Distributed analyses using distinct classes of Brillouin scatterings in optical fibres

THÈSE N^{O} 9022 (2018)

PRÉSENTÉE LE 30 NOVEMBRE 2018
À LA FACULTÉ DES SCIENCES ET TECHNIQUES DE L'INGÉNIEUR
GROUPE SCI STI LT
PROGRAMME DOCTORAL EN PHOTONIQUE

ÉCOLE POLYTECHNIQUE FÉDÉRALE DE LAUSANNE

POUR L'OBTENTION DU GRADE DE DOCTEUR ÈS SCIENCES

PAR

Desmond CHOW MING CHIA

acceptée sur proposition du jury:

Prof. D. Psaltis, président du jury
Prof. L. Thévenaz, directeur de thèse
Prof. J.-C. Beugnot, rapporteur
Prof. A. Zadok, rapporteur
Prof. T. Kippenberg, rapporteur

ÉCOLE POLYTECHNIQUE
FÉDÉRALE DE LAUSANNE

Suisse
2018

Great are the works of the Lord,
studied by all who delight in them.
— Psalm 111:2 The Bible

To my late mother…

Acknowledgements

Pursuing doctoral studies at EPFL is certainly an exciting and unforgettable experience for me. I would like to thank many kind people inside and outside of my professional sphere who accompanied me through this journey.

First and foremost, I would like to thank my supervisor Prof. Luc Thevénaz for offering me the opportunity to study PhD at EPFL. I greatly appreciate his professional guidance as well as personal advice throughout my doctoral student years. Despite his busy schedules, he always attend to my academic related matters no matter how small they are. I thank him also for the cordial working environment that he created in which I could progress.

I would like to extend my gratitude to Prof. Jean-Charles Beugnot for hosting me several times in FEMTO-ST, Besançon through a common project-Opto-acoustic microwires (OASIS) and for sharing with me his invaluable experience in Brillouin scatterings. Special thanks to Prof. Vincent Laude and Prof. Kien Phan Huy in FEMTO-ST for guiding me to understand the numerical simulation and analytical model of Brillouin scatterings.

I am grateful to my colleagues for their supports and friendships: Flavien Gyger, Simon Zaslawski, Li Zhang, Tiago Neves, Galal Malak, Yang Zhisheng, Yang Fan and Yao Can. I also appreciate the help and company of my former colleagues: Kenny Heytow, Marcelo Soto, Mehdi Alem, Andrey Denisov, Xin Lu and Zhiyong Zhao.

I would like to thank the committee members of my doctoral exam for having accepted to assess my thesis: Prof. Avi Zadok, Prof. Jean-Charles Beugnot and Prof. Tobias Kippenberg. I would also like to thank Prof. Demetri Psaltis for being the president of the thesis jury.

On the personal side, I would like to extend special thanks to several members of Westlake Church Lausanne and Eglise Chrétienne Chinoise de Lausanne (ECCL) for inviting me to their home and for fellowship. Westlake: Tom Rizzo & family, Martin Slack & family, Alphonse Abraham & family, Mike Kamrath & family, Ruan Roux, Andrew Simon, Mark Chadwick, Mark Sutherland, Iddo Grothe, Lukas Tiller, Stephan Muhlberg, Dom Reinle; ECCL: Gordon Kan & family, Yung-Min Tsai & family, Yizhu Liu & family, Jingkui Wang & family, Lanpeng Ji & family, Wencheng Ji and many other friends to whom I must apologize for not mentioning.

I would like to thank my parents for their support and encouragements, especially to my late mother who passed away just a few months before I started my PhD at EPFL. I also appreciate the supports and advices from my brother Colin.

Thank you Lord Jesus for your unending grace, mercy and love. Thank you for comforting me in my most difficult time and for opening ways for me when future seemed bleak.

Lausanne, September 2018 Desmond Chow

Abstract

Brillouin scattering is an interaction between light and sound in a material. This inelastic light scattering had been observed in the first optical fibres that were used in cross-continent communication. Via Brillouin scattering, the guided light wave in an optical fibre is back-scattered by the thermally generated high frequency acoustic waves and undergo Doppler frequency shift. Owing to the sensitivity of acoustic velocity to the change of temperature and strain, Brillouin scattering has been widely used in distributed fibre sensors and its resolution, distance range and speed of measurements have been tremendously improved. However, all reported distributed Brillouin fibre sensors incorporate the axial propagating acoustic wave and thus limited to detecting physical parameters inside the fibre core.

In this thesis, distinct classes of Brillouin scatterings in optical fibres are explored and analysed in distributed fashion. Apart from the axial propagating acoustic wave, optical fibre supports a huge variety of elastic vibrations. In the first part, surface and hybrid Brillouin scatterings are studied by using the tapered optical fibre. As the diameter of optical fibre approaches subwavelength range (diameter $\approx 1\ \mu$m), the material properties contrast at the boundary of microfibre (the central part of the tapered optical fibre) gives rise to Rayleigh wave which propagates on the surface. This type of Brillouin scattering as well as the other acoustic resonances along the transition region of the tapered fibre are measured using a distributed Brillouin analysis technique based on phase correlation.

In the second part, forward stimulated Brillouin scattering (FSBS) in standard single-mode fibres (SMF) is explored as a new type of sensor that allows materials surrounding the optical fibre to affect the phase of the guided light. FSBS is an interaction between the guided light and the transverse acoustic waves which are stimulated through electrostriction and resonate within the fibre cross-section due to the acoustic reflection at its boundary. The variation of the acoustic impedance mismatch between the fibre bulk and the external material affects the boundary reflectivity and modify the acoustic decay rate. An experiment has been performed to demonstrate the feasibility to measure acoustic impedance of several liquids through FSBS. As the scattered light of FSBS is in forward direction, obtaining its distributed profile along a fibre is a challenge due to the absence of time-of-flight information. In order to overcome this problem, the local response of FSBS is recovered through measuring the sidebands progression of a light pulse using the backward Brillouin scattering.

Keywords: Brillouin scattering, distributed optical fibre sensors, nonlinear optics.

Résumé

La diffusion Brillouin est une interaction entre la lumière et le son dans un matériau. Cette diffusion inélastique de la lumière a été observée dans les premières fibres optiques qui ont été utilisées pour la communication intercontinentale. Avec l'effet Brillouin, la lumière guidée dans une fibre optique est rétrodiffusée par les ondes acoustiques de haute frequence générées par l'agitation thermique et subit un décalage de fréquence Doppler. Grâce à la sensibilité de la vitesse acoustique à la température et à la dilatation, l'effet Brillouin a été largement utilisé dans les capteurs à fibres optiques distribués et leur résolution, distance de mesure et rapidité ont été grandement perfectionnés. En revanche, toutes les études des capteurs à fibres optiques distribués tirent uniquement parti de l'onde acoustique axiale et sont donc limités à la détection de paramètres physiques au cœur de la fibre optique.

Dans cette thèse, des diffusions Brillouin de différentes catégories dans les fibre optiques sont explorées et examinées de manière distribuée. Hormis l'onde acoustique axiale, la fibre optique permet une grande variété de vibrations élastiques. En premier lieu, les diffusions Brillouin de surface et hybride sont etudiées en utilisant une fibre optique effilée. Lorsque le diamètre devient inférieur à la longueur d'onde (diamètre $\approx 1\ \mu$m), le contraste des propriétés du matériau à la surface de la microfibre (la partie centrale de la fibre effilée) génère une onde Rayleigh qui est guidée à la surface. Ce genre de diffusion Brillouin ainsi que d'autres résonances acoustiques le long de la fibre effilée sont mesurées en utilisant une technique d'analyse Brillouin distribuée basée sur la corrélation de phase.

En second lieu, la diffusion Brillouin vers l'avant (DBVA) dans les fibres optiques conventionnelles est explorée comme un nouveau type de capteur qui permet aux matériaux entourant la fibre optique de modifier la phase de la lumière guidée. L'effet DBVA est une interaction entre la lumière guidée et les ondes acoustiques transverses qui sont stimulées par l'électrostriction et entrent en résonance à l'intérieur de la section transversale de la fibre à cause de la réflexion acoustique à sa surface. La variation de la disparité d'impédance acoustique entre le matériau du corps de fibre et le matériau extérieur influe sur la réflectivité de surface et modifie le taux d'atténuation acoustique. Une expérience a été réalisée pour démontrer la faisabilité de mesurer l'impédance acoustique de certains liquides par DBVA. Comme la lumière diffusée par DBVA se propage vers l'avant, l'obtention de son profil distribué représente un défi en raison de l'absence d'information du temps de vol. Afin de surmonter cette difficulté, la réponse locale de DBVA est récupéré en measurant la progression des harmoniques d'une impulsion lumineuse en utilisant la rétrodiffuse Brillouin.

Mots-clés : diffusion Brillouin, capteurs à fibre optique distribués, effets non-linéaires.

Contents

Acknowledgements **v**

Abstract **vii**

List of figures **xii**

List of tables **xvii**

Introduction **1**

1 Brillouin scatterings in optical fibre **5**

1.1 Brillouin scattering 5
1.2 Stimulated scattering process 7
1.3 Elastic wave propagation 8
1.3.1 Strain 9
1.3.2 Stress 10
1.3.3 Stiffness tensor 12
1.3.4 Elastic energy 13
1.3.5 Isotropic solid 15
1.3.6 Wave equation 17
1.3.7 Attenuation 19
1.3.8 Cylindrical waveguide 19
1.4 Electrostriction 24
1.5 Brillouin scattering as optical nonlinearity 26
1.6 Classes of Brillouin scatterings 29
1.7 Distributed analyses using backward SBS 32
1.7.1 Brillouin optical time domain analysis 35

2 Surface and hybrid Brillouin scatterings **37**

2.1 Acoustic resonances in microfibre 37
2.2 Tapered optical fibre 43
2.3 Distributed analysis of surface and hybrid acoustic waves 44
2.3.1 Theory of phase-correlation distributed Brillouin measurement 45
2.3.2 Spatial resolution 47
2.3.3 Experimental setup 49

2.3.4 Distributed Brillouin spectrum of microfibre 50
2.3.5 Discussion 53

3 Forward stimulated Brillouin scattering 55
3.1 Transverse acoustic resonances 56
3.2 Optical stimulation 57
3.3 Detecting the response of FSBS 60
3.3.1 Optical and acoustic waves coupling 62
3.3.2 Experimental setup 64
3.3.3 Kerr-induced spectral distortion 65
3.4 Acoustic impedance sensing 69
3.4.1 Retrieving the acoustic impedance 69
3.5 Thin polymer coated optical fibre 74
3.5.1 Acoustic impedance measurement 75
3.5.2 Experimental results 79
3.6 Distributed analysis of forward Brillouin scattering 79
3.6.1 Concept and implementation 80
3.6.2 Activation of the FSBS transverse acoustic wave 81
3.6.3 Reading the FSBS-induced phase modulation 83
3.6.4 Intensity progression of the reading pulse sidebands 85
3.6.5 Phase factor recovery and data processing 85
3.6.6 Experimental results 89
3.6.7 Discussion 93

Conclusions 94

A Mathematical operations in the cylindrical coordinate system 99

B Material constants for standard silica optical fibre 101

C FSBS overlap integral 103

Bibliography 111

Curriculum Vitae 113

List of Figures

1.1 The illustration of Brillouin scattering theory. Schematic diagram of (a) the propagation direction and (b) Momentum conservation of the incident, scattered light and the acoustic wave. (Dashed line indicates Anti-Stokes process.) 6

1.2 Illustration of a 1D solid that is fixed on one side and is elongated by a force F on the other end. The material length Δx bounded by PQ is transformed to P'Q'. Strain S is defined as the transformed length Δu divided by the elemental length $S = \Delta u / \Delta x$. 9

1.3 Illustration of a 3D solid at equilibrium. Stress $\mathbf{T}$ acting on an infinitesimal surface ds with normal vector $\mathbf{n}$ and the internal volume force $\mathbf{f}_i$ acting on a infinitesimal volume dV. 11

1.4 Cylindrical coordinate system with unit vectors $\mathbf{r}$, $\boldsymbol{\theta}$ and $\mathbf{z}$. 20

1.5 The dispersion relation of compression wave $n = 0$ in silica cylindrical waveguide. The abscissa is the axial wave vector normalised by the radius a. The ordinate is the mode frequency normalised by the radius a and the transverse wave velocity V_T. The right diagram is the magnification of the left diagram in the region with small wave vector and frequency. Close to the zero axial wave vector, the acoustic modes are dispersive except for the L_{01} mode, their group velocities are close to zero whereas their phase velocities are enormous. 23

1.6 Phase matching conditions and scattering directions of several classes of Brillouin scatterings elucidated using the dispersion diagrams. The (a) backward (b) forward and (c) intermodal stimulated Brillouin scattering. Solid and dotted arrows represent optical and acoustic waves, respectively. 30

1.7 Illustration of (a) single-end and (b) two-end access configurations. 32

1.8 Illustration of (a) time-of-flight, (b) frequency domain and (c) correlation measurement techniques. 33

2.1 The dispersion diagram of the radially symmetric acoustic waves in a 1 μm-diameter silica microfibre. the gray vertical line in the middle indicates the experimental condition where the wave vector k is positioned at $k = 4\pi n_{\text{eff}}/\lambda$ where the optical wavelength λ is 1.55 μm and the effective refractive index n_{eff} is 1.23. 39

2.2 The acoustic displacement profiles of the 1 μm-diameter microfibre at the resonance frequencies f_{res} within 0 and 12 GHz: 5.55 GHz, 8.68 GHz, 9.51 GHz and 11.15 GHz. The lowest resonance mode (f_{res} = 5.55 GHz) is the surface acoustic mode where the acoustic field amplitude decreases rapidly from the microfibre boundary. 40

2.3 Resonance frequencies of the radial (axisymmetric) acoustic modes as the radius of microfibre varies from 0.25 μm to 2.5 μm. Gray vertical line indicates the microfibre with radius of 0.5 μm. 41

2.4 Brillouin spectrum of microfibre by varying the radius obtained through semi-analytical method. The amplitude of spectrum for each radius is normalised by the highest peak and plotted in logarithmic scale. 42

2.5 Taper profile including microfibre and the taper transition region. Since the tapered fibre is symmetric, only half of its profile is shown. Position 0 cm is the middle of the tapered optical fibre. 43

2.6 Integrated stimulated Brillouin scattering gain spectrum measured using counter propagating pump and probe lights. The surface and hybrid acoustic modes associated to the microfibre section are clearly visible. Different acoustic modes are observed from 10-12 GHz as a result of the diameter variation along the taper transition region. 44

2.7 Illustration of phase-correlation based distributed Brillouin measurement with 7-bit Pseudo Random Binary Sequence (PRBS). 46

2.8 The position of the first order correlation peak is displaced by Δz through varying the duration of PRBS bit T_{bit}. 46

2.9 The gain response calculated from the convolution of a triangular correlation peak and the rectangular region R with length δ. 48

2.10 Experimental setup used for phase correlation-based distributed Brillouin measurements. The components are labelled as follows: EDFA, erbium-doped fibre amplifier; SOA, semiconductor optical amplifier; FBG, fibre Bragg grating. PRBS, pseudo random binary sequence. 50

2.11 Phase-correlated distributed Brillouin gain spectra along the silica microfibre for frequency ranges: (a) 5.5 – 5.7 GHz, (b) 8.5 – 9.0 GHz, (c) 9.5 – 10.0 GHz, (d) 10.0 – 10.5 GHz, (e) 10.5 – 11.0 GHz and (f) 11.0 – 11.5 GHz. Position 0 cm is the center of the tapered waist. Gain scales are linear, calculated with respect to the detected off-resonance signal level in each scanning region. Note that the horizontal scale of (a) is made narrower to visualize the entire scanning result that has larger spatial resolution. 51

2.12 Brillouin spectrum as a function of tapered fibre position. Labels (a) to (f) indicate the corresponding acoustic modes measured in Fig. 4(a)-(f) 52

3.1 (a) Dispersion diagram of radial transverse acoustic waves. (b) Zoom-in of dispersion diagram for small axial wave vector where the group velocity is negligible. (c) The phase matching between the vectors of the pump, Stokes lights and the stimulated transverse acoustic mode, which is given by the crossing points of acoustic modes and light line (dotted line) in (b). 57
3.2 Theoretical and experimental FSBS spectrum. 58
3.3 The normalised displacement u_{norm} and dilatation S_{norm} profile of the 5th, 7th and 9th radial transverse acoustic mode. The normalised optical mode profile (bottom). 59
3.4 The impulse response of FSBS when the fibre without coating is exposed to air. (a)(b) The experimental result is overlaid on the theoretical trace. (a) The decay time τ of the transverse acoustic wave is found to be around 1 μs by comparing with the experimental result. (b) The initial part of the trace ($t \leqslant 100$ ns) exhibits pseudo periodical pattern with time separation Δt of around 21 ns. 61
3.5 Experimental setup used for detecting the response of FSBS. The uppermost branch (black line) gives the pump light for the generation of transverse acoustic waves in the sensing fibre. The probe (grey line) is configured as a Sagnac interferometer that converts the time dependent phase-shift induced by the transverse acoustic waves to intensity change that is detectable by a photodiode. The components are labelled as follows: PC, polarisation controller; EDFA, Erbium doped fibre amplifier; BPF, bandpass filter; PD, photodiode. 66
3.6 The combination of FSBS resonance and Kerr effect. (a) The detected resonance spectrum exhibits Fano shape, described as the combination of a complex Lorentzian function (FSBS resonance peak) and the Kerr-induced phase shift that is uniform in spectrum. (b) The simulated signal phase shift of the combined effect compared with the signal phase shift due to FSBS effect alone. 67
3.7 Temporal traces and the corresponding VNA spectra of the detected signal at photodetector (a)(c) without and (b)(d) with pulse gating. 68
3.8 Illustration of acoustic round-trip and reflection at fibre boundary. 70
3.9 Time response of FSBS to a 1 ns short impulse when fibre is surrounded by (a) air, (b) ethanol and (c) water. Time constant τ is determined from fitting the envelope of the signal with exponential decay function. (a) to (c) are normalised by the respective initial amplitude. 71
3.10 Resonance spectrum of transverse acoustic wave when fibre is surrounded by (a) air, (b) ethanol and (c) water. Linewidth $\Delta\nu$ is determined from fitting the resonance spectrum with Lorentzian function. (a) to (c) are normalised by the respective peak intensity. 72
3.11 The measured parameters against external acoustic impedance for (a) time domain technique and (b) frequency domain technique. 74
3.12 Schematic diagram of the optical fibre with polyimide coating layer that acts as a 1D acoustic thin film. The reflection is angled for clarity purpose, transverse acoustic wave being assumed to be reflected normally from the surfaces. 75

3.13 FSBS spectrogram of the 80 μm-diameter polyimide coated fibre that is measured using the frequency domain technique. 76

3.14 Measured FSBS resonance spectra when the 80 μm thin polyimide coated fibre is surrounded by (a) air, (b) ethanol and (c) water. 78

3.15 Activation and reading of the transverse acoustic wave at an arbitrary fibre position. An intensity modulated optical pulse (magenta) stimulates a transverse acoustic wave (blue) (the oscillating period has been enlarged for illustration purpose), whose spectrum is probed by the reading pulse (green) that is time-overlapping with a short segment of the acoustic tail. The reading pulse is phase modulated by the transverse acoustic wave, thus generating multiple spectral sidebands. The longitudinal evolution of each reading pulse sideband resulting from this phase modulation is independently mapped by the process of backward stimulated Brillouin scattering. 81

3.16 Schematic diagram of the apparatus used to measure the spatially resolved spectrum of forward stimulated Brillouin scattering (FSBS). The FSBS activation light is represented as the magenta path (λ = 1533 nm) and the probing system based on backward stimulated Brillouin scattering (BSBS) is represented as the green path (λ = 1551 nm). The sensing fibre is 730 m-long and consists of a 30 m uncoated segment spliced between two coated segments of 500 m and 200 m respectively. The components are labelled as follows: EOM, electro-optic modulator; ISO, isolator; PC, polarisation controller; EDFA, erbium-doped fibre amplifier; SOA, semiconductor optical amplifier; PS, polarisation switch; PD, photodetector; FBG, fibre Bragg grating. The mathematical symbols are defined as follows: ν_{res}, the selected FSBS resonant frequency; ν_{F}, frequency of the intensity modulation and $\Delta\nu_{\mathrm{F}}$, scanned frequency detuning for FSBS activation; ν_{B}, Brillouin frequency shift of BSBS; $\nu_{\mathrm{p}}^{(n)}$, frequency of the intensity modulation and $\Delta\nu_{\mathrm{B}}$, scanned frequency detuning for BSBS probe. 82

3.17 Simulated longitudinal evolution of the reading pulse spectrum. (a) The reading pulse spectrum changes along the fibre as it is being phase modulated by the transverse acoustic wave of forward stimulated Brillouin scattering (FSBS). (For illustration purpose, the fibre surroundings is assumed to be uniform along the fibre, i.e., the phase factor $\xi(\nu_{\mathrm{F}}, z_{\mathrm{r}})$ increases linearly with respect to the reading pulse location z_{r}. The spectrum is normalised by the input intensity of the reading pulse at its central frequency.) (b) The intensity progression of the 0th, 1st and 2nd order spectral sidebands (each one proportional to J_0^2, J_1^2 and J_2^2, respectively) of the reading pulse as a function of the z_{r}-dependent phase factor $\xi(\nu_{\mathrm{F}}, z_{\mathrm{r}})$. (c) The reading pulse spectrum at an arbitrary position. Note that the local spectral sidebands are separated by the modulation frequency of FSBS activation ν_{F}. 84

3.18 Measured intensity progressions of the reading pulse sidebands. Intensity $I_{\mathrm{r}}^{(n)}(\nu_{\mathrm{F}}, z_{\mathrm{r}})$ of the (a) 0th, (b) 1st and (c) 2nd order reading pulse sidebands (each one is proportional to J_0^2, J_1^2 and J_2^2, respectively), measured at each scanning frequency ν_{F} (detuned within $\Delta\nu_{\mathrm{F}}$ around ν_{res}). Experimental results are obtained when the 30 m uncoated fibre segment is exposed to air. 86

3.19 Data processing steps to obtain the local response of forward stimulated Brillouin scattering. (a) The measured intensity $I_{\mathrm{r}}^{(n)}(z_{\mathrm{r}})$ of the 0th, 1st and 2nd order spectral sidebands versus distance z_{r}, obtained at the FSBS peak resonant frequency ν_{res}. (b) Phase factor $\xi(z_{\mathrm{r}})$ retrieved by using the Bessel recurrence relation in Eq. 3.52. (c) The local amplitude of refractive index changes $a_{\mathrm{RI}}(z)$ (unitless) that is obtained by using segmental differentiation. 88

3.20 Distributed spectra of forward stimulated Brillouin scattering (FSBS) measured over the 730 m-long sensing fibre when the 30 m uncoated fibre segment is exposed to (a) air, (b) ethanol and (c) water. The FSBS responses represented by the local amplitudes of refractive index changes a_{RI} (unitless) could be clearly observed in the exposed fibre regions (0.5 km). 89

3.21 The spectra of forward stimulated Brillouin scattering (FSBS) measured at a given fibre position inside the 30 m fibre segment exposed to (a) air, (b) ethanol and (c) water. The FSBS spectra measured at an arbitrary position in the normal coated fibre segment (with acrylate polymer coating) are plotted alongside for comparison. $\Delta\nu_{\mathrm{FWHM}}$ is the full width at half maximum (FWHM) of the measured spectrum at the sensing point (convolution of the pulse spectrum and FSBS resonance spectrum) and $\Delta\nu_{\mathrm{m}}$ is the recovered original linewidth of FSBS resonance at the corresponding position. 90

3.22 Broadening of the measured FSBS resonance linewidth caused by the finite duration of FSBS activating pulse. (a) The convolution of the pulse spectrum and the Lorentzian shape FSBS resonance spectrum simulated via numerical approach (using *conv* function in Matlab) and analytical approach (using Eq. 3.56). The Lorentzian linewidth $\Delta\nu_{\mathrm{m}}$ and the pulse duration T are arbitrarily set as 0.5 MHz and 0.5 μs, respectively. (b) The original FSBS resonance linewidth $\Delta\nu_{\mathrm{m}}$ recovered from the FWHM of the measured spectrum of the convolution $\Delta\nu_{\mathrm{FWHM}}$ for two different FSBS activating pulse durations, $T = 0.5$ μs and $T = 0.7$ μs. Both numerical and analytical approaches are plotted, they give the same $\Delta\nu_{\mathrm{m}}$. The points corresponds to the measurement results of air, ethanol and water surroundings as in Fig. 3.21 are marked by crosses. 92

List of Tables

1.1 Category of distributed Brillouin analyses 31
1.2 Nomenclatures of distributed Brillouin measurement techniques 31

3.1 The resonance frequencies of radial transverse acoustic waves in SMF. 58
3.2 Resonance frequencies of the 80 μm-diameter polyimide coated fibre. 77
3.3 Experimental results and calculations of acoustic impedances 79

Introduction

The study of Brillouin scatterings in optical fibres is an interdisciplinary domain that encompasses optics, elastic waves and mechanical properties of materials. In essence, Brillouin scattering is the interaction between light and propagating elastic waves in a material. Elastic waves exist in a medium at mechanical equilibrium because of thermal fluctuations (spontaneous Brillouin scattering process) or through the presence of optical fields that are phase-matched with the speed of sound in the medium (stimulated Brillouin scattering (SBS) regime). The elastic waves scatter light waves through a Bragg scattering process, in which the light wave is backscattered and Doppler shifted, or through Raman-Nath diffraction, where the light wave is phase modulated and forward scattered at successive angles. With the emergence of lasers, the generation of strong gigahertz sound waves in a material is enabled, which was unattainable using common piezoelectric materials. Since the frequency of scattered light depends on sound velocity, SBS had been employed extensively in the characterisation of elastic and photoelastic properties of transparent crystals especially for small volume sample [83]. Besides solids, Brillouin scatterings were studied in several material phases including gas [38], liquid [18, 16], superfluid [63] and plasma [54].

In fibre optics, Brillouin scattering was traditionally studied as an undesired effect because it poses a limitation on the maximum transmitted power. Due to the long interaction length between optical and acoustic fields, the stimulated acoustic wave depletes the transmitted power by continuously transfers power from the forward propagating light to the backscattered light. In fibre optics communications, applying phase modulation on the transmitted light is a common practice to suppress Brillouin scattering [24]. This approach is nevertheless infeasible for high power laser delivery system, instead a combined approach of fibre design and active cooling mechanism is used [92]. On the contrary, Brillouin scattering is important in fibre optics sensing. Since the speed of sound is sensitive to the change in material density and temperature, Brillouin scattering in optical fibre enables temperature and strain measurements in a distributed fashion that extends beyond 50 km and could reach spatial resolution of less than 1 m.

The acoustic wave that is present in the conventional Brillouin scattering is the longitudinal propagating elastic wave. In fact, there are many classes of acoustic guidances as the optical fibre is essentially an acoustic waveguide. Nevertheless, the observation of these acoustic guidances in optical fibre through Brillouin scattering depends on the phase matching between the optical waves and the related acoustic waves as well as their field overlap magnitude. In an optical fibre, the degree of freedom in wave vector matching is limited to the axial direction. In other words, to enable Brillouin interaction with acoustic waves guided with an oblique wave vector, the guided optical waves must have a wave vector difference that matches the axial wave vector component of the guided acoustic waves. This translates into distinct resonance frequencies for different classes of acoustic guidance. Hence, the focus of this thesis is set to investigate several classes of acoustic waves that are present in an optical fibre through Brillouin scattering. In particular, distributed Brillouin analyses are developed or in certain cases re-adapted to position resolve these acoustic resonances. Their applications, especially on a new type of fibre sensing that detects the mechanical properties of the external material, are explored and presented.

Chapter 1 discusses the general principles of Brillouin scattering in optical fibres. The theories of elastic waves are reviewed in the chapter as they serve as the foundations for understanding the subsequent acoustic wave analysis of a cylindrical waveguide, which represents the structure of an optical fibre. Especially, its acoustic guidance can be described analytically by a dispersion relation (Pochhammer-Chree equation) that relates the acoustic wave vector to its resonance frequency. Nevertheless, the scope of cylindrical waveguide analysis discussed in the chapter focuses only on the radially symmetric (axisymmetric) modes as the context of experiments in the subsequent chapters revolves around the radially symmetric cases. Subsequently, an expression of electrostrictive stress is reviewed, formulated in terms of photoelastic constants through an analysis of energetics. Combining the electrostrictive force and the elastic wave equations, a general expression for elastic wave propagation under an electrostrictive force (elastodynamic equation) is highlighted. Being in the domain of distributed Brillouin fibre sensing, the existing distributed sensing techniques using longitudinal acoustic wave, which provides the background for the distributed analyses of distinct Brillouin scatterings in the subsequent chapters, are briefly reviewed.

Chapter 2 describes the Brillouin scatterings of a microfibre, which were first studied in FEMTO-ST Institute, France [12]. In a subwavelength waveguide such as the microfibre, the guided acoustic field is tightly confined within the cross-sectional area and subjected to the stark mechanical properties difference across the boundary which gives rise to dispersive acoustic guidance and avoided crossings between compressional and shear acoustic modes. In addition, the optical field in microfibre extends beyond the microfibre structure and has large overlap with several acoustic modes. Thus, the Brillouin spectrum of a microfibre exhibits a few resonance peaks, the peak with the lowest resonance frequency corresponds to the surface acoustic wave (Rayleigh wave), which has acoustic field strength that is maximum at the boundary and decreasing towards the centre of microfibre. The microfibre (produced in FEMTO-ST Institute, France) is fabricated from tapering a standard single-mode fibre (SMF) using flame brushing technique, and has diameter of ~1 μm and length of ~10 cm. This microfibre produced from tapering provides good light coupling but several acoustic resonances from the taper transition region which do not belong to the microfibre are present in the integrated Brillouin spectrum. Therefore, in this thesis, a previously reported phase correlation distributed Brillouin analysis technique, which permits position scanning with centimeter resolution is used here to position resolve the Brillouin spectrum along the taper fibre so that the acoustic resonances can be mapped to their respective fibre sizes [20]. The experimental results are compared with the semi-analytical theoretical simulations and show good agreement.

Chapter 3 explores a novel application of forward stimulated Brillouin scattering (FSBS) in fibre optics sensing-measure the acoustic impedance of the material surrounding a standard single-mode fibre. This application was first proposed in Bar-Ilan University, Israel [6]. FSBS process involves acoustic waves that resonate within the transverse plane of an optical fibre. Because of the multi-pass acoustic reflections of the resonating transverse acoustic waves at the fibre boundary, the reflectivity between the fibre bulk silica and the external material can be retrieved from the acoustic decay rate or linewidth broadening, and from these parameters the acoustic impedance of the external material is determined. The principle of FSBS is discussed and reviewed in the chapter, based on the FSBS coupled wave theory in literature, an expression that estimates the acoustic-induced refractive index change is formulated. In the detection of FSBS, the resonance spectrum is distorted by Kerr effect and the solution to this problem through pulse gating is presented. The acoustic impedance sensing is also demonstrated by using a thin polyimide coated fibre, which overcomes the need of removing the fibre coating as in several previous works. In the final part of the chapter, one of the main works of this thesis-a distributed FSBS measurement technique is presented [22], a simultaneous and independent work on distributed FSBS measurement is also achieved in Bar-Ilan University, Israel [10]. Position-resolving FSBS is challenging as FSBS is a forward scattering process and does not involve backscattered light that brings time-of-flight information. Harnessing the FSBS-induced phase-modulated sidebands of a light pulse and using the backward stimulated Brillouin scattering process, the local phase change due to transverse acoustic wave along the fibre can be recovered. The results of distributed FSBS spectrum measurement as well as the local acoustic impedance retrieval are presented.

The final chapter summarises the main results of this thesis. A few ongoing works and the areas to be improved are outlined and discussed. The future perspectives and possible applications on the outcomes of this thesis are proposed and evaluated.

1 Brillouin scatterings in optical fibre

1.1 Brillouin scattering

Light scatterings is a ubiquitous physical phenomenon that is significant in bridging the microscopic material properties with visual observation by human eyes. The blue sky, atomic lattice, molecular vibration and material elasticity are among the numerous classical examples of scientific domain that had been studied through the scattering of light. In physical terms, subwavelength fluctuations in optical properties of a medium is the origin of light scattering. A perfectly homogeneous material can scatter light in the forward direction only as the scatterings in all the other directions cancel out mutually through destructive interference. In addition, the scattering of light in forward direction is the reason for refractive index, the theoretical discussion is in [31]. Several light scattering processes are described extensively in literature: Rayleigh scattering refers to the scattering of light from sub-wavelength density fluctuations; Raman scattering originates from the interaction of light with the vibrational modes of molecules; Brillouin scattering is the interaction of light and sound wave (propagating density fluctuations).

Initially, Brillouin scattering was just a pure theoretical prediction by Léon Brillouin which appeared on his note in 1914. The proposed theory, however, was not formally disseminated until 1922. The original motivation of his work was to complete Einstein's theory on solid and reconciling it with Debye's model on specific heat [58]. The experimental verification of Brillouin's theory was found to be difficult at that time due to the unavailability of intense and coherent light source to efficiently induce ultrasonic pressure wave in a medium. Since the first published theory in 1922 [17], the theory would need an additional eight years to be experimentally proven by E. Gross [36]. Although Gross's experiment was originally set to explore Raman scattering in several organic liquids, it turned out that the observed scattered light did not agree with the expected Raman lines but agree extremely well with the acousto-optic theory proposed by L. Brillouin and P. Debye. In the advent of laser, Brillouin scattering in a solid material could be studied systematically especially in the stimulated regime, as demonstrated by R. Chiao and C. Townes in 1964[19].

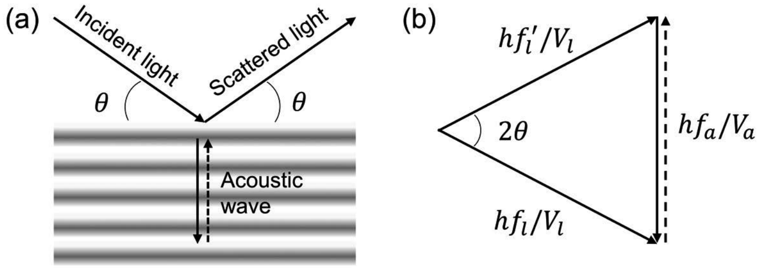

Figure 1.1 – The illustration of Brillouin scattering theory. Schematic diagram of (a) the propagation direction and (b) Momentum conservation of the incident, scattered light and the acoustic wave. (Dashed line indicates Anti-Stokes process.)

The experimental context of the theory originally proposed by L. Brillouin was to investigate the scattered light when the incoming light is incident on the surface of a medium at an angle θ, as illustrated in Fig 1.1(a). Although an acoustic stimulation process is absent, faint sound waves do exist spontaneously in a medium due to thermal fluctuations. Inspired by Bragg's theory that was used to study crystal lattice by X-ray scattering, given as $2d\sin(\theta) = n\lambda$ where d is the lattice constant and λ is the scattered wavelength, it was apparent to L. Brillouin that the periodical pattern of the propagating density wave resembles a lattice structure that would scatter light in a similar manner. Replacing d in Bragg's theory with the acoustic wavelength λ_a and after some mathematical manipulations yield the following expression

$$\frac{f_\mathrm{a}}{f_\mathrm{l}} = \pm 2\frac{V_\mathrm{a}}{V_\mathrm{l}}\sin(\theta) \tag{1.1}$$

f_l, f_l' and f_a are the frequencies of incident, scattered light and the acoustic wave, respectively. V_l and V_a are the velocities of light and sound, respectively.

In Bragg scattering, the frequency of the scattered light is the same as that of the incident light, thus the material could be seen as a stationary mirror that reflects light at certain frequencies. For Brillouin interaction, the scattered light is frequency shifted because the acoustic wave is travelling away or towards the wave front of the incident light, leading to Doppler-shifted scattered light frequency. A receding acoustic wave red-shifts the incident light frequency and results in Stokes light. Conversely, an advancing acoustic wave blue-shifts the incident light frequency and leads to Anti-Stokes light.

Brillouin's formula can be illustrated with the isosceles in Fig. 1.1(b). In essence, it holds that momentum is conserved among the incident, scattered lights and the propagating density wave, $hf_\mathrm{l}'/V_\mathrm{l} = -hf_\mathrm{l}/V_\mathrm{l} \pm hf_\mathrm{a}/(V_\mathrm{a}\sin(\theta))$, where h is the Planck's constant. This relation indirectly provides an elegant way to describe wave-particle duality of acoustic wave. According to quantum theory of light, an optical wave of angular frequency ω and wavevector $\mathbf{k}$ is considered as a stream of photons, each with energy $\hbar\omega$ and momentum $\hbar\mathbf{k}$. Likewise an acoustic wave of angular frequency $\Omega = 2\pi f_\mathrm{a}$ and wavevector $|\mathbf{q}| = 2\pi/\lambda_\mathrm{a}$ can be viewed as a stream of acoustic quanta called phonon, each with energy $\hbar\Omega$ and momentum $\hbar\mathbf{q}$. In quantum mechanics, Brillouin Stokes process is viewed as the annihilation of an incident photon while a Stokes photon and an acoustic phonon are created simultaneously. The process is reverse for Brillouin Anti-Stokes process where an incident photon and an acoustic phonon are annihilated to create a new photon.

1.2 Stimulated scattering process

Brillouin interaction involves the presence of two light fields (pump and Stokes lights) and an acoustic wave. In the absence of an initial Stokes light, the scattering is spontaneous where the participating acoustic wave is induced by thermal fluctuations in the medium [15]. However, in the presence of an initial Stokes light, the scattering process becomes stimulated, known as stimulated Brillouin scattering (SBS). In this regime, the Stokes light interferes with pump light, resulting in an oscillating light intensity that varies spatially and temporally. Through electrostriction, this variation in light intensity produces moving sinusoidal density fluctuations (acoustic wave) in the medium. As a result, pump light is scattered by the acoustic wave as Stokes light, leading to an even stronger interference between pump and Stokes lights that further reinforces the acoustic wave. Eventually, this positive feedback produces an intense Stokes light that grows exponentially as a function of interaction length.

Phase matching is important in SBS process, the scattering condition relies on both wave vectors and frequency difference of the participating light waves. Because of the conservation of both the energy and momentum in Brillouin interaction, the frequencies and wave vectors involved in each Stokes scattering event are parametrically related by

$$\Omega = \omega_{\mathrm{p}} - \omega_{\mathrm{s}} \tag{1.2a}$$

$$\mathbf{q} = \mathbf{k}_{\mathrm{p}} - \mathbf{k}_{\mathrm{s}} \tag{1.2b}$$

where ω_{p}, ω_{s}, Ω are the frequencies and $\mathbf{k}_{\mathrm{p}}$, $\mathbf{k}_{\mathrm{s}}$, $\mathbf{q}$ are the wave vectors of the pump, Stokes light waves and the acoustic wave, respectively. The dispersion relation of the acoustic wave in a boundless medium is given by

$$\Omega = V_{\mathrm{a}}|\mathbf{q}| \tag{1.3}$$

For typical acoustic wave, the frequency ω is small as compared to that of pump and Stokes lights, which gives $\omega_{\mathrm{p}} \approx \omega_{\mathrm{s}}$. Since the components of pump and Stokes wave vectors in the propagation direction of the acoustic wave are the opposite of each other, the acoustic wave vector $\mathbf{q}$ can be approximated as $|\mathbf{q}| \approx 2|\mathbf{k}_{\mathrm{p}}|\sin(\theta)$. Thus the acoustic frequency is given by

$$\Omega = 2V_{\mathrm{a}}k\sin\theta \tag{1.4}$$

where V_{a} is the speed of sound in the medium, k is the wave vector of light and θ is the angle between incident light and the acoustic wave front (refer to Fig. 1.1). Equation 1.4 is the same as Eq. 1.1 discussed previously which was obtained through Bragg equation. In optical fibre, the directions of pump and Stokes lights are in the same axis as the acoustic wave, which gives $\theta = \pi/2$, therefore Eq. 1.4 can be rewritten as

$$f_\mathrm{a} = \frac{2 n_\mathrm{eff} V_\mathrm{a}}{\lambda} \tag{1.5}$$

where f_a is the frequency of acoustic wave, n_eff is the effective refractive index and λ is the vacuum wavelength of light. Brillouin scattering in optical fibre was first observed by E. Ippen and R. Stolen in 1972 [45]. Silica is the bulk material used in standard optical fibre, the acoustic velocity V_a is 5950 ms^{-1} and the effective refractive index $n_\mathrm{eff} \approx 1.45$. Hence, typical Brillouin frequency shift f_a of an optical fibre in telecommunication wavelength ($\lambda = 1.55\mu$m) is found to be around $f_\mathrm{a} \approx 11.1$ GHz.

1.3 Elastic wave propagation

Brillouin scattering discussed in the previous section involves acoustic plane wave that propagates freely in a border-less medium. However, the guiding characteristics are altered when the acoustic wave is confined within a given structure. Optical fibre is a cylindrical acoustic waveguide that supports several classes of guided acoustic waves such as longitudinal, radial, torsional and flexural waves. In standard optical fibres, the cross sectional area of fibre bulk is much larger than the fibre core and the guided optical wave can be seen as interacting with an axially propagating acoustic plane wave, therefore the standard acoustic dispersion relation described in Eq. 1.3 is valid. Nevertheless, when the diameter of an optical fibre approaches the acoustic wavelength, such as a silica microfibre realised by tapering a standard optical fibre, the propagation velocity could change dramatically. Apart from the longitudinal acoustic wave, standard optical fibre also supports transverse acoustic waves that oscillate primarily in the radial direction. This type of acoustic guidance has wave vector that is almost perpendicular to the fibre axis. In fact, regardless of the size of an optical fibre, all types of acoustic guidances exist spontaneously because the wave vector of a guided acoustic wave could take any arbitrary direction. Yet, to operate in the stimulated regime, both pump and Stokes lights have to meet the phase matching conditions so that the resulting interference pattern matches the frequency and axial wave vector of a particular guided acoustic wave.

In view of the dependence of Brillouin scattering on acoustic guidance, the acoustic dispersion relation in a cylindrical structure is to be determined. Acoustic wave traverses in a medium that is elastic. A solid is considered as elastic if it could be elongated by an applied force and return to its original dimension when the force is lifted. The bulk material of a standard optical fibre-silica demonstrates elasticity under a small applied force hence the description of guided acoustic wave follows the analysis of solid elastic waves treated rigorously in [7, 8, 69, 70, 51]. Because of the myriad of mathematical models reported in literature based on different types of analyses, review of the essential parameters from [69, 70] are compiled and included here for clarity and better understanding.

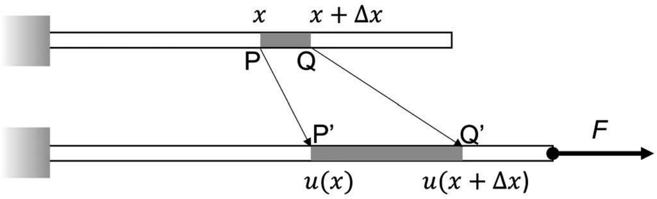

Figure 1.2 – Illustration of a 1D solid that is fixed on one side and is elongated by a force F on the other end. The material length Δx bounded by PQ is transformed to P'Q'. Strain S is defined as the transformed length Δu divided by the elemental length $S = \Delta u / \Delta x$.

1.3.1 Strain

Strain is the parameter that quantifies deformation of a solid. In the simplest form, consider a rod with length L. When placed under an axial force, the rod will be elongated by ΔL and has an axial strain of $\Delta L/L$, the cross section A reduces simultaneously. However, in a continuous medium, the distribution of strain might not be uniform because of the variations in material properties and applied force, which requires an approach that resolves to individual point in the solid.

Lagrange description lays out the analysis of strain based on the geometrical transformation experienced by a local element at equilibrium. Consider an elemental material length Δx on a 1D solid bounded by 2 points P and Q as illustrated in Fig. 1.2. The coordinates of P and Q are x and $x + \Delta x$, respectively. A force F is applied along the axis resulting in an overall elongation of the solid. Points P and Q are now transformed to $u(x)$ and $u(x+\Delta x)$, respectively. Therefore, strain S of 1D solid is defined as

$$S = \frac{u(x+\Delta x) - u(x)}{\Delta x} = \frac{\mathrm{d}u}{\mathrm{d}x} \tag{1.6}$$

For a 3D solid, an applied force simultaneously causes deformation in the other directions apart from the principal direction. For example the cross-sectional area A of a rod shrinks when it is pulled by an axial force, which means its axial elongation is related to its transverse deformation. Inferring from Eq. 1.6, deformation of a 3D solid δu_i can be written as

$$\begin{aligned}\delta u_i &= \frac{\partial u_i}{\partial x_j}\delta x_j \\ &= \frac{1}{2}\left(\frac{\partial u_i}{\partial x_j} + \frac{\partial u_j}{\partial x_i}\right)\delta x_j + \frac{1}{2}\left(\frac{\partial u_i}{\partial x_j} - \frac{\partial u_j}{\partial x_i}\right)\delta x_j\end{aligned} \tag{1.7}$$

Einstein's tensor notation is used here and throughout the text, which implies summation from 1 to 3 over the dummy indices i and j that represent the axes. $\partial u_i / \partial x_j$ is a matrix of 3×3 displacement gradient components. The matrix can be decomposed into the symmetric and asymmetric parts.

$$S_{ij} = \frac{1}{2}\left(\frac{\partial u_i}{\partial x_j} + \frac{\partial u_j}{\partial x_i}\right) \quad \text{symmetric} \tag{1.8a}$$

$$\Omega_{ij} = \frac{1}{2}\left(\frac{\partial u_i}{\partial x_j} - \frac{\partial u_j}{\partial x_i}\right) \quad \text{asymmetric} \tag{1.8b}$$

S_{ij} and Ω_{ij} are the components that represent respectively length change and overall rotation. A deformation requires relative distance between two points of a line to change. Since Ω_{ij} do not contribute to length change, they are eliminated from the strain analysis. Consider the elemental material length d**x** and its deformation d**u**. The new length d**x**′ and its square value are written as

$$\begin{aligned}
&\mathrm{d}\mathbf{x}' = \mathrm{d}\mathbf{x} + \mathrm{d}\mathbf{u}\\
&(\mathrm{d}x_i{}')^2 = (\mathrm{d}x_i)^2 + 2\mathrm{d}x_i\mathrm{d}u_i + (\mathrm{d}u_i)^2 \quad \text{since } (\mathrm{d}u_i)^2 \approx 0\\
&(\mathrm{d}x_i{}')^2 - (\mathrm{d}x_i)^2 \approx 2\mathrm{d}x_i\mathrm{d}u_i\\
&(\mathrm{d}x_i{}')^2 - (\mathrm{d}x_i)^2 \approx 2\frac{\partial u_i}{\partial x_j}\mathrm{d}x_i\mathrm{d}x_j
\end{aligned} \tag{1.9}$$

Since interchanging indice i and j gives the same result, therefore

$$\begin{aligned}
(\mathrm{d}\mathbf{l})^2 = (\mathrm{d}\mathbf{x}')^2 - (\mathrm{d}\mathbf{x})^2 &\approx \left(\frac{\partial u_i}{\partial x_j} + \frac{\partial u_j}{\partial x_i}\right)\mathrm{d}x_i\mathrm{d}x_j\\
&\approx 2S_{ij}\mathrm{d}x_i\mathrm{d}x_j
\end{aligned} \tag{1.10}$$

Thus, it is shown that length change d**l** gives rise to strain S_{ij}. Since S_{ij} depends on the coordinates of a material point, it is a tensor of rank 2. Besides, as S_{ij} represents the symmetric components in the displacements gradients $\partial u_i/\partial x_j$, therefore $S_{ij} = S_{ji}$. The components of strain can be divided into dilatation $(i = j)$ and shear $(i \neq j)$. Dilatation S describes the increase of volume, given by the divergence of deformation **u**.

$$S = S_{ii} = \nabla \cdot \mathbf{u} = \frac{\partial u_i}{\partial x_i} \tag{1.11}$$

1.3.2 Stress

An external force applied on a rigid body produces stress on its surface, for instance when a rod of cross section A is pulled by an axial force F, there is a stress of F/A acting on its end facet. For a rigid body of an arbitrary shape as illustrated in Fig 1.3, each infinitesimal surface ds is subjected to a mechanical stress **T**, defined as force per unit area d**F**/ds, note that **T** is not necessarily aligned to the unit vector of surface normal **n**. Thus, stress acting on each surface ds is written as $\mathbf{T}\cdot\mathbf{n}$ or in tensor notation $T_{ik}n_k$. Stress is then a tensor of rank 2 as it depends on **n**. In continuum mechanics, the total external force exerted on the body is equal to the summation of stress $T_{ik}n_k$ over each ds. On the other hand, the total internal force acting on

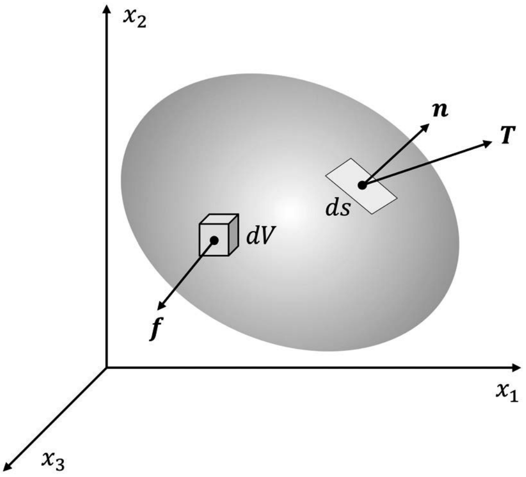

Figure 1.3 – Illustration of a 3D solid at equilibrium. Stress **T** acting on an infinitesimal surface ds with normal vector **n** and the internal volume force $\mathbf{f}_i$ acting on a infinitesimal volume dV.

the body is the summation of local volume force $\mathbf{f}_i$ acting on each infinitesimal volume $\mathrm{d}V$. In equilibrium, the relationship can be written as

$$F = \int_s \mathbf{T} \cdot \mathbf{n}\, \mathrm{d}s + \int_V \mathbf{f}_i\, \mathrm{d}V = 0 \tag{1.12}$$

Applying Gauss's theorem to the stress term yield the internal volume force **f**, which is equal to the negative divergence of stress.

$$\begin{aligned} \mathbf{f} &= -\nabla \cdot \mathbf{T} \\ f_i &= -\frac{\partial T_{ik}}{\partial x_k} \end{aligned} \tag{1.13}$$

When stress T_{ik} is aligned to one of the axes, it represents volume force in direction x_i acting on the surface with normal in direction x_k. In the absence of an applied torque to the body, there is no rotational stress components, therefore stress tensor is symmetric, $T_{ik} = T_{ki}$.

For the dynamic case, consider the body is subjected to an external force F. From Newton's law of motion, force is a product of mass and acceleration, $F = ma$. Using density ρ (mass per unit volume) and second derivative of the material displacement **u**. Eq. 1.12 is rewritten as

$$\frac{\partial T_{ik}}{\partial x_k} + f_i = \rho \frac{\partial^2 u_i}{\partial t^2} \tag{1.14}$$

Equation 1.14 is known as the elastodynamic equation, which describes the propagation of acoustic wave in an elastic material.

1.3.3 Stiffness tensor

Strain and stress of an elastic solid can be related by Hookes's law, which states that the force required to compress or extend a spring is a linear function of the elongation x, given as $F = kx$, where the gradient k is the spring's property called stiffness. An elastic solid can be viewed as a spring, when a small force is applied, the atomic lattice is lengthened by a small amount. As the force is lifted, the strong inter-atomic force returns the atomic lattice to its initial state. In a solid, stress, which represents the divergence of force is a function of strain, which represents the elongation. Stress can be expanded by Taylor series around strain $S = 0$:

$$T_{ij}(S) = T_{ij}(0) + \frac{\partial T_{ij}(0)}{\partial S_{kl}} S_{kl} + \frac{\partial^2 T_{ij}(0)}{\partial S_{kl} \partial S_{mn}} S_{kl} S_{mn} ... \tag{1.15}$$

Since $T_{ij}(0) = 0$ and assuming linear relationship (first order of Taylor expansion). Stress is defined as

$$T_{ij} = c_{ijkl} S_{kl} \tag{1.16a}$$

$$c_{ijkl} = \left(\frac{\partial T_{ij}}{\partial S_{kl}} \right)_{S_{kl}=0} \tag{1.16b}$$

where c_{ijkl} is the stiffness tensor, rank 4, which describes the relationships between stress and strain tensors in a linear elastic solid. A rank 4 tensor has $3^4 = 81$ components. Since both tensors T_{ij} and S_{kl} are symmetric, swapping the indices ij or kl does not affect the tensor.

$$c_{ijkl} = c_{jikl} = c_{ijlk} \tag{1.17}$$

Considering the equality above, the two terms in strain are equal, thus stress is

$$T_{ij} = c_{ijkl} \frac{\partial u_k}{\partial x_l} \tag{1.18}$$

Because of the symmetry, indices ij and kl can be reduced to 6 sets of combinations.

$$\begin{aligned} &(11) \leftrightarrow (1) \\ &(22) \leftrightarrow (2) \\ &(33) \leftrightarrow (3) \\ &(23) = (32) \leftrightarrow (4) \\ &(13) = (31) \leftrightarrow (5) \\ &(12) = (21) \leftrightarrow (6) \end{aligned} \tag{1.19}$$

Hence c_{ijkl} is contracted to $c_{\alpha\beta}$ ($6 \times 6 = 36$ elements matrix) where α corresponds to ij and β corresponds to kl. Then, the stiffness tensor can be written as a matrix of two indices.

$$T_\alpha = c_{\alpha\beta} S_\beta \tag{1.20}$$

Note that each symmetrical component of S_{kl} in Eq. 1.19 appears twice. Thus S_β should be written as

$$\begin{aligned}
S_1 &= S_{11} \\
S_2 &= S_{22} \\
S_3 &= S_{33} \\
S_4 &= 2S_{23} = 2S_{32} \\
S_5 &= 2S_{13} = 2S_{31} \\
S_6 &= 2S_{12} = 2S_{21}
\end{aligned} \tag{1.21}$$

The number of elements in stiffness matrix can be further reduced. Consider adiabatic or isothermal conditions (discussed in the next section), the stiffness matrix becomes symmetric:

$$c_{\alpha\beta} = c_{\beta\alpha} \tag{1.22}$$

This reduces the total distinct elements to 21, representing the richest possible stiffness matrix of a material, which has a triclinic lattice structure.

$$c_{\alpha\beta} = \begin{bmatrix} c_{11} & c_{12} & c_{13} & c_{14} & c_{15} & c_{16} \\ c_{12} & c_{22} & c_{23} & c_{24} & c_{25} & c_{26} \\ c_{13} & c_{23} & c_{33} & c_{34} & c_{35} & c_{36} \\ c_{14} & c_{24} & c_{34} & c_{44} & c_{45} & c_{46} \\ c_{15} & c_{25} & c_{35} & c_{45} & c_{55} & c_{56} \\ c_{16} & c_{26} & c_{36} & c_{46} & c_{56} & c_{66} \end{bmatrix} \tag{1.23}$$

For an isotropic material, the stiffness matrix can be further simplified, this will be discussed in the subsection of isotropic solid.

1.3.4 Elastic energy

As an elastic solid is deformed, work is done and stored as potential energy. An infinitesimal work done by the mechanical force is defined as $\mathrm{d}w = f_i \, \mathrm{d}u_i$. The rate of work done is then given by $\mathrm{d}w/\mathrm{d}t = f_i \, \dot{u}_i$. Replacing f_i using the elastodynamic equation in Eq. 1.14 gives

$$\begin{aligned}
\frac{\mathrm{d}w}{\mathrm{d}t} &= \rho \ddot{u}_i \dot{u}_i - \frac{\partial T_{ij}}{\partial x_j} \dot{u}_i \\
&= \rho \ddot{u}_i \dot{u}_i + T_{ij} \frac{\partial \dot{u}_i}{\partial x_j} + \frac{\partial}{\partial x_j} \left(-T_{ij} \dot{u}_i \right)
\end{aligned} \tag{1.24}$$

The three terms on the right hand side of Eq. 1.24 represents the kinetic, potential energy and the Poynting vector, respectively. The first term is the time derivative of the kinetic energy, given by

$$e_k = \frac{1}{2}\rho \dot{u}_i{}^2 \tag{1.25}$$

The second term is related to the potential energy

$$\frac{\mathrm{d}e_p}{\mathrm{d}t} = T_{ij}\frac{\partial \dot{u}_i}{\partial x_j} \tag{1.26}$$

Since strain tensor is symmetric $S_{ij} = S_{ji}$, the differential change of potential energy is

$$\mathrm{d}e_p = T_{ij}\mathrm{d}S_{ij} \tag{1.27}$$

The third term is related to Poynting vector $P = -T_{ij}\dot{u}_i$, which represents the energy flux. The transfer of energy is described by the first law of thermodynamics

$$\mathrm{d}U = \partial w + \partial Q \tag{1.28}$$

where $\mathrm{d}U$ is the change of internal energy, w is the work done and ∂Q is the heat change. According to the second law of thermodynamics, heat change ∂Q is equal to the product of temperature and entropy change $\mathrm{d}\sigma$.

$$\partial Q = \theta \mathrm{d}\sigma \tag{1.29}$$

Let's consider work done w is equal to the potential energy change $\mathrm{d}e_p$. Substitute Eq. 1.27 and Eq. 1.29 into Eq. 1.28 gives

$$\mathrm{d}U = \theta\mathrm{d}\sigma + T_{ij}\mathrm{d}S_{ij} \tag{1.30}$$

In the adiabatic condition, where entropy σ is constant, stress T_{ij} inferred from Eq. 1.30 is

$$T_{ij} = \left(\frac{\partial U}{\partial S_{ij}}\right)_{(\sigma)} \tag{1.31}$$

This equation shows that in the absence of heat transfer, stress is equal to the change of internal energy per unit strain. In addition, strain is in the same directions as stress. Substituting Eq. 1.31 into Eq. 1.16 yields

$$c^{(\sigma)}_{ijkl} = \left(\frac{\partial^2 U}{\partial S_{ij}\partial S_{kl}}\right)_{(\sigma)} = c^{(\sigma)}_{klij} \tag{1.32}$$

Since interchanging the indices ij and kl does not produce a different result, the stiffness matrix is found to be symmetrical, as mentioned in the previous subsection. This condition is also valid for isothermal case using similar derivation with $\partial Q = \sigma\mathrm{d}\theta$. As for obtaining the total potential energy, consider Eq. 1.30 and replacing T_{ij} with Eq. 1.16

$$\mathrm{d}U = \theta \mathrm{d}\sigma + c_{ijkl}^{(\sigma)} S_{kl} \mathrm{d}S_{ij} \tag{1.33}$$

Based on the symmetrical property of stiffness matrix, it can be written as

$$\begin{aligned} \mathrm{d}U &= \theta \mathrm{d}\sigma + \frac{1}{2}\left(c_{ijkl}^{(\sigma)} S_{kl} \mathrm{d}S_{ij} + c_{klij}^{(\sigma)} S_{ij} \mathrm{d}S_{kl}\right) \\ &= \theta \mathrm{d}\sigma + \frac{1}{2} c_{ijkl}^{(\sigma)} \mathrm{d}\left(S_{ij} S_{kl}\right) \end{aligned} \tag{1.34}$$

Then, the internal energy U is obtained as

$$U(\sigma, S) = U_0(\sigma) + \frac{1}{2} c_{ijkl}^{(\sigma)} S_{ij} S_{kl} \tag{1.35}$$

Assume that heat remains unchanged in its initial state, the potential energy is therefore the product of strain and stress

$$e_p = \frac{1}{2} c_{ijkl} S_{ij} S_{kl} = \frac{1}{2} T_{ij} S_{ij} \tag{1.36}$$

1.3.5 Isotropic solid

In general, the stiffness tensor of an elastic material depends on its geometrical orientation. However, for an isotropic solid, the stiffness tensor is invariant to rotation, which means its elastic property is the same as seen from different angles. By applying a tensor rotation, all components of the stiffness tensor vary except for the Kronecker deltas $\delta_{ij}\delta_{kl}$. Because of the symmetry $\delta_{ij} = \delta_{ji}$, there are only three combinations.

$$\begin{aligned} &\delta_{ij}\delta_{kl} \\ &\delta_{ik}\delta_{jl} \\ &\delta_{il}\delta_{jk} \end{aligned} \tag{1.37}$$

Thus, the stiffness tensor can be written as

$$c_{ijkl} = \lambda \delta_{ij}\delta_{kl} + \mu_1 \delta_{ik}\delta_{jl} + \mu_2 \delta_{il}\delta_{jk} \tag{1.38}$$

Because of the symmetry given in Eq. 1.17, $\delta_{ik}\delta_{jl}$ is equal to $\delta_{il}\delta_{jk}$, thus μ_1 and μ_2 can be combined into a single parameter μ.

$$c_{ijkl} = \lambda \delta_{ij}\delta_{kl} + \mu\left(\delta_{ik}\delta_{jl} + \delta_{il}\delta_{jk}\right) \tag{1.39}$$

where λ and μ are the Lamé constants. By iterating the indices $ijkl$ and writing c_{ijkl} in the contracted notation $c_{\alpha\beta}$, the following elements are related to one another and expressed in λ and μ, the rest vanishes because of the odd combinations where one of the Kronecker deltas is zero, for instance $c_{26} = c_{2212} = 0$.

$$c_{11} = c_{22} = c_{33} = \lambda + 2\mu \tag{1.40a}$$

$$c_{12} = c_{23} = c_{13} = \lambda \tag{1.40b}$$

$$c_{44} = c_{55} = c_{66} = \mu = \frac{(c_{11} - c_{12})}{2} \tag{1.40c}$$

Only three distinct elements are present, c_{11}, c_{12} and c_{44}. Hence, the relation between stress and strain of an isotropic solid is written as

$$\begin{bmatrix} T_{xx} \\ T_{yy} \\ T_{zz} \\ T_{yz} \\ T_{xz} \\ T_{xy} \end{bmatrix} = \begin{bmatrix} c_{11} & c_{12} & c_{12} & 0 & 0 & 0 \\ c_{12} & c_{11} & c_{12} & 0 & 0 & 0 \\ c_{12} & c_{12} & c_{11} & 0 & 0 & 0 \\ 0 & 0 & 0 & c_{44} & 0 & 0 \\ 0 & 0 & 0 & 0 & c_{44} & 0 \\ 0 & 0 & 0 & 0 & 0 & c_{44} \end{bmatrix} \begin{bmatrix} S_{xx} \\ S_{yy} \\ S_{zz} \\ 2S_{yz} \\ 2S_{xz} \\ 2S_{xy} \end{bmatrix} \tag{1.41}$$

Also, the elements of elastic constant, c_{11} and c_{12}, can be related to the Young's modulus E and Poisson's ratio σ of the isotropic medium by

$$c_{11} = \frac{E(1-\sigma)}{(1+\sigma)(1-2\sigma)} \tag{1.42a}$$

$$c_{12} = \frac{E\sigma}{(1+\sigma)(1-2\sigma)} \tag{1.42b}$$

It is helpful to further simplify the stress tensor to the normal and tangential components. The normal component is expressed as

$$\begin{aligned} T_{ii} &= c_{iikl} S_{kl} = \left(\lambda \delta_{kl} + 2\mu \delta_{ik} \delta_{il}\right) S_{kl} \\ &= \lambda \left(S_{11} + S_{22} + S_{33}\right) + 2\mu S_{ii} \end{aligned} \tag{1.43}$$

where $S = S_{11} + S_{22} + S_{33}$ is the dilatation as given in Eq. 1.11. For the tangential components where $i \neq j$, it is expressed as

$$\begin{aligned} T_{ij} &= c_{ijkl} S_{kl} = \mu \left(\delta_{ik} \delta_{jl} + \delta_{il} \delta_{jk}\right) S_{kl} \\ &= 2\mu S_{ij} \end{aligned} \tag{1.44}$$

Combining both Eq. 1.43 and Eq. 1.44 yield

$$T_{ij} = \lambda S \, \delta_{ij} + 2\mu S_{ij} \tag{1.45}$$

This equation relates stress to strain in an isotropic material by the Lamé constants and reduce the indices to 2.

1.3.6 Wave equation

Elastic wave propagation is described by the elastodynamic equation (Eq. 1.14). Neglecting the internal force, it is written as

$$\rho \frac{\partial^2 u_i}{\partial t^2} = \frac{\partial T_{ij}}{\partial x_j} \tag{1.46}$$

Substituting stress T_{ij} expressed in Eq. 1.18 into Eq. 1.46 yield

$$\rho \frac{\partial^2 u_i}{\partial t^2} = c_{ijkl} \frac{\partial^2 u_k}{\partial x_j \partial x_l} \tag{1.47}$$

The acoustic wave propagation is obtained by solving Eq. 1.47 based on the stiffness tensor c_{ijkl} of the medium.

Consider the case of an isotropic solid, stress T_{ij} is given by Eq. 1.45. Using the expression of strain given in Eq. 1.8 and replacing $\lambda = (c_{11} - 2c_{44})$ and $\mu = c_{44}$ yields the following equation.

$$\begin{aligned} T_{ij} &= (c_{11} - 2c_{44})\, S\delta_{ij} + 2c_{44} S_{ij} \\ &= (c_{11} - 2c_{44})\, S\delta_{ij} + c_{44} \left(\frac{\partial u_i}{\partial x_j} + \frac{\partial u_j}{\partial x_i} \right) \end{aligned} \tag{1.48}$$

Stress T_{ij} obtained here is then substituted into the wave equation (Eq. 1.46). S is replaced with dilatation (Eq. 1.11).

$$\rho \frac{\partial^2 u_i}{\partial t^2} = \frac{\partial}{\partial x_i} \left[(c_{11} - 2c_{44}) \frac{\partial u_i}{\partial x_i} \right] + c_{44} \frac{\partial^2 u_i}{\partial x_j^2} + c_{44} \frac{\partial}{\partial x_i} \left(\frac{\partial u_j}{\partial x_j} \right) \tag{1.49}$$

Followed by expressing Eq. 1.49 in the vector form.

$$\rho \frac{\partial^2 \mathbf{u}}{\partial t^2} = (c_{11} - c_{44})\, \nabla (\nabla \cdot \mathbf{u}) + c_{44} \nabla^2 \mathbf{u} \tag{1.50}$$

In order to decouple this differential equation, the solution is assumed to contain a scalar potential $\nabla\phi$ and a vector potential $\nabla \wedge \boldsymbol{\psi}$ terms, given as

$$\mathbf{u} = \nabla\phi + \nabla \wedge \boldsymbol{\psi} \tag{1.51}$$

Substituting Eq. 1.51 into Eq. 1.50 and using the following vector calculus identities

$$\nabla \wedge (\nabla\phi) = 0 \tag{1.52a}$$

$$\nabla \cdot (\nabla \wedge \boldsymbol{\psi}) = 0 \tag{1.52b}$$

results in the following equation.

$$\rho\frac{\partial^2\nabla\phi}{\partial t^2}+\rho\frac{\partial^2\left(\nabla\wedge\psi\right)}{\partial t^2}=\left(c_{11}-c_{44}\right)\nabla\left(\nabla^2\phi\right)+c_{44}\nabla^2\left(\nabla\phi\right)+c_{44}\nabla^2\left(\nabla\wedge\boldsymbol{\psi}\right) \tag{1.53}$$

This equation can be separated into two parts, the scalar and vector variables.

$$\nabla\left(\rho\frac{\partial^2\phi}{\partial t^2}-c_{11}\nabla^2\phi\right)+\nabla\wedge\left(\rho\frac{\partial^2\boldsymbol{\psi}}{\partial t^2}-c_{44}\nabla^2\boldsymbol{\psi}\right)=0 \tag{1.54}$$

Since $\nabla\wedge(\nabla\phi)=0$, ϕ is a scalar field. Likewise, given $\nabla\cdot(\nabla\wedge\boldsymbol{\psi})=0$, $\boldsymbol{\psi}$ is a vector field. The scalar equation represents the longitudinal wave whereas the vector equation represents the shear wave. The two equations are independent of each other.

$$\rho\frac{\partial^2\phi}{\partial t^2}-c_{11}\nabla^2\phi=0 \tag{1.55a}$$

$$\rho\frac{\partial^2\boldsymbol{\psi}}{\partial t^2}-c_{44}\nabla^2\boldsymbol{\psi}=0 \tag{1.55b}$$

The significance of Eqs. 1.55 is that longitudinal and shear waves of an isotropic medium propagate independent of each other at their respective velocities, V_{L} and V_{T}, given by

$$V_{\mathrm{L}}=\sqrt{\left(\frac{c_{11}}{\rho}\right)} \tag{1.56a}$$

$$V_{\mathrm{T}}=\sqrt{\left(\frac{c_{44}}{\rho}\right)}=\sqrt{\left(\frac{\left(c_{11}-c_{12}\right)}{2\rho}\right)} \tag{1.56b}$$

Since c_{12} is positive, the following relation is obtained

$$V_{\mathrm{T}}<\frac{V_{\mathrm{L}}}{\sqrt{2}} \tag{1.57}$$

which means the velocity of shear wave is always less than the velocity of longitudinal wave divided by $\sqrt{2}$ in any isotropic medium. It follows that the displacement vector $\mathbf{u}$ can be decomposed into a scalar field u_{L} corresponds to the longitudinal wave and a vector field $\mathbf{u}_{\mathrm{T}}$ corresponds to the shear wave, given by

$$\mathbf{u}=u_{\mathrm{L}}+\mathbf{u}_{\mathrm{T}} \tag{1.58}$$

Substitute Eq. 1.58 into Eq. 1.50 and include the respective velocities, V_{L} and V_{T} leads to the following two equations which confirms the two independent propagations u_{L} and $\mathbf{u}_{\mathrm{T}}$.

$$\frac{\partial^2 u_{\mathrm{L}}}{\partial t^2}-V_{\mathrm{L}}^2\nabla^2 u_{\mathrm{L}}=0 \tag{1.59a}$$

$$\frac{\partial^2\mathbf{u}_{\mathrm{T}}}{\partial t^2}-V_{\mathrm{T}}^2\nabla^2\mathbf{u}_{\mathrm{T}}=0 \tag{1.59b}$$

1.3.7 Attenuation

The stress and strain relation in Eq. 1.16 implies that stress responds instantaneously to the change of strain. In reality, the stress response is delayed and the acoustic wave is attenuated during propagation. Therefore, a loss term is introduced into the Hooke's law.

$$T_{ij} = c_{ijkl} S_{kl} + \eta_{ijkl} \frac{\partial S_{kl}}{\partial t} \tag{1.60}$$

where η is the viscosity constant with units $\mathrm{N} \cdot \mathrm{s}/m^2$. Substitute Eq. 1.60 into 1.47 the following equation is obtained

$$\rho \frac{\partial^2 u_i}{\partial t^2} = c_{ijkl} \frac{\partial^2 u_l}{\partial x_j \partial x_k} + \eta_{ijkl} \frac{\partial^3 u_l}{\partial x_j \partial x_k \partial t} \tag{1.61}$$

The tensor η_{ijkl} implies that a material is characterized by several relaxation times depending on the nature of the wave and the propagation direction. For isotropic material, the components of viscosity tensor reduce to η_{11} and η_{44} for compression and shear waves, respectively. Thus, Eq. 1.61 simplifies to two independent equations of compression and shear waves

$$\rho \frac{\partial^2 u_\mathrm{L}}{\partial t^2} = c_{11} \frac{\partial^2 u_\mathrm{L}}{\partial x_i^2} + \eta_{11} \frac{\partial}{\partial t} \left(\frac{\partial^2 u_\mathrm{L}}{\partial x_i^2} \right) \tag{1.62a}$$

$$\rho \frac{\partial^2 u_\mathrm{T}}{\partial t^2} = c_{44} \frac{\partial^2 u_\mathrm{T}}{\partial x_i^2} + \eta_{44} \frac{\partial}{\partial t} \left(\frac{\partial^2 u_\mathrm{T}}{\partial x_i^2} \right) \tag{1.62b}$$

1.3.8 Cylindrical waveguide

Cylindrical coordinate consists of three unit vectors **r**, $\boldsymbol{\theta}$ and **z** as illustrated in Fig. 1.4. The dispersion relation for an isotropic cylindrical waveguide is obtained by solving the wave equations (Eqs. 1.55), rewritten here as

$$\nabla^2 \phi - \frac{1}{V_L^2} \frac{\partial^2 \phi}{\partial t^2} = 0 \tag{1.63a}$$

$$\nabla^2 \boldsymbol{\psi} - \frac{1}{V_T^2} \frac{\partial^2 \boldsymbol{\psi}}{\partial t^2} = 0 \tag{1.63b}$$

The scalar potential ϕ is assumed to consist separable variables

$$\phi = f(r)\, g(\theta)\, \mathrm{e}^{i(\omega t - kz)} \tag{1.64}$$

where $f(r)$ is the radial profile and $g(\theta)$ is the azimuthal variation. Because of the periodicity of $g(\theta)$, $g(\theta + n2\pi) = g(\theta)$, therefore $g(\theta)$ is expressed in the form of $\sin(n\theta)$ or $\cos(n\theta)$ where n is an integer number ($n = 0, 1, 2, \ldots$). Substitute Eq. 1.64 into Eq. 1.63(a) and solve using the

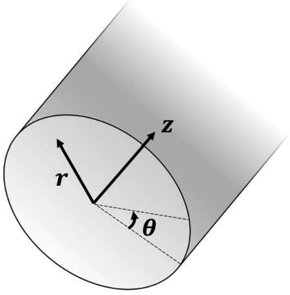

Figure 1.4 – Cylindrical coordinate system with unit vectors **r**, $\boldsymbol{\theta}$ and **z**.

scalar Laplacian $\nabla^2\phi$ given in Appendix A1 results in

$$\begin{aligned}&\frac{\partial^2 g}{\partial\theta^2}+n^2g=0\\&\frac{\partial^2 f}{\partial r^2}+\frac{1}{r}\frac{\partial f}{\partial r}+\left(\frac{\omega^2}{V_L^2}-k^2\right)f-\frac{n^2}{r^2}f=0\end{aligned}\tag{1.65}$$

This is a transformed Bessel differential equation, the corresponding standard solution is given in Appendix A1. Comparing with the standard solution, ϕ is obtained as

$$\phi=AJ_n\left(pr\right)\cos\left(n\theta\right)\mathrm{e}^{i(\omega t-kz)}\tag{1.66}$$

where p is given by

$$p^2=\frac{\omega^2}{V_L^2}-k^2\tag{1.67}$$

The differential equations of vector potential $\boldsymbol{\psi}$ is obtained by expanding the vector Laplacian term $\nabla\boldsymbol{\psi}$ in Eq. 1.63(b) as given in Appendix A3. This results in following equations

$$\nabla^2\psi_z+\frac{\omega^2}{V_T^2}\psi_z\tag{1.68a}$$

$$\nabla^2\psi_r-\frac{\psi_r}{r^2}-\frac{2}{r^2}\frac{\partial\psi_\theta}{\partial\theta}+\frac{\omega^2}{V_T^2}\psi_r\tag{1.68b}$$

$$\nabla^2\psi_\theta-\frac{\psi_\theta}{r^2}+\frac{2}{r^2}\frac{\partial\psi_r}{\partial\theta}+\frac{\omega^2}{V_T^2}\psi_\theta\tag{1.68c}$$

Equation 1.68(a) is similar to the scalar potential ϕ, therefore the solution is in the form of

$$\psi_z=BJ_n\left(qr\right)\sin\left(n\theta\right)\mathrm{e}^{i(\omega t-kz)}\tag{1.69}$$

where q is given by

$$q^2 = \frac{\omega^2}{V_T^2} - k^2 \tag{1.70}$$

For ψ_r and ψ_θ, the solution is assumed a priori as

$$\psi_r = \psi_r(r)\sin(n\theta)\,\mathrm{e}^{i(\omega t-kz)} \tag{1.71a}$$
$$\psi_\theta = \psi_\theta(r)\cos(n\theta)\,\mathrm{e}^{i(\omega t-kz)} \tag{1.71b}$$

The $\sin(n\theta)$ and $\cos(n\theta)$ difference is due to the coupling terms $\partial\psi_r/\partial\theta$ and $\partial\psi_\theta/\partial r$ in Eq. 1.68(b) and (c), which have different signs when differentiated with respect to θ. Substitute Eqs. 1.71 into Eqs. 1.68(b) and (c) results in

$$\frac{\partial^2\psi_r}{\partial r^2} + \frac{1}{r}\frac{\partial\psi_r}{\partial r} + \frac{1}{r^2}\left(-n^2\psi_r + 2n\psi_\theta - \psi_r\right) + q^2\psi_r = 0 \tag{1.72a}$$
$$\frac{\partial^2\psi_\theta}{\partial r^2} + \frac{1}{r}\frac{\partial\psi_\theta}{\partial r} + \frac{1}{r^2}\left(-n^2\psi_\theta + 2n\psi_r - \psi_\theta\right) + q^2\psi_\theta = 0 \tag{1.72b}$$

The second equation is exactly the same as the first except replacing ψ_r by ψ_θ. Subtracting and adding the two equations followed by finding the solutions using the transformed Bessel differential equation in Appendix A1 results in

$$\psi_r - \psi_\theta = 2CJ_{n+1}(qr) \tag{1.73a}$$
$$\psi_r + \psi_\theta = 2DJ_{n-1}(qr) \tag{1.73b}$$

and the following solutions are obtained

$$\psi_r = DJ_{n-1}(qr) + CJ_{n+1}(qr) \tag{1.74a}$$
$$\psi_\theta = DJ_{n-1}(qr) - CJ_{n+1}(qr) \tag{1.74b}$$

Considering stress free boundary at $r = a$ where a is the radius of the cylindrical waveguide, three simultaneous equations $T_{rr} = 0$, $T_{r\theta} = 0$ and $T_{rz} = 0$ can be written but there are four unknowns. Thus, by setting $\psi_r = -\psi_\theta$, D can be conveniently eliminated, leading to the following solution form.

$$\phi = AJ_n\left(pr\right)\cos(n\theta)\,\mathrm{e}^{i(\omega t-kz)} \tag{1.75a}$$
$$\psi_z = BJ_n\left(qr\right)\cos(n\theta)\,\mathrm{e}^{i(\omega t-kz)} \tag{1.75b}$$
$$\psi_r = CJ_{n+1}\left(qr\right)\sin(n\theta)\,\mathrm{e}^{i(\omega t-kz)} \tag{1.75c}$$
$$\psi_\theta = -CJ_{n+1}\left(qr\right)\cos(n\theta)\,\mathrm{e}^{i(\omega t-kz)} \tag{1.75d}$$

Subsequently, the stress terms will be determined. Firstly, the material displacement **u** as in

Eq. 1.51 is expanded using the vector calculus identities given in Appendix A1.

$$u_r = \frac{\partial \phi}{\partial r} + \frac{1}{r}\frac{\partial \psi_z}{\partial \theta} - \frac{\partial \psi_\theta}{\partial z} \tag{1.76a}$$

$$u_\theta = \frac{1}{r}\frac{\partial \phi}{\partial \theta} + \frac{\partial \psi_r}{\partial z} - \frac{\partial \psi_z}{\partial r} \tag{1.76b}$$

$$u_z = \frac{\partial \phi}{\partial z} + \frac{1}{r}\frac{\partial \left(r\psi_\theta\right)}{\partial r} - \frac{1}{r}\frac{\partial \psi_r}{\partial \theta} \tag{1.76c}$$

Then, the strain terms are obtained with Eq. 1.8 using the differentiation technique in cylindrical coordinate system.

$$S_{rr} = \frac{\partial u_r}{\partial r} \tag{1.77a}$$

$$S_{\theta\theta} = \frac{u_r}{r} + \frac{1}{r}\frac{\partial u_\theta}{\partial \theta} \tag{1.77b}$$

$$S_{zz} = \frac{\partial u_z}{\partial z} \tag{1.77c}$$

$$S_{r\theta} = S_{\theta r} = \frac{1}{2}\left(\frac{\partial u_\theta}{\partial r} - \frac{u_\theta}{r} + \frac{1}{r}\frac{\partial u_r}{\partial \theta}\right) \tag{1.77d}$$

$$S_{\theta z} = S_{z\theta} = \frac{1}{2}\left(\frac{1}{r}\frac{\partial u_z}{\partial \theta} + \frac{\partial u_\theta}{\partial z}\right) \tag{1.77e}$$

$$S_{rz} = S_{zr} = \frac{1}{2}\left(\frac{\partial u_r}{\partial z} + \frac{\partial u_z}{\partial r}\right) \tag{1.77f}$$

The dilatation is obtained from the addition of diagonal components in Eq. 1.77.

$$S = \frac{\partial u_r}{\partial r} + \frac{u_r}{r} + \frac{1}{r}\frac{\partial u_\theta}{\partial \theta} + \frac{\partial u_z}{\partial z} \tag{1.78}$$

Having the strain terms and dilatation, the stress terms can be expanded based on Eq. 1.45.

$$T_{rr} = \lambda S + 2\mu \frac{\partial u_r}{\partial r} \tag{1.79a}$$

$$T_{\theta\theta} = \lambda S + 2\mu \left(\frac{u_r}{r} + \frac{1}{r}\frac{\partial u_\theta}{\partial \theta}\right) \tag{1.79b}$$

$$T_{zz} = \lambda S + 2\mu \frac{\partial u_z}{\partial z} \tag{1.79c}$$

$$T_{r\theta} = \mu \left(\frac{\partial u_\theta}{\partial r} - \frac{u_\theta}{r} + \frac{1}{r}\frac{\partial u_r}{\partial \theta}\right) \tag{1.79d}$$

$$T_{\theta z} = \mu \left(\frac{1}{r}\frac{\partial u_z}{\partial \theta} + \frac{\partial u_\theta}{\partial z}\right) \tag{1.79e}$$

$$T_{rz} = \mu \left(\frac{\partial u_r}{\partial z} + \frac{\partial u_z}{\partial r}\right) \tag{1.79f}$$

The equations are solved by introducing stress free boundary conditions $T_{rr} = 0$, $T_{r\theta} = 0$ and $T_{rz} = 0$ at $r = a$, where a is the radius of the cylindrical waveguide. The dispersion relation associating ω and k is obtained from the nonzero determinant of the three simultaneous

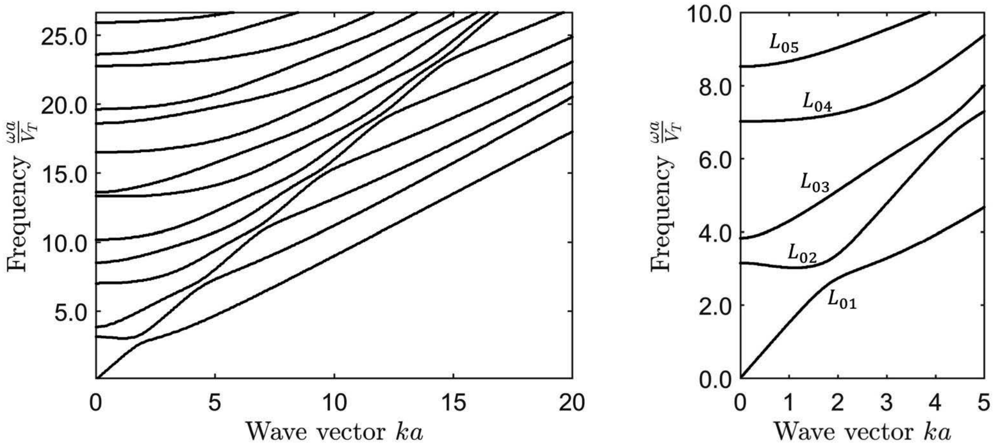

Figure 1.5 – The dispersion relation of compression wave $n = 0$ in silica cylindrical waveguide. The abscissa is the axial wave vector normalised by the radius a. The ordinate is the mode frequency normalised by the radius a and the transverse wave velocity V_T. The right diagram is the magnification of the left diagram in the region with small wave vector and frequency. Close to the zero axial wave vector, the acoustic modes are dispersive except for the L_{01} mode, their group velocities are close to zero whereas their phase velocities are enormous.

equations given by the boundary conditions. The roots of the determinant represent the acoustic modes. The integer n is the circumferential order. For the simple case of $n = 0$, which gives the compressional waves, the simultaneous equations are

$$\begin{bmatrix} -(\lambda(k^2+p^2)+2\mu p^2)J_0(pa)+2\mu\frac{p}{a}J_1(pa) & -2ik\mu\left(qJ_0(qa)+\frac{1}{a}J_1(qa)\right) \\ 2ik\mu pJ_1(pa) & -\mu(k^2-q^2)J_1(qa) \end{bmatrix} \begin{bmatrix} A \\ C \end{bmatrix} = \begin{bmatrix} 0 \\ 0 \end{bmatrix} \tag{1.80}$$

Using the equality $\lambda(k^2+p^2)+2\mu p^2 = \mu(q^2-k^2)$, the determinant is given by

$$\begin{aligned} &\frac{2p}{a}\left(q^2+k^2\right)J_1\left(pa\right)J_1\left(qa\right)-\left(q^2-k^2\right)^2 J_0\left(pa\right)J_1\left(qa\right) \\ &-4k^2pqJ_1\left(pa\right)J_0\left(qa\right)=0 \end{aligned} \tag{1.81}$$

This is the dispersion relation of axisymmetric acoustic mode, known as Pochhammer-Chree equation where p and q are from Eq. 1.67 and Eq. 1.70, respectively. The dispersion diagram relates the angular frequency ω to axial wave vector k, shown in Fig. 1.5. It is plotted based on Eq. 1.81 and the material parameters of silica (Appendix B). As k approaches zero, the acoustic modes are dispersive. The group velocity is close to zero whereas the phase velocity is extremely large. Each mode reaches a cutoff frequency at $k = 0$ with the exception of the fundamental mode L_{01}. As the axial wave vector k increases, the group velocity of all acoustic modes approaches the shear wave velocity V_T. Individual guided acoustic mode can be stimulated by pump and probe lights with difference of wave vectors Δk and angular frequencies $\Delta\omega$ that match the phase velocity of the acoustic mode.

1.4 Electrostriction

In backward SBS, light and acoustic waves interact mainly through electrostriction. The effect is attributed to the tendency of a material to become denser in the presence of an intense light [15]. As light intensity varies, the potential energy follows suites, producing gradient of energy in the medium. Mechanical force arises from this energy gradient and pull the local mass towards the region of higher light intensity.

The electrostrictive stress can be related to the photoelastic coefficients through a general analysis of energetics [66]. The mechanical energy change $\mathrm{d}U$ as given in Eq. 1.30 is assumed as equal to the electromagnetic energy change δu_{EM} under adiabatic or isothermal condition. Consider the time average electromagnetic energy density

$$u_{\mathrm{EM}} = \frac{1}{2} D_k E_k + \frac{1}{2} H_k B_k \tag{1.82}$$

By assuming that a locally induced material strain $S'_{ij} = S_{ij} + \delta S_{ij}$ transforms the electric displacement field D_j into D'_j while leaving all other field components unchanged. D_j and D'_j can be expressed in terms of dielectric tensor as

$$\begin{aligned} D_i &= \epsilon_0 \epsilon_{ij} E_j \\ D'_i &= \epsilon_0 \left(\epsilon_{ij} + \delta\epsilon_{ij}\right) E_j \\ \delta D_i &= D'_i - D_i = \epsilon_0 \delta\epsilon_{ij} E_j \end{aligned} \tag{1.83}$$

where ϵ_{ij} is the dielectric constant. Then, the change in u_{EM} is given as

$$\delta u_{\mathrm{EM}} = \frac{1}{2} \epsilon_0 \left(\delta\epsilon_{ij} E_j\right) E_i \tag{1.84}$$

For a photoelastic material, the variation of permittivity $\delta\epsilon$ due to strain is given by [70].

$$\delta\epsilon_{il} = -\epsilon_{ij} p_{jkmn} \epsilon_{kl} S_{mn} \tag{1.85}$$

where p_{jkmn} is the photoelastic tensor, which can be written in the contracted notation $p_{\alpha\beta}$. For an isotropic material, the matrix has only three distinct elements, p_{11}, p_{12} and p_{44}. Since permittivity ϵ_{ij} is diagonal for an isotropic material, $\epsilon_{ij} = \epsilon\delta_{ij}$, the corresponding strain variation is given by

$$\delta\epsilon_{kl} = -\epsilon^2 p_{ijkl} S_{ij} \tag{1.86}$$

Substitute into Eq. 1.84 yields

$$\delta u_{\mathrm{EM}} = -\frac{1}{2} \epsilon_0 \left[\epsilon^2 p_{ijkl} S_{ij}\right] E_k E_l \tag{1.87}$$

Then, differentiate both sides of Eq. 1.87 by S_{ij}, taking the limit $\delta S_{ij} \to 0$ and substitute

$\delta u_{\mathrm{EM}}/\delta S_{ij}$ by using Eq. 1.31 results in the time-averaged electrostrictively induced stress.

$$\langle T_{ij}^{\mathrm{es}}\rangle = -\frac{1}{2}\epsilon_0\left[\epsilon^2 p_{ijkl}\right]\langle E_k^{(1)}E_l^{(2)}\rangle \tag{1.88}$$

The components of stress induced through electrostriction [65] are given as

$$\begin{bmatrix} T_{xx} \\ T_{yy} \\ T_{zz} \\ T_{yz} \\ T_{xz} \\ T_{xy} \end{bmatrix} = -\frac{1}{2}\epsilon_0\epsilon^2 \begin{bmatrix} p_{11} & p_{12} & p_{12} & 0 & 0 & 0 \\ p_{12} & p_{11} & p_{12} & 0 & 0 & 0 \\ p_{12} & p_{12} & p_{11} & 0 & 0 & 0 \\ 0 & 0 & 0 & p_{44} & 0 & 0 \\ 0 & 0 & 0 & 0 & p_{44} & 0 \\ 0 & 0 & 0 & 0 & 0 & p_{44} \end{bmatrix} \begin{bmatrix} E_x^{(1)}E_x^{(2)*} \\ E_y^{(1)}E_y^{(2)*} \\ E_z^{(1)}E_z^{(2)*} \\ E_y^{(1)}E_z^{(2)*} + E_z^{(1)}E_y^{(2)*} \\ E_x^{(1)}E_z^{(2)*} + E_z^{(1)}E_x^{(2)*} \\ E_x^{(1)}E_y^{(2)*} + E_y^{(1)}E_x^{(2)*} \end{bmatrix} \tag{1.89}$$

The electrostrictive force f_i^{es} is given by the divergence of stress (Eq. 1.13), the vector components of f_i^{es} are given by

$$f_x^{\mathrm{es}} = \frac{\partial T_{xx}}{\partial x} + \frac{\partial T_{xy}}{\partial y} + \frac{\partial T_{xz}}{\partial z} \tag{1.90a}$$

$$f_y^{\mathrm{es}} = \frac{\partial T_{yx}}{\partial x} + \frac{\partial T_{yy}}{\partial y} + \frac{\partial T_{yz}}{\partial z} \tag{1.90b}$$

$$f_z^{\mathrm{es}} = \frac{\partial T_{zx}}{\partial x} + \frac{\partial T_{zy}}{\partial y} + \frac{\partial T_{zz}}{\partial z} \tag{1.90c}$$

Consider the optical field as a plane wave, the electric field component E_i in the propagating direction z is close to zero, $E_z \approx 0$. Furthermore, suppose the transverse electric field is aligned to y axis, the electric field in x direction becomes zero, $E_x = 0$. This leads to zero values for the stress components T_{ij} where $i \neq j$ whereas the components T_{ii} are given by

$$T_{xx}^{\mathrm{es}} = T_{zz}^{\mathrm{es}} = -\frac{1}{2}\epsilon_0\epsilon^2 p_{12}|E_y|^2 \tag{1.91a}$$

$$T_{yy}^{\mathrm{es}} = -\frac{1}{2}\epsilon_0\epsilon^2 p_{11}|E_y|^2 \tag{1.91b}$$

Since the field profile of a plane wave is transversally invariant, the differential terms in x and y directions of Eq.1.90 are canceled out, leaving behind a single term $\partial T_{zz}/\partial z$. Consider the variation of optical intensity as matching with the acoustic wave of wave vector q and frequency Ω, $E_y^2 = |E_y|^2 \exp i(\Omega t - qz)$, the electrostrictive force becomes

$$f_z^{\mathrm{es}} = \frac{\partial T_{zz}}{\partial z} = i\frac{1}{2}q\epsilon_0 n^4 p_{12}|E_y|^2 \tag{1.92}$$

This equation indicates that for an optical plane wave, the only nonzero force component is in the direction of propagation. The imaginary number i indicates that the electrostrictive force f^{es} is $\pi/2$ phase shift with respect to the variation of the optical field intensity. For the general description of acoustic wave propagation, the elastodynamic equation (Eq. 1.14 and Eq. 1.47) can be written in the following form:

$$\rho\frac{\partial^2 u_i}{\partial t^2} - c_{ijkl}\frac{\partial^2 u_k}{\partial x_j \partial x_l} = -\epsilon_0\epsilon^2 p_{ijkl}\frac{\partial}{\partial x_j}\left(E_k^{(1)}E_l^{(2)*}\right) \tag{1.93}$$

This elastodynamic equation which includes the contribution of electrostrictive stress is widely utilized in the finite element method (FEM) based numerical simulation of acoustic wave guidance in several guiding structures: surface acoustic wave in microfibre [12], transverse acoustic waves in photonic crystal fibre [11] and small core optical waveguides [52].

1.5 Brillouin scattering as optical nonlinearity

The elastic waves present in the optical fibre act as the source of optical nonlinearity that couples the participating optical waves. As the refractive index of optical fibre is perturbed by the propagating acoustic waves, energy is transferred between different optical frequency components. The nonlinear coupled equations of the conventional backward SBS are discussed here by including the photoelastic constant as the nonlinear parameter χ. The optical field involved in the interaction is $E(\mathbf{x},t),t) = E_1(\mathbf{x},t) + E_2(\mathbf{x},t)$, which is assumed to be weakly guided in the optical fibre and aligned to y direction, defined as

$$E_1(\mathbf{x},t) = E_0(r)A_1(z,t)e^{i(k_1 z-\omega_1 t)} + \text{c.c.} \tag{1.94a}$$

$$E_2(\mathbf{x},t) = E_0(r)A_2(z,t)e^{i(-k_2 z-\omega_2 t)} + \text{c.c.} \tag{1.94b}$$

$E_0(r)$ is the transverse mode profile. $A_1(z,t)$ and $A_2(z,t)$ are the slowly varying wave envelopes. Likewise, the acoustic field inside the medium is described by the material displacement.

$$u(\mathbf{x},t) = u_0(r)B(z,t)e^{i(qz-\Omega t)} + \text{c.c.} \tag{1.95}$$

Under perfect phase matching condition, acoustic frequency and wave vector are $\Omega = \omega_1 - \omega_2$ and $q = 2k_1$, respectively. Taking the compression wave equation with loss term as in Eq. 1.62(a) and combine with the electrostrictive force term in Eq. 1.93, the acoustic wave equation is rewritten here as

$$\frac{\partial^2 u}{\partial t^2} - V_L^2\frac{\partial^2 u}{\partial x_i^2} - \Gamma\frac{\partial}{\partial t}\left(\frac{\partial^2 u}{\partial x_i^2}\right) = -\epsilon_0\chi\rho^{-1}\frac{\partial}{\partial x_i}\left(E_1E_2^*\right) \tag{1.96}$$

where Γ is the acoustic damping parameter, $\Gamma = \eta/\rho$, χ is the nonlinear parameter, $\chi = \epsilon^2 p_{12} = n^4 p_{12}$ and ϵ_0 is the dielectric constant. The wave equation of optical field obtained from Maxwell's equations is given by

$$\nabla^2 E_i - \frac{1}{(c/n)^2}\frac{\partial^2}{\partial t^2}E_i = \frac{1}{\epsilon_0 c^2}\frac{\partial^2 P_i}{\partial t^2} \tag{1.97}$$

The acoustic mode solutions can be found from the eigenvalues of the acoustic wave equation (Eq. 1.96) by setting Γ and the electrostrictive force term to zero

$$\frac{\partial^2 u}{\partial t^2} - V_L^2 \frac{\partial^2 u}{\partial x_i^2} = 0 \tag{1.98}$$

Substituting Eq. 1.95 into Eq. 1.98 and expand the terms yield

$$\left(-2i\Omega\frac{\partial B}{\partial t} - \Omega^2 B\right) - V_L^2\left(B\nabla_\perp^2 + 2iq\frac{\partial B}{\partial z} - q^2 B\right) u_0(r) = 0 \tag{1.99}$$

where $\nabla_\perp^2$ is the Laplacian acting on the transverse field. The second derivative terms are ignored because the acoustic envelope $B(z,t)$ is a slowly varying term. Consider $B(z,t)$ as a constant, the following relation could be found

$$\nabla_\perp^2 u_0(r) = u_0(r)\left(q_a^2 - \frac{\Omega_B^2}{V_L^2}\right) \tag{1.100}$$

where q_a and Ω_B are respectively the propagation constant and the frequency of the acoustic eigenmodes. Substitute Eq. 1.95 into Eq. 1.96, replace $\nabla_\perp^2 u_0(r)$ using Eq.1.100 and consider $q \approx q_a$, the equation describing the evolution of the acoustic envelope $B(z,t)$ is

$$2i\Omega\frac{\partial B}{\partial t} + 2iqV_L^2\frac{\partial B}{\partial z} + B(\Omega^2 - \Omega_B^2 + i\Omega\Gamma_B) = -iq\epsilon_0\chi\rho^{-1}QA_1A_2^* \tag{1.101}$$

where the Brillouin linewidth Γ_B is defined as $\Gamma_B = \Omega_B^2\Gamma$ and Q is the overlap integral of optical and acoustic fields over the cross section, defined in [50]. Assume that the acoustic field envelope varies slowly in axial direction, the propagation term $\partial B/\partial z$ is neglected. Subsequently, consider the steady state condition $\partial B/\partial t = 0$, thus B can be written as

$$B = iq\epsilon_0\chi\rho^{-1}Q\frac{A_1A_2^*}{\Omega_B^2 - \Omega^2 - i\Omega\Gamma_B} \tag{1.102}$$

For the optical wave, two wave equations for each component E_1 and E_2 is obtained by substituting Eqs. 1.94 into Eq. 1.97, the second order derivative terms are neglected.

$$\frac{\partial A_1}{\partial z} + \frac{1}{c/n}\frac{\partial A_1}{\partial t} = \frac{1}{2ik\epsilon_0 c^2}\frac{\partial^2 P_1}{\partial t^2} \tag{1.103a}$$

$$-\frac{\partial A_2}{\partial z} + \frac{1}{c/n}\frac{\partial A_2}{\partial t} = \frac{1}{2ik\epsilon_0 c^2}\frac{\partial^2 P_2}{\partial t^2} \tag{1.103b}$$

The nonlinear polarisation P_{NL} is given by

$$P_{NL} = \epsilon_0\Delta\chi E(\mathbf{x},t) \approx \epsilon_0\Delta\epsilon E(\mathbf{x},t) \tag{1.104}$$

where $\Delta\epsilon$ is the permittivity change. For an isotropic material, $\Delta\epsilon$ is given by Eq. 1.86. Since the electric field vector is defined in y direction, the component of permittivity change $\Delta\epsilon_{ij}$

that affects E_y is $\Delta\epsilon_{yy}$, which is given by

$$\Delta\epsilon = \Delta\epsilon_{yy} = -\epsilon^2(p_{11}S_{yy} + p_{12}(S_{xx} + S_{zz})) \tag{1.105}$$

Assume that the variation of acoustic field ∂u in the transverse directions is small as compared to the longitudinal direction, the strain components S_{xx} and S_{yy} become zero, this result in

$$\begin{aligned}\Delta\epsilon &= -\epsilon^2 p_{12} S_{zz} \\ &= -\chi S_{zz}\end{aligned} \tag{1.106}$$

Thus, substituting Eq. 1.106 into Eq. 1.104 yields

$$P_{\mathrm{NL}} = -\epsilon_0 \chi S_{zz} E(\mathbf{x}, t) \tag{1.107}$$

The strain component S_{zz} is in the longitudinal direction, which is given by $S_{zz} = \partial u/\partial z$. Consider slowly varying acoustic field $\partial B/\partial z = 0$, so that $\partial u/\partial z = iqBu_0(r)\exp(i(qz - \Omega t))$, the nonlinear polarization $P_{\mathrm{NL}}^{(1)}$ and $P_{\mathrm{NL}}^{(2)}$ can then be written as

$$P_{\mathrm{NL}}^{(1)} = -\epsilon_0 \chi S_{zz} E(\mathbf{x}, t) = -iq\epsilon_0 \chi B u_0(r) E_2(\mathbf{x}, t) \tag{1.108a}$$
$$P_{\mathrm{NL}}^{(2)} = -\epsilon_0 \chi S_{zz}^* E(\mathbf{x}, t) = iq\epsilon_0 \chi B^* u_0(r) E_1(\mathbf{x}, t) \tag{1.108b}$$

Substituting Eqs. 1.108 into Eqs. 1.103, the resulting wave equations are

$$\frac{\partial A_1}{\partial z} + \frac{1}{c/n}\frac{\partial A_1}{\partial t} = \frac{q\omega\chi}{2nc} QBA_2 \tag{1.109a}$$
$$-\frac{\partial A_2}{\partial z} + \frac{1}{c/n}\frac{\partial A_2}{\partial t} = \frac{-q\omega\chi}{2nc} QB^* A_1 \tag{1.109b}$$

Consider steady state condition $\partial A/\partial t = 0$ and substitute B from Eq. 1.102 into Eq. 1.109, the following coupled amplitude equations can be obtained

$$\frac{\partial A_1}{\partial z} = \frac{iq^2\epsilon_0\omega\chi^2 Q^2}{2nc\rho} \frac{A_1|A_2|^2}{\Omega_{\mathrm{B}}^2 - \Omega^2 - i\Omega\Gamma_{\mathrm{B}}} \tag{1.110a}$$
$$\frac{\partial A_2}{\partial z} = \frac{-iq^2\epsilon_0\omega\chi^2 Q^2}{2nc\rho} \frac{A_2|A_1|^2}{\Omega_{\mathrm{B}}^2 - \Omega^2 + i\Omega\Gamma_{\mathrm{B}}} \tag{1.110b}$$

The intensity of light is defined as $I_i = 2n\epsilon_0 c A_i A_i^*$. Differentiating I_i with respect to z and replacing $\partial A_i/\partial z$ from Eqs. 1.110, the following coupled equations for the intensities of the two interacting waves are found, which are the same as in [15].

$$\frac{\mathrm{d}I_1}{\mathrm{d}z} = -gI_1I_2 \tag{1.111a}$$
$$\frac{\mathrm{d}I_2}{\mathrm{d}z} = -gI_1I_2 \tag{1.111b}$$

The SBS gain is given by

$$g = g_0 \frac{(\Gamma_{\mathrm{B}}/2)^2}{(\Omega_{\mathrm{B}} - \Omega)^2 + (\Gamma_{\mathrm{B}}/2)^2} \tag{1.112}$$

This is a Lorentzian function with linewidth Γ_{B}. The line centre gain factor is given by

$$g_0 = \frac{\chi^2 \omega^2 Q^2}{n V_L c^3 \rho \Gamma_{\mathrm{B}}} \tag{1.113}$$

For constant pump, the solution of Eq. 1.111 gives

$$I_2(z) = I_2(L) e^{g I_1 (L-z)} \tag{1.114}$$

In this case the Stokes wave injected into the medium at $z = L$ experiences exponential growth as it propagates through the medium. The coupled wave equations for conventional SBS provides a generic case which can be reformulated for the other types of Brillouin scatterings.

1.6 Classes of Brillouin scatterings

Brillouin scatterings can be broadly categorized into: backward Brillouin scatterings, surface Brillouin scattering, forward Brillouin scatterings and intermodal Brillouin scattering. The diversity of Brillouin scattering stems from the numerous interplay between optical fields and the guided acoustic wave while the governing physics on elastic wave and electrostriction remain the same. The classes of Brillouin scattering differ in terms of the direction of light scattering and the type of participating acoustic wave. The interaction between the optical and acoustic waves for several Brillouin scatterings genres are shown in Fig. 1.6 using the dispersion diagrams. The abscissa and ordinate represents the axial wave vector k and angular frequency ω of light wave, respectively. The phase matched acoustic wave is represented by dotted lines linking the optical waves.

The first discovered Brillouin scattering belongs to the backward SBS, commonly referred to as SBS because of the self-reinforcing nature of the scattering process. In backward SBS, light is back-scattered by the longitudinal compression acoustic wave, resulting in the frequency shifted scattered light that corresponds to the velocity of longitudinal acoustic wave in a material. SBS is efficient in optical fibres because of the perfect overlap of optical and acoustic fields along its entire length. At phase matching condition, the acoustic wave vector is approximately the wave vector difference of counter-propagating lights, $q \approx 2k_{\mathrm{op}}$ (Fig. 1.6(a)). SBS appears as a limiting factor for long haul fibre optics communication links as the pump light is depleted by the scattered Stokes light, which has to be overcome by techniques that reduce its efficiency such as random phase modulation of the pump light. Nevertheless, SBS emerges as a useful effect for distributed temperature and strain sensing owing to the sensitivity of sound velocity towards material property change and the back scattering process that relates the time-of-flight information to the local change of sensing parameter.

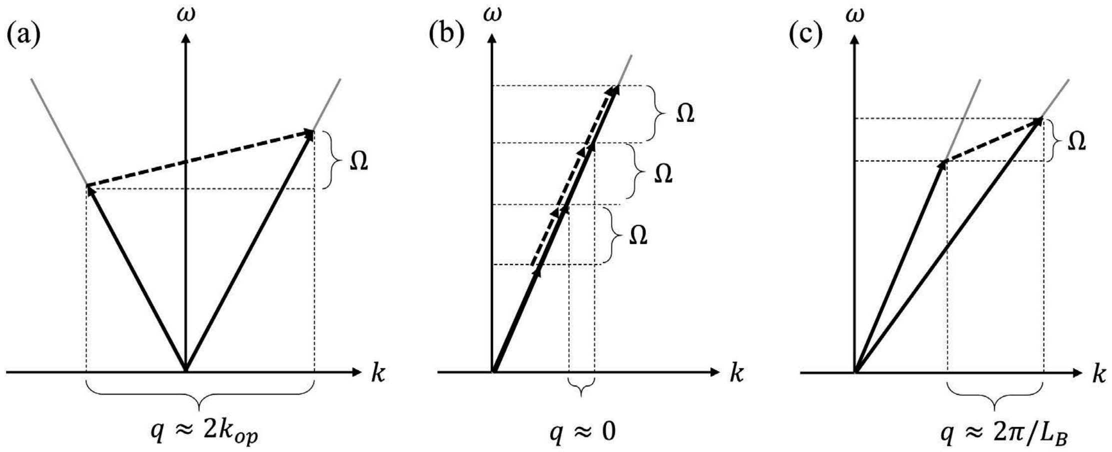

Figure 1.6 – Phase matching conditions and scattering directions of several classes of Brillouin scatterings elucidated using the dispersion diagrams. The (a) backward (b) forward and (c) intermodal stimulated Brillouin scattering. Solid and dotted arrows represent optical and acoustic waves, respectively.

Surface Brillouin scattering is an interesting phenomenon observed in small acoustic waveguides with dimension close to the range of the acoustic wavelength. It is first observed by J-C. Beugnot *et al.* in a tapered optical microfibre [12]. Due to the small ratio of fibre dimension to acoustic wavelength, the guided acoustic wave is subjected to contrasting elastic stiffness at the fibre boundary, changing its mode profile and propagating velocity. Besides, the optical field covers the entire cross-section in sub-micrometer dimension, this enables electrostriction to be efficient near the fibre boundary and surface acoustic wave manifests as a result. Having the characteristics of Rayleigh wave, surface acoustic wave in microfibre has material displacement that is decreasing rapidly from the fibre boundary and close to naught in the middle of the microfibre. The stimulation process follows that of SBS using counter-propagating pump and probe lights. Surface Brillouin scattering has also been observed in solid core photonic crystal fibre, where its air-filling factor has an impact on the surface Brillouin frequency shift [82]. Systematic study on the influence of diameter change on the resonance frequencies of several acoustic modes in microfibre has also been reported in [35]. In view of the concentration of material strain close to the boundary, surface Brillouin scattering is expected to be sensitive towards surface defects, coating thickness, etc.

Forward stimulated Brillouin scattering (FSBS), first reported by R. M. Shelby in 1984 using standard single-mode optical fibre [72], is the scattering of light by the transversally resonating acoustic waves. This scattering process occurs for very large axial acoustic phase velocity and exhibits multiple resonance frequencies which are determined by the fibre dimension (Fig. 1.6(b)). Because of the relaxed phase matching conditions, the scattered light can easily lead to higher order light scatterings [88]. Several nomenclatures of forward Brillouin scattering exist in literature which highlight different aspects of the scattering process: FSBS emphasizes on the forward direction of the scattered light and the directional reciprocity of the process. By introducing both pump and probe lights which are frequency separated by one of the scattering frequencies, the FSBS process is enhanced thus defined as a stimulated process; Guided acoustic wave Brillouin scattering (GAWBS) draws on the importance of acoustic wave confinement and guidance in the scattering process; Raman-like light scattering stresses the independence of Stokes frequency shift from the wavelength of optical pump, which is similar to Raman scattering. FSBS appears as a major noise source in the study of fibre optics soliton propagation due to the periodical phase modulation resulting from the lasting transverse acoustic resonances. However, recent development of an acoustic impedance sensor based on FSBS demonstrates that this scattering process could be otherwise useful for long distance material property sensing with minimalist modifications to current standard optical fibre (described further in Chapter 3).

Another variant of FSBS is the intermodal FSBS, first described by P. S. J. Russel *et al.* in 1991 [71]. The mechanism is quite different from the FSBS mentioned before despite the similarity in names. Intermodal FSBS is a collinear Brillouin scattering process that involves interaction of two co-propagating optical modes and the flexural acoustic wave (Fig. 1.6(c)). The beating between the two optical modes in a dual-mode fibre produces intensity variation that electrostrictively stimulates a flexural acoustic wave, which has wavelength corresponding to the intermodal optical beat length L_B. Interestingly, the propagating direction of the flexural acoustic wave can be reversed by interchanging the role of individual optical mode as pump or Stokes wave. Intermodal FSBS has been used to measure the modal beat length in few modes optical fibres [48].

Table 1.1 – Category of distributed Brillouin analyses

	Single-end access	Two-end access
Time-of-flight	BOTDR	BOTDA BEDS BDG
Frequency domain	BOFDR	BOFDA
Correlation	BOCDR	BOCDA PCBDS

Table 1.2 – Nomenclatures of distributed Brillouin measurement techniques

Acronym	Nomenclature	References
BOTDR	Brillouin optical time domain reflectometry	[42]
BOTDA	Brillouin optical time domain analysis	[42]
BOFDR	Brillouin optical frequency domain reflectometry	[55]
BOFDA	Brillouin optical frequency domain analysis	[34]
BOCDR	Brillouin optical correlation domain reflectometry	[57]
BOCDA	Brillouin optical correlation domain analysis	[44]
BEDS	Brillouin echoes distributed sensor	[33]
PCBDS	Phase correlation Brillouin distributed sensor	[90]
BDG	Brillouin dynamic grating	[78]

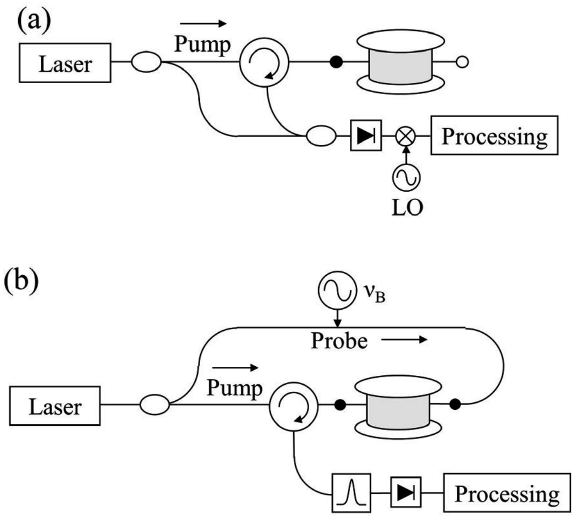

Figure 1.7 – Illustration of (a) single-end and (b) two-end access configurations.

1.7 Distributed analyses using backward SBS

Backward SBS is a powerful tool for realising distributed fibre sensor because of two factors: 1. The sound velocity in silica is sensitive towards strain and temperature. 2. The back-scattered light enables the position of Brillouin interaction to be resolved. The first distributed sensor based on backward Brillouin scattering was proposed by T. Horiguchi *et al.* in 1995 [42]. Since then, academic researches and industrial applications on distributed Brillouin sensors are growing at a fast rate. On the research front, most reported works are aiming to push the limits on the spatial resolution, distance range and the acquisition speed [56, 33, 62]. For industrial applications, the distributed Brillouin sensor is traditionally deployed in monitoring downhole drilling and is recently making inroads into the monitoring of infrastructures, pipelines as well as landslides. The myriads of distributed Brillouin sensing techniques reported in literature can be broadly categorized into the six most common groups as shown in Table 1.1 and are briefly discussed. The full nomenclatures, acronyms and the related references of several distributed Brillouin measurement techniques are listed in Table 1.2.

The single-end access configuration is the most convenient option for field test where laser is launched into the optical fibre through one end and the back-scattered light is routed by a circulator to detection, as illustrated in Fig. 1.7(a). Due to the weak Brillouin Stokes light for this configuration, a highly sensitive detection scheme is required. A coherent detection scheme is normally used where the back-scattered signal is optically mixed with a continuous wave (CW) laser and the detected beat signal is then electrically mixed with a microwave local oscillator whose frequency is detuned in small step over the resonance spectrum. The recorded signal is then proportional to the baseband amplitude of the beat signal. This type of configurations are usually referred to as "reflectometry" to draw the similarity with optical

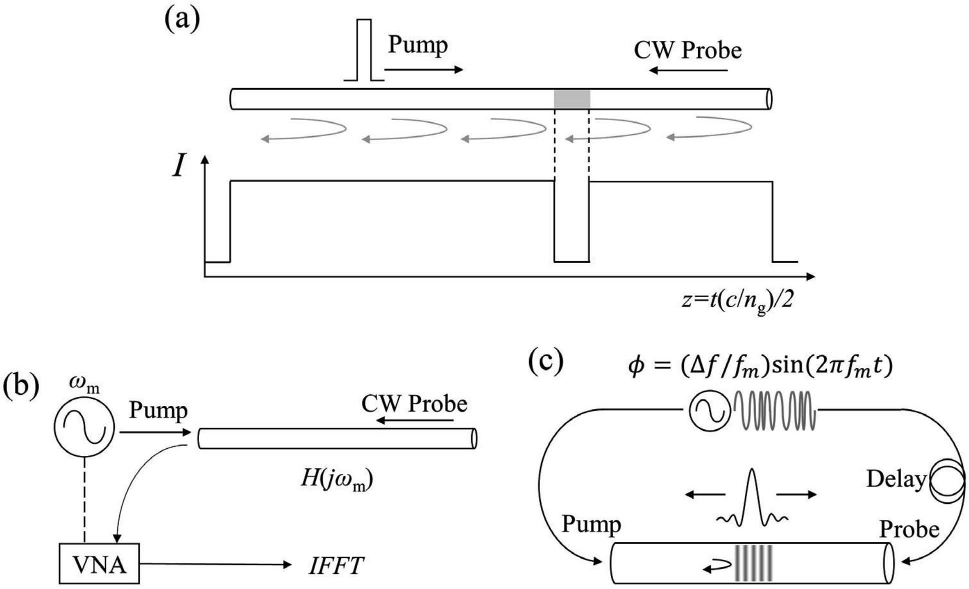

Figure 1.8 – Illustration of (a) time-of-flight, (b) frequency domain and (c) correlation measurement techniques.

time domain reflectometry (OTDR), which is a distributed measurement technique based on incoherent Rayleigh scattering that is widely used in measuring attenuation and identifying loss points in an optical fibre links.

For the two-end access configuration, counter propagating pump and probe lights from the same laser are respectively launched into the two ends of the optical fibre, as illustrated in Fig. 1.7(b). The frequency of the probe light is offset by instruments to correspond with the frequency of the Brillouin Stokes light and scanned in small frequency step across the resonance spectrum. Since the Brillouin interaction in the presence of pump and probe waves is certainly in the stimulated regime, the intensity of back-scattered light can be over 100 times the Rayleigh back-scattering intensity. The detection scheme includes a narrow bandwidth filter to select the Stokes light and the signal is then read by a photo-detector. This configuration is usually referred to as "analysis" to highlight the ability of reconstructing Brillouin spectrogram with high resolution frequency scan.

In time-of-flight measurement, an optical pulse is launched into the fibre and the time trace of Brillouin back-scattered light provides the information of interaction strength at each position in the fibre, illustrated in Fig. 1.8(a). The most common time-of-flight Brillouin measurement techniques are BOTDA and BOTDR. The record time t and interaction location z are related by

$$z = (c/n_g)\frac{t}{2} \tag{1.115}$$

where c is the speed of light in vacuum and n_g is the group index of light in the fibre. The spatial resolution Δz is related to the pulse duration Δt by

$$\Delta z = (c/n_g)\frac{\Delta t}{2} \tag{1.116}$$

Thus, Δz for Δt of 10 ns is around 1 m. Time-of-flight based measurement is popular for its simplicity in terms of implementation and data processing. However, the spatial resolution is limited to 1 m because it corresponds to the acoustic decay time in silica which is around 10 ns. In other words, an optical pulse shorter than 10 ns is insufficient to fully stimulate the acoustic wave. As in frequency domain, the detected spectrum is given by the convolution of acoustic resonance spectrum and the pulse spectrum. Thus, as Δt is shorter, the width of the pulse spectrum becomes broader, this smears out the detected Brillouin spectrum and affects the precision of the measured frequency shift. This problem can be overcome by several techniques: (i). BEDS-Launching a CW pump with a dark pulse or a π-phase shifted pulse so that the acoustic wave is pre-activated at all sensing points [33]; (ii) Brillouin dynamic grating-Acoustic waves are pre-activated in a polarization maintaining fibre and interrogated by an optical pulse launched in the orthogonal polarization and at a different wavelength.

The position-resolved Brillouin response can also be obtained through the frequency domain alternative. First proposed by D. Garus *et al.*, this type of measurement involves determining a complex transfer function $H(j\omega)$ from the amplitude ratio of counter propagating pump $X_p(j\omega)$ and probe $X_s(j\omega)$ waves at pump input side of the fibre, given by $H(j\omega) = X_s(j\omega)/X_p(j\omega)$. As illustrated in Fig. 1.8(b), the pump wave for a typical BOFDA is modulated by a frequency ω_m that is synchronized to the detection by a vector network analyzer (VNA), which returns the baseband transfer function $H(j\omega)$ of the sensing fibre. Then, the temporal response is obtained through inverse fast Fourier transform (IFFT) of $H(j\omega)$, from which the Brillouin response with respect to the location in the fibre can be recovered. The maximum range of detection is given by

$$L_{\max} = \frac{c}{2n_{\mathrm{g}}}\frac{1}{\Delta f_m} \tag{1.117}$$

where Δf_m is the scanning frequency step. The spatial resolution is given by

$$\Delta z = \frac{c}{2n_{\mathrm{g}}}\frac{1}{f_{m,\max} - f_{m,\min}} \tag{1.118}$$

where $f_{m,\max}$ and $f_{m,\min}$ are the maximum and minimum modulation frequencies, respectively. For small spatial resolution, the frequency scan has to cover a wide range whereas for long measurement range, the scanning frequency step has to be extremely small.

Since the generation of acoustic wave is not instantaneous in response to the optical excitation, Brillouin scattering is efficient only when the phase difference between pump and probe lights does not change during the interaction. Based on this fact, correlation measurements utilize counter-propagating pump and probe lights with common phase modulation pattern to create local correlation points with efficient Brillouin scattering. Elsewhere outside of the correlation points, Brillouin scattering is suppressed by the fast changing phase difference (see Fig. 1.8(c)). By varying the period of the frequency modulation, the positions of higher oder correlation peaks change. A delay fibre is usually used so that a higher order correlation peak is inside the sensing fibre. Correlation measurement method is first introduced by K. Hotate *et al.* using sinusoidal frequency modulation [44]. The method has the advantages of sub-meter spatial resolution and the flexibility to measure the Brillouin spectrum at a specific location without scanning the entire fibre. For the generic BOCDA, which uses sinusoidal frequency modulation, the measurement range is limited by the separation between correlation peaks d_m, given by

$$d_m = \frac{(c/n_{\mathrm{g}})}{2f_m} \tag{1.119}$$

where f_m is the modulation frequency. The spatial resolution Δz is given by

$$\Delta z = \frac{\Delta\nu_B}{f_m}\frac{(c/n_{\mathrm{g}})}{2\pi\Delta f} \quad f_m < \Delta\nu_B/2 \tag{1.120}$$

where ν_B is the Brillouin linewidth and Δf is the modulation amplitude of the laser frequency. To decrease Δz, either f_m or Δf should be increased. However, hiking up f_m leads to shorter measurement range d_m. This problem is overcome by a variant of correlation Brillouin measurement using peudo-random bit sequence (PRBS) where the sequence length could be set arbitrarily long to increase the measurement range without affecting the spatial resolution [90, 26] (discussed further in the next chapter).

1.7.1 Brillouin optical time domain analysis

Brillouin optical time domain analysis (BOTDA) is the most common time-of-flight Brillouin measurement technique, which can be used to map the resonance spectrum of backward stimulated Brillouin scattering (SBS) along an optical fibre. In the standard scheme, the technique involves using an optical pump pulse to interact with a CW counter-propagating probe light that is red-shifted by intensity modulation to a frequency that is within the variation range of Brillouin frequency shift (BFS) of an optical fibre. By detuning this pump-probe frequency offset around the BFS, the local Lorentzian-shaped Brillouin gain spectrum (BGS) can be reconstructed.

The strength of Brillouin interaction at each position can be determined using small gain approximation. Consider the pump pulse as undepleted inside the fibre, the intensity of Stokes wave within the duration of pump pulse (corresponds to a small length Δz bounded by two points, z_1 and z_2, where $\Delta z = z_2 - z_1$) is derived from the coupled wave equations Eq. 1.111(b). The direction of z is inverted to place the end of fibre $z = L$ as the beginning $z = 0$.

$$\begin{aligned}\int \frac{\mathrm{d}I_s}{I_s}\bigg|_{z_1}^{z_2} &= gI_p \int \mathrm{d}z\bigg|_{z_1}^{z_2} \\ \ln\left(\frac{I_s(z_2)}{I_s(z_1)}\right) &= gI_p\Delta z \\ \ln\left(1+\frac{I_s(z_2)-I_s(z_1)}{I_s(z_1)}\right) &= gI_p\Delta z\end{aligned} \tag{1.121}$$

The left hand side is approximated by Taylor expansion of $\ln(1+x)$ up to the first order. Since the pump is configured such that only one pump pulse is present inside the fibre at a time, the probe light acquires gain only once in the fibre when it crosses the pump pulse. Just before meeting the pump pulse, the intensity of probe light $I_s(z_1)$ is the same as when it enters the fibre $I_s(z_1) = I_s(0)$. After passing the pump pulse, the probe intensity $I_s(z_2)$ remains at the same level of the acquired gain, $I_s(z_2) = I_s(z)$. Thus, Eq. 1.121 becomes

$$\begin{aligned}\frac{I_s(z_2)-I_s(z_1)}{I_s(z_1)} &= gI_p\Delta z \\ G_s(z) = \frac{I_s(z)-I_s(0)}{I_s(0)} &= g(z)I_p\Delta z\end{aligned} \tag{1.122}$$

where $G_s(z)$ is the intensity gain of Stokes signal at position z. I_p and Δz are parameters independent of z.

Consider the entire fibre is from the same spool and placed under homogeneous temperature and strain, $g(z)$ must be a constant along the distance z, $G_s(z)$ is therefore linearly proportional to the intensity of pump pulse I_p at each fibre position. In this case, the full temporal trace of the probe represents the intensity evolution of the propagating pump pulse. This feature of BOTDA is deployed as a local light intensity interrogation technique and has previously been used to monitor 4-wave mixing signals with the aim of obtaining the position-resolved value of chromatic dispersion [77, 85]. This technique is also utilized in recovering the intensity evolution of FSBS (discussed further in chapter 3).

2 Surface and hybrid Brillouin scatterings

The rich dynamics of photon-phonon interactions in subwavelength dimension structures have generated immense scientific interest lately. Surface Brillouin scattering [12] and Brillouin scattering self-cancellation [32] are among the newly discovered optoacoustic dynamics in sub-wavelength optical fibre. Surface Brillouin scattering can be described as an inelastic light scattering generated by a surface acoustic wave (SAW) induced via electrostriction. Traveling at the boundary interface of dissimilar elastic stiffness regions, SAWs demonstrate certain advantages over bulk waves because of their low speed and accessibility, permitting a wide range of applications including surface studies, signal processing, time delay, etc. [87]. The acoustic guidance in microfibre warrants in-depth research, unlike the simple plane-wave description of stimulated Brillouin scattering (SBS) in conventional optical fibres, the low dimension and hard mechanical boundary conditions of silica microfibres confine elastic waves into eigenmodes. This feature gives rise to a variety of acoustic vibrations featuring different spatial distributions and speeds, among them hybrid shear-longitudinal acoustic waves (HAWs) and SAWs [12]. Being compatible with standard optical fibre, silica microfibres simplify the explorations and manipulations of the acoustic waves in an isolated mesoscopic phononics structure [9].

2.1 Acoustic resonances in microfibre

When an intense light from a coherent laser source is launched into an optical fibre, both longitudinal compression and transverse shear waves are electrostrictively stimulated. In the conventional SBS process, a slow travelling longitudinal acoustic wave backscatters the incoming light to a Doppler-shifted frequency, satisfying the phase matching conditions between the interacting lightwaves and acoustic wave, $\nu_B = 2n_{\text{eff}}V/\lambda$, with n_{eff} the effective refractive index of the propagating light, V the acoustic phase velocity and λ the optical wavelength in vacuum. In standard optical fibres, the short wavelength approximation applies well to the longitudinal acoustic waves as the fibre core is large and the transverse strains could be conveniently neglected [52, 11]. However, as the dimension of an optical fibre approaches the acoustic wavelength, the mismatch in the elastic properties between the silica microfibre and air imposes strong boundary conditions, causing longitudinal and shear components of acoustic waves to couple. Thus the acoustic mode branches into several HAWs with different spatial distributions and propagation speeds [12]. Conversely, SAWs originate from the coupling of shear and longitudinal components in an elliptically-polarized particle motion along the boundary of two different materials [12]. SAW generation is efficient due to the large evanescent field extending across the mechanical stress free boundary, shaking the microfibre surface to form minuscule moving periodic corrugations.

The guiding characteristics of the silica microfibres can be expressed based on the analysis of cylindrical waveguide in the previous chapter, where the boundary is assumed to be stress free (T_{rr}, $T_{r\theta}$ and T_{rz} are zero at $r = a$). For the (radial) axisymmetric acoustic modes, the field magnitude and resonance frequencies are obtained from the matrix of simultaneous equations given by the boundary conditions (Eq. 1.80). At the acoustic resonances, the determinant of Eq. 1.80 is zero and the equations are collinear. By using either equation in Eq. 1.80, the amplitudes A and C from Eq. 1.75 can then be related as

$$C = A\frac{-(\lambda(k^2+p^2)+2\mu p^2)J_0(pa)+2\mu\frac{p}{a}J_1(pa)}{2ik\mu\big(qJ_0(qa)+\frac{1}{a}J_1(qa)\big)} \quad \text{or} \tag{2.1a}$$

$$C = A\frac{2ikpJ_1(pa)}{(k^2-q^2)J_1(qa)} \tag{2.1b}$$

The parameters p and q, which are functions of k and ω, are given in Eq. 1.67 and Eq. 1.70, respectively. k and ω are the wave vector and angular frequency at resonance. The relative magnitude of the respective acoustic field components u_r, u_θ and u_z can be retrieved by considering $A = 1$. With the values of A and C, the acoustic field profile can be reconstructed from Eqs. 1.75 and Eqs. 1.76.

The resonance frequency f is related to the axial wave vector k by the dispersion relation of the axisymmetric acoustic modes (Pochhammer-Chree equation, Eq. 1.81). The zeros of this dispersion relation represents the guided modes, which are represented by the solid curves in the dispersion diagram (Fig. 2.1). Phase velocity is given by the slope of the line connecting the related point and the origin whereas group velocity is given by the local gradient at the corresponding point. As a result of the stress free boundary, the compression waves are strongly coupled to the shear waves [8]. All acoustic modes except the first mode L_{01} have cut-off frequencies at $k = 0$. Along the line of free propagating compression wave ($\omega = V_L k$), p vanishes (refer to Eq. 1.67 where $p^2 = \omega^2/V_L^2 - k^2$). Since $p = 0$, $J_0(pr)$ in the expression of the compression wave (Eq. 1.75) is unity ($J_0(0) = 1$), thus the amplitude of the compression wave ϕ is invariant in the transverse plane. From the second equation of Eqs. 2.1, the amplitude of shear wave that is represented by C (Eq. 1.75) is zero when $p = 0$. Thus, the acoustic wave guidance along the compression wave line is determined by the axial propagating scalar plane wave as present in the conventional SBS.

As the velocity of guided acoustic wave is higher than V_L, both p and q are real, the field is thus contributed by both compression and shear waves. In the region where the velocity is

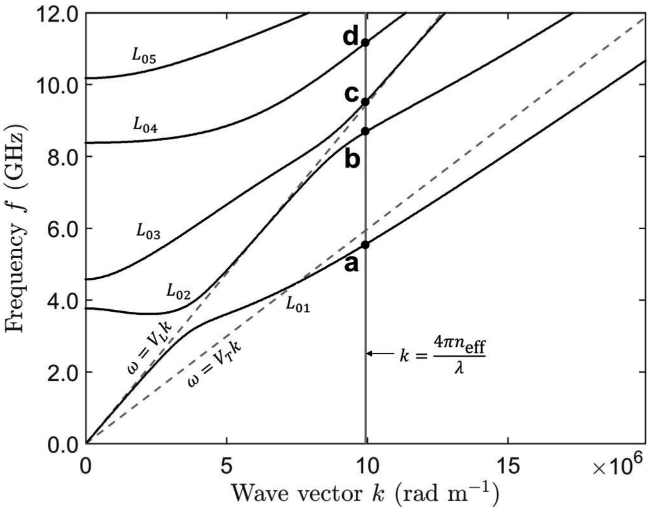

Figure 2.1 – The dispersion diagram of the radially symmetric acoustic waves in a 1 μm-diameter silica microfibre. the gray vertical line in the middle indicates the experimental condition where the wave vector k is positioned at $k = 4\pi n_{\text{eff}}/\lambda$ where the optical wavelength λ is 1.55 μm and the effective refractive index n_{eff} is 1.23.

between compression $\omega = V_L k$ and shear waves $\omega = V_T k$, p is imaginary whereas q is positive real. Given that $J_n(ix) = ((ix)^n/x^n)I_n(x)$ where $I_n(x)$ is the modified Bessel function of the first kind, the field strength of compression wave ϕ in this region decreases rapidly from the fibre boundary. Because of the small ϕ that is present in the middle of the fibre, the acoustic field is dominated by the shear wave. This is evident as in the limit $k \to \infty$, the group velocity of the acoustic modes approaches the shear wave velocity V_T. The fundamental acoustic mode L_{01} has guiding characteristic that is different from the higher order modes, the propagation speed is V_L when k is small. Nevertheless, as k increases, L_{01} transitions into a shear mode and is depressed below the shear wave velocity as k is large. In this case, since both p and q are imaginary, the acoustic field concentrates close to the boundary and decreasing towards the centre, which is similar to the characteristics of Rayleigh wave.

In the experiment, the acoustic waves in microfibre are stimulated by the counter-propagating pump and probe lights at telecom wavelength (λ=1.55 μm). The acoustic wave vector is given by

$$k = 2k_{\text{op}} = \frac{4\pi n_{\text{eff}}}{\lambda} \tag{2.2}$$

The effective refractive index of optical wave for microfibre with radius $a = 0.5\mu$m is $n_{\text{eff}} = 1.23$, which is obtained via semi-analytical solution of the scalar electromagnetic wave equation in optical fibre and consider the fundamental optical mode [4]. Here, the value of acoustic wave vector k calculated based on Eq. 2.2 is 9.94×10^6 rad m^{-1}, also indicated in the dispersion diagram (Fig. 2.1) where it crosses with 4 acoustic modes at **a**, **b**, **c** and **d** which have resonance frequencies at 5.55 GHz, 8.68 GHz, 9.51 GHz and 11.15 GHz, respectively. The mode profiles

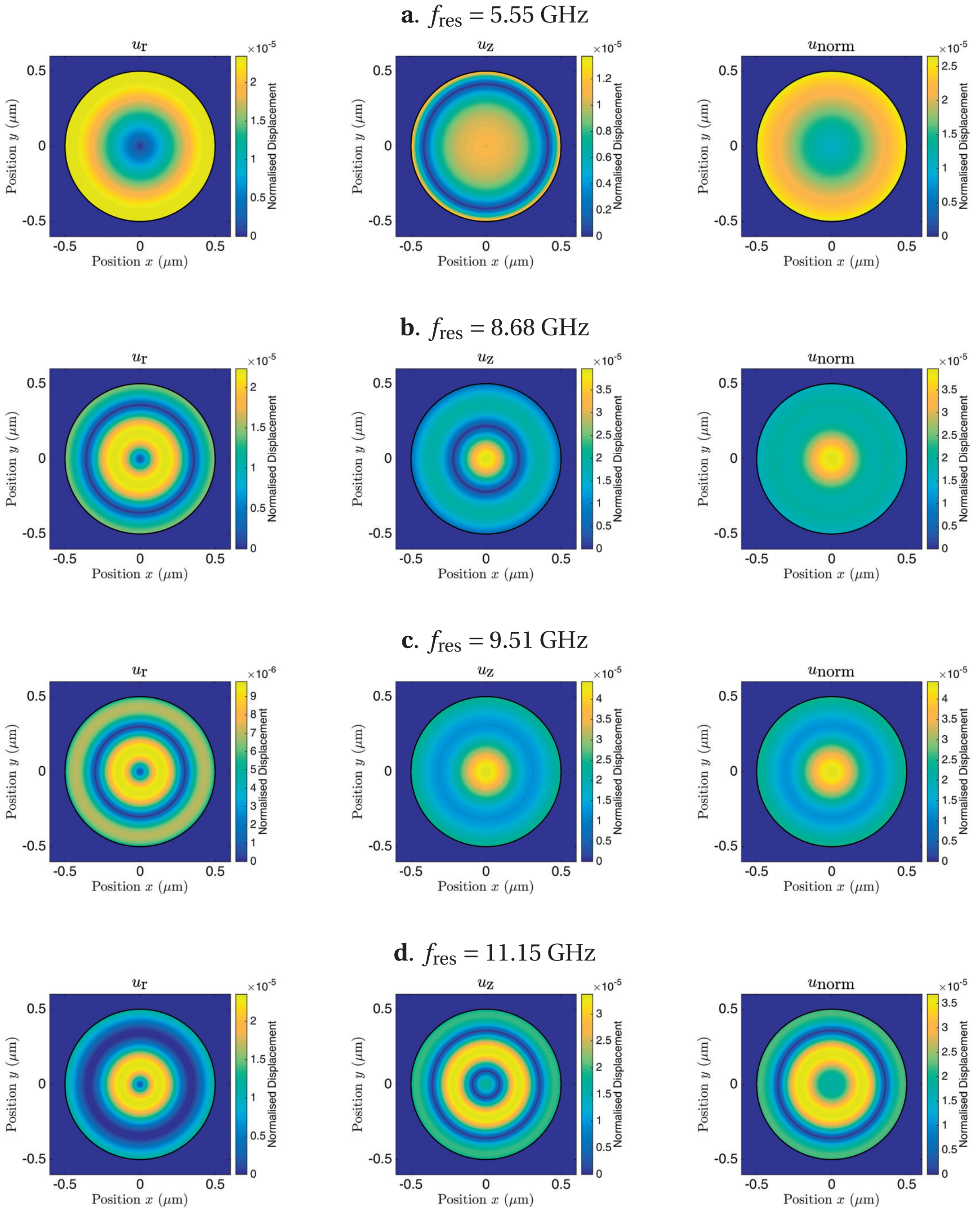

Figure 2.2 – The acoustic displacement profiles of the 1 μm-diameter microfibre at the resonance frequencies f_{res} within 0 and 12 GHz: 5.55 GHz, 8.68 GHz, 9.51 GHz and 11.15 GHz. The lowest resonance mode ($f_{\text{res}} = 5.55$ GHz) is the surface acoustic mode where the acoustic field amplitude decreases rapidly from the microfibre boundary.

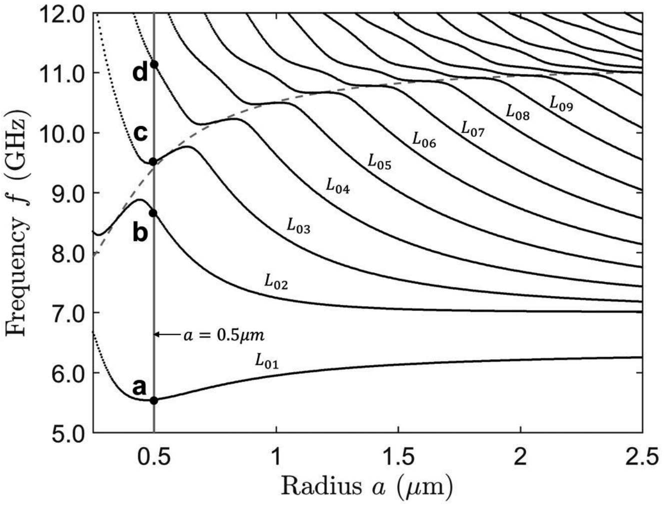

Figure 2.3 – Resonance frequencies of the radial (axisymmetric) acoustic modes as the radius of microfibre varies from 0.25 μm to 2.5 μm. Gray vertical line indicates the microfibre with radius of 0.5 μm.

of each field component given in terms of the material displacements (u_r, u_θ and u_z) and the normalised field ($u_{\text{norm}} = \sqrt{u_r^2 + u_\theta^2 + u_z^2}$) are shown in Fig.2.2, the displacements are normalised by the total displacement integrated over the entire fibre cross-section surface.

Once the displacement field has been determined, strain S_{ij} (Eqs. 1.77), dilatation S (Eq. 1.78) and stress T_{ij} (Eqs. 1.79) can be retrieved accordingly. For the analysis of energy, the kinetic and potential energy of the acoustic modes are given by Eq. 1.25 and Eq. 1.36, respectively. The average kinetic energy per unit cross-sectional area $A = \pi a^2$ is then given by

$$e_{\text{k}}^{(\text{avg})} = \frac{\rho\omega^2}{a^2}\int_R |u_i|^2 \, r\text{d}r \tag{2.3}$$

The integration is performed over the entire cross-sectional surface R. Likewise, the average potential energy per unit cross-sectional area is written as

$$e_{\text{p}}^{(\text{avg})} = \frac{1}{a^2}\int_R T_{ij}S_{ij} \, r\text{d}r \tag{2.4}$$

The average total energy per unit cross-sectional area is then given by the sum of average kinetic and potential energy, given by

$$e_{\text{tot}}^{(\text{avg})} = e_{\text{k}}^{(\text{avg})} + e_{\text{p}}^{(\text{avg})} \tag{2.5}$$

The acoustic resonance frequency changes drastically as the radius of microfibre varies. The resonance frequencies for each microfibre radius are found using the dispersion relation (Eq. 1.81). The acoustic wave vector k is given in Eq. 2.2. For the experiment, λ is fixed at

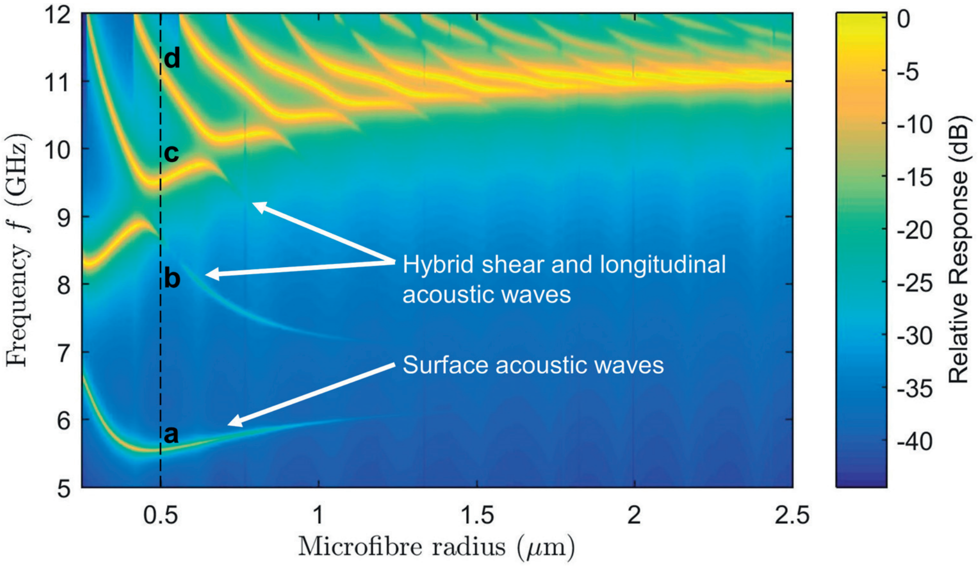

Figure 2.4 – Brillouin spectrum of microfibre by varying the radius obtained through semi-analytical method. The amplitude of spectrum for each radius is normalised by the highest peak and plotted in logarithmic scale.

1.55 μm but n_{eff} varies based on the microfibre radius a, therefore n_{eff} for each a, which is increased in step from $a = 0.25$ μm to $a = 2.5$ μm, is determined through the semi-analytical solution of the scalar electromagnetic equation. The acoustic resonant frequencies of the microfibre with varying radius is shown in Fig. 2.3. The dashed line represents longitudinal compression wave at velocity V_L as in the conventional SBS. Multiple crossovers between shear waves and compression waves are present. The 1 μm-diameter microfibre is marked by the gray vertical line with 4 intersections **a**, **b**, **c** and **d**, they are the same points as in Fig. 2.1.

The relative strength of each acoustic resonance is proportional to the overlap integral between optical and acoustic modes Q_m^2, given in [50]. Since it is arbitrary to set $A = 1$ for the acoustic field in the calculation, Q_m^2 should be normalised for each mode. The normalised Q_m^2 of mode m is written as

$$Q_m^2 = \frac{\left|\int_R E^2(r) \cdot u_z^m(r)\, r\mathrm{d}r\right|^2}{\int_R |E^2(r)|^2\, r\mathrm{d}r\, \int_R |u_z^m(r)|^2\, r\mathrm{d}r} \tag{2.6}$$

where $E(r)$ is the electric field profile. Having the relative peak amplitude, the Brillouin spectra of microfibre for different radii are obtained and plotted in Fig. 2.4. For larger radius, the acoustic modes with frequencies lower than that of the compression wave have small relative peak amplitude as they belong to the shear modes which has negligible contribution towards the scattering of light in the axial direction.

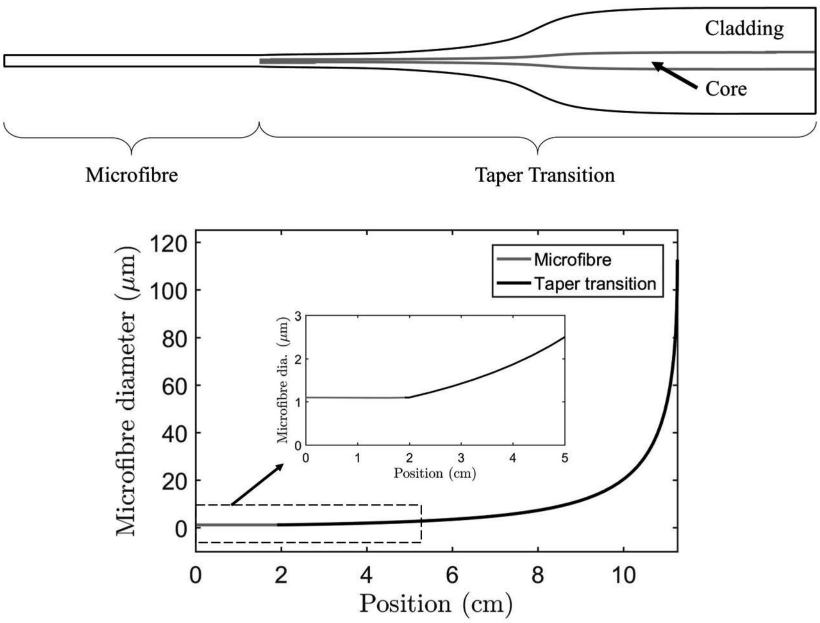

Figure 2.5 – Taper profile including microfibre and the taper transition region. Since the tapered fibre is symmetric, only half of its profile is shown. Position 0 cm is the middle of the tapered optical fibre.

2.2 Tapered optical fibre

Studying the fascinating optoacoustic properties of microfibres would be hard without a low-loss transition between the microfibre and standard optical fibre. The microfibre (produced in FEMTO-ST Institute, France) is fabricated by adiabatically tapering a single-mode fibre (SMF) to micrometer scale using a flame brushing technique [13]. An uncoated stretch of standard SMF is heated in a moving flame and pulled apart slowly by a pair of precision translation stages. The fabricated tapered optical fibre consists of two taper transition regions on both sides, each one has a length of ~10 cm, in the middle is the tapered waist which is referred to as the microfibre, it has a length of ~4 cm and a diameter of ~1.0 µm. The tapered fibre is symmetric, therefore only half of the tapered fibre profile is shown in Fig. 2.5 where the position 0 cm corresponds to the center location of the tapered fibre waist. The optical guidance through the tapered fibre is monitored during fabrication and single mode guidance is ensured by observing the modal beating from the transmitted power.

The presence of distinct elastic waves in the fabricated tapered optical fibre is first verified by launching counter propagating continuous wave (CW) pump and probe light into the microfibre. The probe signal gain is measured by varying the frequency difference between pump and probe lights from 5.4 GHz to 11 GHz. Fig. 2.6 shows the acquired stimulated Brillouin gain spectrum of the tapered optical fibre. SAW, due to its distinct resonance frequency, is clearly identified, nevertheless, the classes of different acoustic resonances from 8.8 GHz to 11 GHz are indistinguishable without resolving to their respective location in the microfibre.

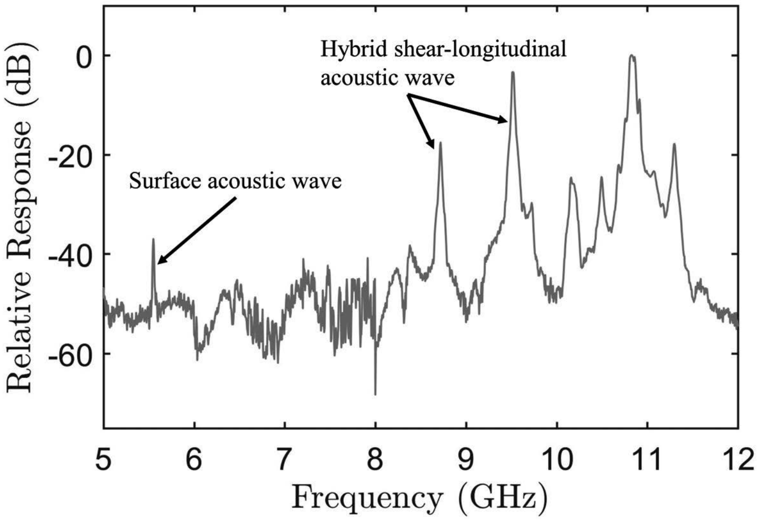

Figure 2.6 – Integrated stimulated Brillouin scattering gain spectrum measured using counter propagating pump and probe lights. The surface and hybrid acoustic modes associated to the microfibre section are clearly visible. Different acoustic modes are observed from 10-12 GHz as a result of the diameter variation along the taper transition region.

2.3 Distributed analysis of surface and hybrid acoustic waves

The existence of multiple auxiliary elastic resonances in a silica microfibre have been experimentally verified through the heterodyne detection technique [12]. However, such measurements merely indicate the existence of multiple elastic resonances in the entire tapered fibre sample, applied techniques so far did not resolve the exact longitudinal location of each resonance mode inside a tapered fibre. Indeed, the existence of each acoustic mode highly depends on the local diameter of the microfibre, and therefore different resonance frequencies are expected to be found at different positions of the tapered fibre section (e.g. in the transition region and waist). Distributed Brillouin measurement techniques can be used to stimulate and probe different classes of acoustic waves at specific locations inside an optical microfibre, thus pinpointing precisely their respective locations and amplitude. Specifically, using the correlation-based distributed Brillouin technique [44, 90, 26], each Brillouin resonance frequency can be locally generated at any position over the tapered optical fibre with a spatial resolution of a few centimeters [20].

The distributed Brillouin measurement technique utilised here to position-resolve the Brillouin scatterings in the tapered optical fibre is referred to as phase-correlation distributed Brillouin measurement [90, 26]. This technique involves launching counter-propagating pump and probe light beams that are phase-modulated with the same 0 or π phase shift random binary bit sequence. Therefore at certain locations inside the tapered fibre, the optical phase of both pump and probe are identical, these locations are referred to as correlation peaks. At the correlation peak, the local acoustic waves (independently for each acoustic mode) have enough time to be efficiently activated, thus scattering pump light at the corresponding Brillouin resonant frequency. This way, the phase-modulated Brillouin interaction technique can be used to simultaneously generate and measure different acoustic waves, including SAWs, with precise location mapping inside microfibres. Experimental results are validated comparing them with the semi-analytical analysis described in the previous section. The experimental approach here combined with the theoretical analysis presented, provide a way to better understand the physical behaviours of guided acoustic waves with changing structural dimensions.

2.3.1 Theory of phase-correlation distributed Brillouin measurement

In phase-correlation distributed Brillouin measurement [90, 26], two counter-propagating light waves that are modulated with 0 and π phase pseudo random binary sequence (PRBS) are used to stimulate acoustic waves at their cross-correlation points. The concept is illustrated in Fig. 2.7. The counter propagating light waves are defined as

$$E_p = A_p \exp(i(\omega_p t - k_p z + \phi_p)) + \text{c.c.} \tag{2.7a}$$

$$E_s = A_s \exp(i(\omega_s t + k_s z + \phi_s)) + \text{c.c.} \tag{2.7b}$$

As they interfere in the fibre, the resulting optical field intensity is

$$I = 2n\epsilon_0 c E_p E_s^* = 2n\epsilon_0 c A_p A_s^* \exp(i(\Omega t - qz + \Delta\phi)) \tag{2.8}$$

where the difference of frequency, wave vector and phase are $\Omega = \omega_p - \omega_s$, $q \approx 2k_p$ and $\Delta\phi = \phi_p - \phi_s$, respectively. The pseudo random bit train is defined as

$$B_{\text{PRBS}}(t) = \sum_{j=0}^{\infty} \sum_{i=0}^{N} X_i \; [u(t - i(j+1)T_{\text{bit}}) - u(t-(i+1)(j+1)T_{\text{bit}})] \tag{2.9}$$

where X_i is the PRBS of length N, $u(t)$ is the unit step function and T_{bit} is the bit duration, the PRBS repeats itself after every N bits and j is the repetition count of the PRBS pattern. Since pump and probe lights are counter-propagating inside the fibre, the phase difference is

$$\begin{aligned} \Delta\phi = \phi_p - \phi_s &= \pi \left(B_{\text{PRBS}}(t'_p) - B_{\text{PRBS}}(t'_s) \right) \\ &= \pi \left(B_{\text{PRBS}}(t - \frac{z}{c/n_{\text{g}}}) - B_{\text{PRBS}}(t - \frac{L-z}{c/n_{\text{g}}}) \right) \end{aligned} \tag{2.10}$$

where t'_p and t'_s are the position-dependent transformed time of pump and probe wave, respectively. z is the position from the starting point of the fibre, c is the speed of light in vacuum, n_{g} is the effective group index of the guided light and L is the length of fibre. At the correlation peaks, for example $z = L/2$, the phase difference $\Delta\phi$ is zero, the optical intensity is therefore at its maximum. However, elsewhere in the fibre, $\Delta\phi$ alternates between 0 and π randomly, as a result the optical intensity averages to zero in time. Since the acoustic wave

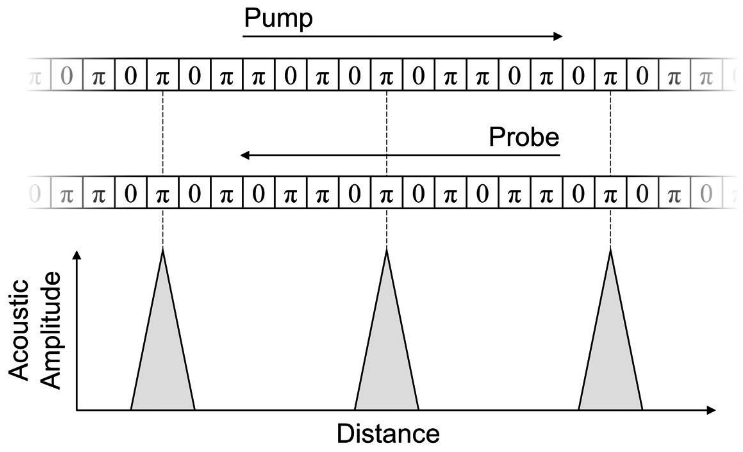
Pump
π 0 π 0 π 0 π π 0 π 0 π 0 π π 0 π 0 π 0 π π
Probe
0 π π 0 π 0 π 0 π π 0 π 0 π 0 π π 0 π 0 π 0
Acoustic Amplitude
Distance

Figure 2.7 – Illustration of phase-correlation based distributed Brillouin measurement with 7-bit Pseudo Random Binary Sequence (PRBS).

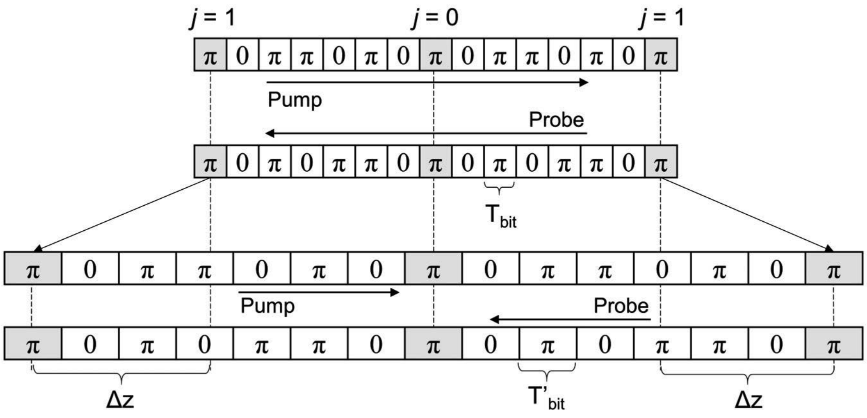
j = 1
j = 0
j = 1
π 0 π π 0 π 0 π 0 π π 0 π 0 π
Pump
Probe
π 0 π 0 π π 0 π 0 π 0 π π 0 π
T_bit
π 0 π π 0 π 0 π 0 π π 0 π 0 π
Pump
Probe
π 0 π 0 π π 0 π 0 π 0 π π 0 π
Δz
T'_bit
Δz

Figure 2.8 – The position of the first order correlation peak is displaced by Δz through varying the duration of PRBS bit T_{bit}.

requires a certain activation time to reach its full amplitude, the rapid 0 and π phase shifts of light intensity renders the acoustic wave generation ineffective.

In practice, there are two ways to place the correlation peak in the fibre. The first method is by introducing a time delay in either pump or probe wave. However, this requires an adjustable optical delay line. The second method is displacing the sample fibre to a higher order correlation peak by including a long delay fibre. Through changing the duration of PRBS bit T_{bit}, the position of a higher order correlation ($j > 0$) can be controlled, as illustrated in Fig. 2.8. As the PRBS bit length is controlled by a frequency generator in the experiment, the frequency of T_{bit} is given as $f_{\text{PRBS}} = 1/T_{\text{bit}}$. For the change of T_{bit}, assuming the frequency change is small, the change of bit duration is given as

$$\Delta T_{\text{bit}} = \frac{1}{f^{(1)}_{\text{PRBS}}} - \frac{1}{f^{(2)}_{\text{PRBS}}} = \frac{\Delta f_{\text{PRBS}}}{f^{2}_{\text{PRBS}}} \tag{2.11}$$

From Eq. 2.10, the time difference between the pump and probe waves is

$$\begin{aligned}\Delta t_{\text{ps}} &= t'_p - t'_s \\ &= \frac{L-2z}{c/n_{\text{g}}}\end{aligned} \tag{2.12}$$

The repetition time of the PRBS pattern is

$$\Delta t_{\text{rep}} = mNT_{\text{bit}} \tag{2.13}$$

where m is the order of correlation peak and N is the length of PRBS sequence. At the correlation peaks, $\Delta t_{\text{ps}} = \Delta t_{\text{rep}}$. Therefore the location of a correlation peak is given by

$$z = \frac{1}{2}\left(L \pm mNT_{\text{bit}}(c/n_{\text{g}})\right) \tag{2.14}$$

Introducing a small change in the bit duration ΔT_{bit}, the position of correlation peak will be moved by

$$\Delta z = \pm\frac{1}{2}mN\Delta T_{\text{bit}}(c/n_{\text{g}}) \tag{2.15}$$

The displacement of correlation peak Δz scales with its order m and PRBS length N. In practice, a long fibre (delay line) of length L with a different Brillouin frequency shift is connected with the sample with length l much smaller than L, $l \ll L$, so that a higher order correlation peak falls inside the sample. By substituting $z = L$ into Eq 2.13, the order of correlation peak that lies just outside the long fibre is given by

$$m = \lceil \frac{L}{NT_{\text{bit}}c/n_{\text{g}}} \rceil \tag{2.16}$$

Then, substitute Eq. 2.16 into Eq. 2.15, the sampling interval (change of the correlation peak's position) is obtained as

$$\Delta z = \frac{1}{2}L\frac{\Delta T_{\text{bit}}}{T_{\text{bit}}} = \frac{1}{2}L\frac{\Delta f_{\text{PRBS}}}{f_{\text{PRBS}}} \tag{2.17}$$

2.3.2 Spatial resolution

The spatial resolution of the phase-correlated Brillouin measurement is determined by two factors: the correlation peak size and the sampling interval. Consider the counter-propagating lights centered at the correlation peak, the transformed time of the pump and probe waves

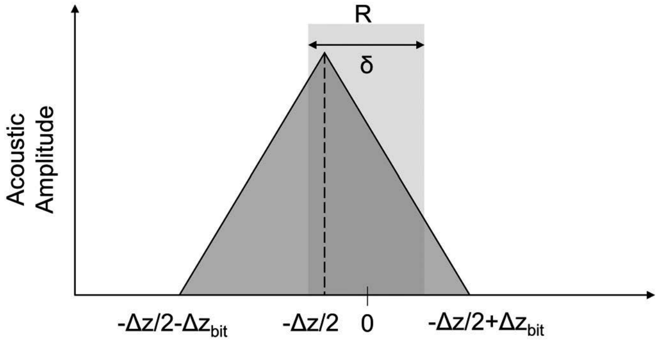

Figure 2.9 – The gain response calculated from the convolution of a triangular correlation peak and the rectangular region R with length δ.

are $t'_p = t - z/(c/n_g)$ and $t'_s = t + z/(c/n_g)$, respectively. As the time difference equals to the duration of a PRBS bit, $T_{\text{bit}} = t'_s - t'_p$, the length that corresponds to the overlapping of a PRBS bit is given as

$$\Delta z_{\text{bit}} = \frac{1}{2} T_{\text{bit}}(c/n_g) \tag{2.18}$$

Assuming perfect 0 and π phase transitions for the light waves, the acoustic wave amplitude at the correlation peak can be defined as the convolution of two rectangular pulses, which results in a triangular shape with base length that is twice the PRBS bit length Δz_{bit}. Here, Δz_{bit} is defined as the full width half maximum (FWHM) of the correlation peak.

In order to detect a zone R with length δ, the sampling interval Δz has to be configured judiciously. Δz that is much larger than δ will fail to detect R. The acoustic response limited by R is determined from the convolution of the correlation peak and R, as illustrated in Fig. 2.9. The shape of the correlation peak with integral equal to unity is given by

$$c(z) = \frac{1}{\Delta z_{\text{bit}}} \left(1 - \left|\frac{z + \Delta z/2}{\Delta z_{\text{bit}}}\right|\right) \tag{2.19}$$

Consider the threshold of detectable R is half of the maximum gain, the following integral from the convolution is written

$$\int_{-\delta/2}^{\delta/2} \frac{1}{\Delta z_{\text{bit}}} \left(1 - \left|\frac{z + \Delta z/2}{\Delta z_{\text{bit}}}\right|\right) dz = \frac{1}{2} \tag{2.20}$$

Since the area of triangle inside R is $1/2$, the area outside R must be equal to $1/2$. The integral can then be solved by using triangle similarity, leading to the following equation

$$\frac{1}{2\Delta z_{\text{bit}}^2} \left((\Delta z_{\text{bit}} - \delta/2 - \Delta z/2)^2 + (\Delta z_{\text{bit}} - \delta/2 + \Delta z/2)^2\right) = \frac{1}{2} \tag{2.21}$$

Equation 2.21 is solved for Δz, which gives

$$\Delta z = \sqrt{-2\Delta z_{\text{bit}}^2 + 4\Delta z_{\text{bit}}\delta - \delta^2} \tag{2.22}$$

Δz obtained here represents the minimum sampling interval needed to detect R of length δ with sampling resolution of Δz_{bit}. Consider the finest possible sampling interval $\Delta z = 0$, δ is then obtained as

$$\delta = 2\Delta z_{\text{bit}}\left(1 - 1/\sqrt{2}\right) \approx 0.6\ \Delta z_{\text{bit}} \tag{2.23}$$

Thus, by oversampling with sampling interval far smaller than the correlation peak FWHM, the spatial resolution could be reduced to 60% of the correlation peak's FWHM.

2.3.3 Experimental setup

Figure. 2.10 shows the experimental setup for measuring the local Brillouin gain along the microfibre, using counter propagating pump and probe waves. The incoming light from a laser diode (1552 nm) is first phase-modulated by a 1023-bit PRBS at ~2 GHz clock frequency. The phase-modulated light is then split by a 90/10 coupler into pump and probe arms. Light in the probe arm is intensity-modulated to generate sidebands with suppressed carrier and passed through a 2 km SMF delay line, which is necessary to place a high-order correlation peak inside the microfibre and thus to provide precise longitudinal sampling interval. The Brillouin frequency scanning step is 1 MHz.

In order to distinguish the correlation peak and create strong acoustic wave simultaneously, the phase-modulated light in the pump arm is time-gated (intensity-modulated) by a semiconductor optical amplifier (SOA) using pulses of 70 ns with 25 µs repetition period and then amplified by an erbium-doped fibre amplifier (EDFA). This way, each correlation peak with its amplitude would appear separately in the Brillouin back-scattered time trace. After pump and probe interact inside the sample, the probe is directed into a detection system, where one of the sidebands is selected by a fibre Bragg grating (FBG) ($\Delta\nu$ = 6 GHz) and detected by a photo-receiver ($\Delta\nu$ = 125 MHz). The detailed operating principles of phase-correlation distributed Brillouin scanning method can be found in [90, 26].

The spatial resolution is optimized to give sufficient detected Brillouin gain with reasonable number of resolved points. The PRBS clock period T_{bit} determines the correlation peak's FWHM, which is evaluated to be ~5.2 cm, assuming an effective refractive index n_{eff} of 1.44 for silica glass. The longitudinal sampling interval is set to 2.5 cm. So with the pre-set oversampling the spatial resolution can be as small as 60 % of the correlation peak FWHM, giving an effective spatial resolution of 3.2 cm. The longitudinal scan is then conducted over 40 cm in total length, covering the waist, transition and untapered fibre sections.

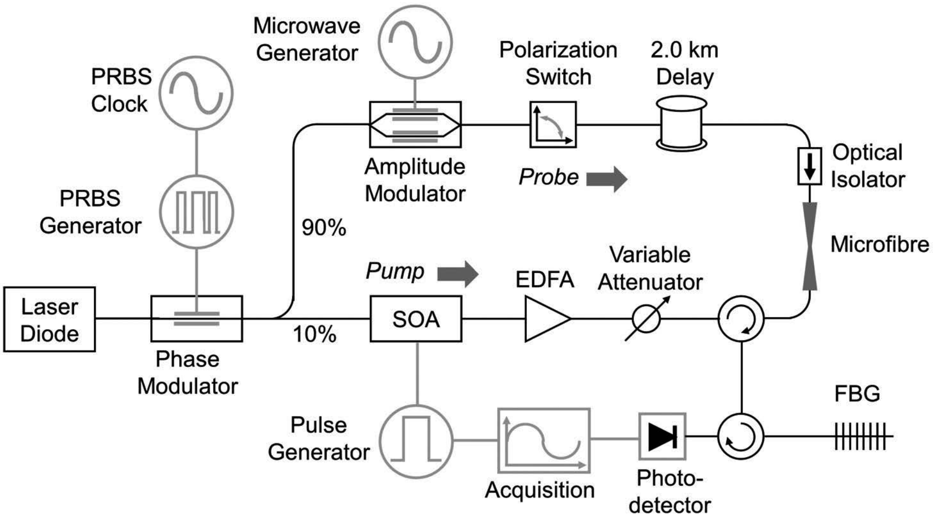
Microwave Generator
PRBS Clock
Polarization Switch
2.0 km Delay
Optical Isolator
Amplitude Modulator
Probe
PRBS Generator
90%
Microfibre
Variable Attenuator
Pump
EDFA
Laser Diode
SOA
10%
Phase Modulator
FBG
Pulse Generator
Acquisition
Photo-detector

Figure 2.10 – Experimental setup used for phase correlation-based distributed Brillouin measurements. The components are labelled as follows: EDFA, erbium-doped fibre amplifier; SOA, semiconductor optical amplifier; FBG, fibre Bragg grating. PRBS, pseudo random binary sequence.

2.3.4 Distributed Brillouin spectrum of microfibre

The spatio-spectral domain of the microfibre is scanned by independently sweeping the pump-probe frequency offset and varying slightly the PRBS clock frequency f_{PRBS}. The small changes in the PRBS clock allow for a full longitudinal scan of the entire tapered fibre, having practically a negligible impact on the spatial resolution due to the use of a high-order correlation peak [90, 26]. The Brillouin gain spectra (and respective resonance frequencies) are experimentally obtained along the microfibre by scanning a frequency range from 5.5 GHz to 11.5 GHz, as shown in Fig. 2.11. The distance scale in the figure originates in the middle of the waist and increases towards the untapered regions. The Brillouin frequency shift of the untapered standard fibre segments is around 10.815 GHz, as shown in Fig. 2.11(e) at positions larger than ±12 cm. Results indicate that 4 acoustic resonances can be clearly identified in the waist (microfibre), i.e. around 0 cm: at 5.6 GHz (Fig. 2.11(a)), 8.8 GHz (Fig. 2.11(b)), 9.65 GHz (Fig. 2.11(c)) and 11.45 GHz (Fig. 2.11(f)). From these, the resonance at 9.65 GHz gives the highest gain (see the high contrast in Fig. 2.11(c)), followed by 11.45 GHz and 8.8 GHz.

In the transition region (distance from 2 cm to 8 cm), a number of resonance pairs are found at 10.25 GHz, 10.55 GHz, 10.7 GHz and 10.815 GHz (see Fig. 2.11(d),(e)), indicating the symmetry of the tapered fibre sample and confirming the structural nature of the acoustic resonances. In the far transition region (distance from 8 cm to 12 cm, i.e. when the taper diameter approaches the standard fibre diameter), an unusual broad scattering band appears from 10.85 to 11.2 GHz (Fig. 2.11(e)) due to the changes of longitudinal and shear acoustic velocities as the fibre diameter varies. The broad scattering band discontinued from the resonant frequency of standard optical fibre segment (at 10.815 GHz). This can be explained

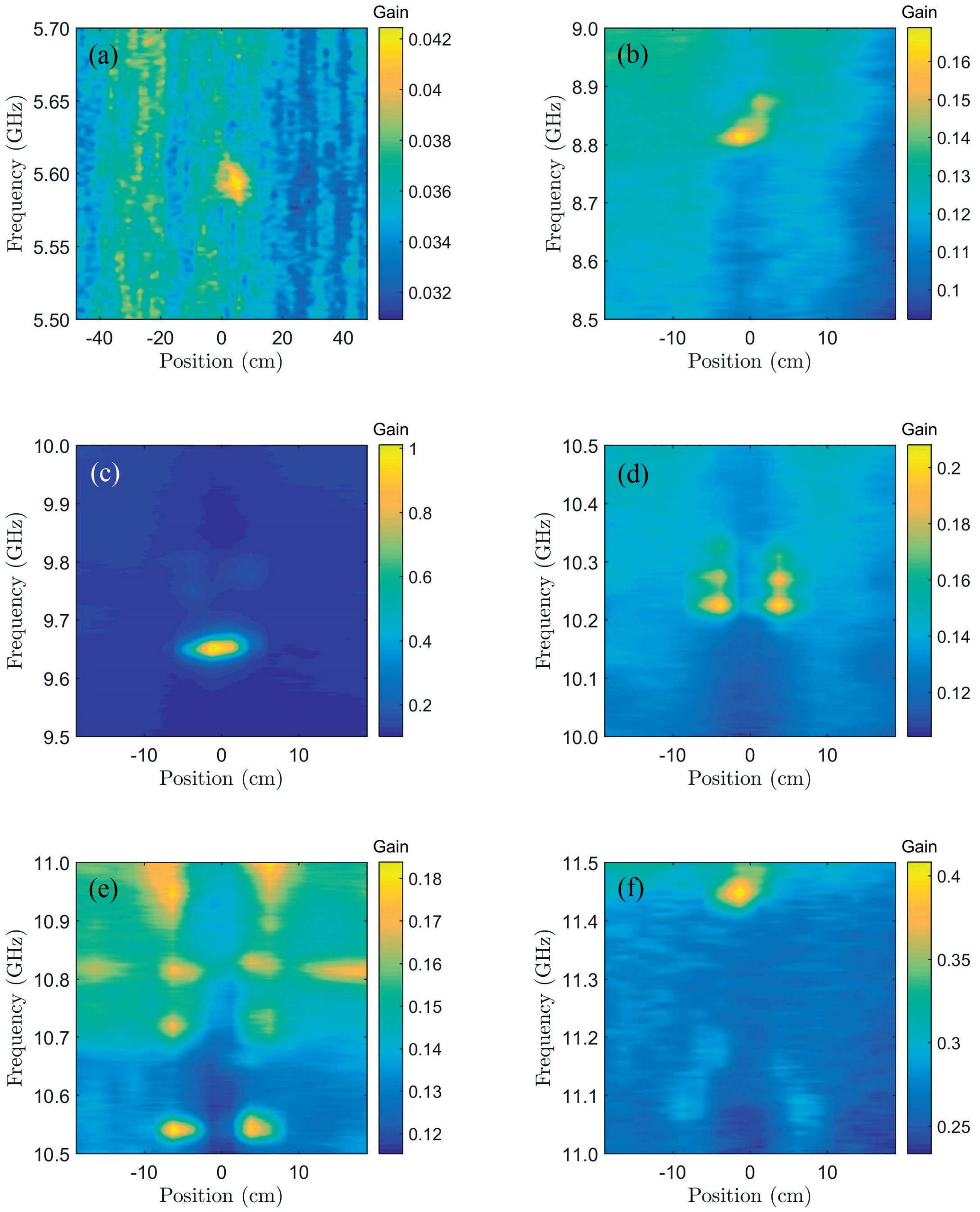

Figure 2.11 – Phase-correlated distributed Brillouin gain spectra along the silica microfibre for frequency ranges: (a) 5.5 – 5.7 GHz, (b) 8.5 – 9.0 GHz, (c) 9.5 – 10.0 GHz, (d) 10.0 – 10.5 GHz, (e) 10.5 – 11.0 GHz and (f) 11.0 – 11.5 GHz. Position 0 cm is the center of the tapered waist. Gain scales are linear, calculated with respect to the detected off-resonance signal level in each scanning region. Note that the horizontal scale of (a) is made narrower to visualize the entire scanning result that has larger spatial resolution.

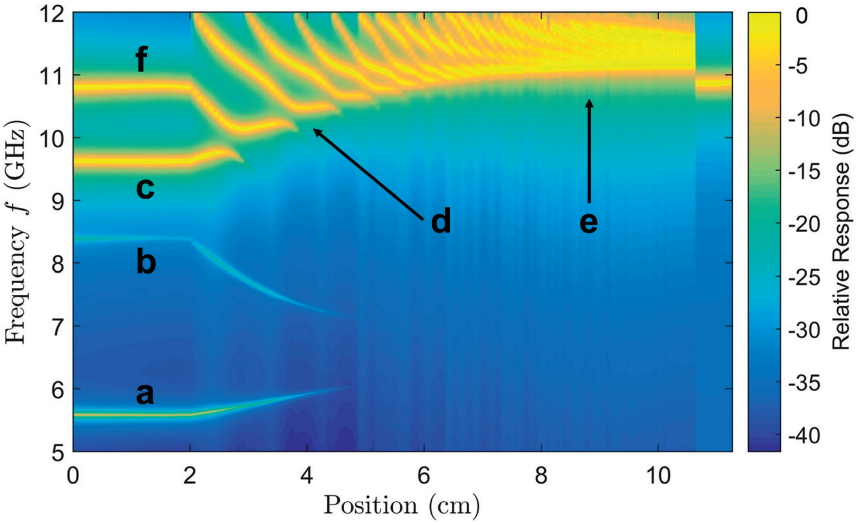

Figure 2.12 – Brillouin spectrum as a function of tapered fibre position. Labels (a) to (f) indicate the corresponding acoustic modes measured in Fig. 4(a)-(f)

by the rapid diameter reduction and core disappearance in the transition region: as fibre tapers down exponentially to micrometer scale, the Ge-doped core defuses rapidly, forcing the light to propagate in the pure silica cladding and causing the sudden jump in the Brillouin frequency shift.

SAW is the slowest propagating acoustic wave in the microfibre, thus leading to the lowest resonant frequency, being of ~5.6 GHz (Fig. 2.11(a)). Due to the strong pump reflection induced by the taper profile and the close spectral proximity between SAW and pump frequencies, the measurement of SAW has been performed with an enlarged spatial resolution (~85 % longer). Indeed, since the pump and probe spectra broaden with finer spatial resolution (i.e. with large PRBS clock frequencies), sharper spatial resolutions typically lead to overlapping of the phase-modulated pump and probe spectra. This induces real practical challenges in the optical filtering required in reception, especially for the low SAW resonance frequency of 5.6 GHz. To minimize this spectral overlapping, and reduce distortions in the measurements, the PRBS clock frequency for SAW measurement has been reduced down to 1.0 GHz, resulting in a correlation peak FWHM of 10 cm. With oversampling, the spatial resolution could be improved down to about 6 cm, covering the uniform microfibre region in a single sampled point. The measurements in Fig. 2.11(a) indicate that the phase-correlation Brillouin method used in this case allows for distributed Brillouin measurements of SAW.

Nevertheless, a few solutions to overcome the limit on spatial resolution due to spectral overlapping exist in literature. A noise-based correlation technique [23] has been shown to spatially resolve the Brillouin response of a chalcogenide photonic waveguide on a chip with a high spatial resolution of 800 μm [91]. In another approach, low frequency intensity modulations are introduced to the pump and probe lights and the Brillouin response is detected via lock-in technique, a spatial resolution of 1.6 mm was achieved [76].

The experimental results are confirmed by semi-analytical solutions as shown in Fig. 2.12. Brillouin spectrum is simulated by varying the wire diameter according to the tapering profile. As indicated in labels (a), (b), (c) and (f), all the acoustic resonant frequencies at the taper waist (microfibre) agree with the measurements. The resonance peaks are slightly shifted due to the perturbation in strain during microfibre packaging, temperature variation or slight departure from the intended microfibre diameter during fabrication. In the transition region, acoustic resonance branching appears at shear and longitudinal wave intersections that form multiple avoided crossings. Since the Brillouin gain is spatially integrated over the correlation peak width in the experiment, the tails extending out from most resonant peaks are not clearly visible with the exception of the fleeting extensions for resonances at 8.8 GHz (Fig. 2.11(b)) and 9.65 GHz (Fig. 2.11(c)). Higher up in the tapered fibre dimension, acoustic mode splitting is vague, yet the superposition of the adjoining resonances gives rise to a broad scattering band (label (e)) as noticed in the experiment (Fig. 2.11(e)) which expands gradually as the taper diameter approaching the micrometer scale. For the far taper position, light is guided in the Ge-doped fibre core, which has slightly lower Brillouin frequency shift (~10.8 GHz at $\lambda = 1.55\ \mu$m) as compared to the pure silica fibre cladding (~11.1 GHz at $\lambda = 1.55\ \mu$m). As the core size reduces to certain diameter that corresponds to the position at ~10.5 cm, the propagation constants of guided light in both the core and the cladding become almost equal. This allows the guided light to couple abruptly into the fibre cladding, therefore the properties of Brillouin scattering in this case are calculated based on the properties of cladding material (pure silica). On the other hand, radiation pressure has previously been observed to cancel Brillouin scattering in a subwavelength tapered optical fibre [32]. However, this phenomenon is not observed in the current experiment using counter-propagating pump and probe lights, therefore the effect of radiation pressure is not considered in this theoretical model. This issue is further discussed in the concluding chapter.

2.3.5 Discussion

The generation and detection of localized SAWs and different classes of hybrid acoustic waves along a microwire have been demonstrated using a phase-correlation based distributed Brillouin interrogation method. Experimental results reveal the diverse acoustic spatio-spectral dynamics inside a microscale structurally-varied optical waveguide, presenting a convenient way to study the physics of local SAWs, HAWs, shear wave propagation, coupling regimes at avoided crossing, etc. The study reveals the interest of an intermediate region where the fibre diameter is in the range 5-10 μm, for which the acoustic resonances vary stepwise and not continuously. The successful demonstration of SAWs distributed Brillouin mapping opens a way to practically realize distributed SAWs sensors in optical fibres. In general, this technique also provides huge potentials for acoustic engineering in subwavelength waveguide given the ability to access acoustic properties at arbitrary points, thus effectively turning a continuous optical fibre into a multi-element acoustic device or sensor. Further developments are aiming at understanding the interactions between different acoustic waves and the surrounding environment.

3 Forward stimulated Brillouin scattering

Forward stimulated Brillouin scattering (FSBS), also known as guided acoustic waves Brillouin scattering (GAWBS), is an opto-acoustic effect involving interaction of light with transverse acoustic eigenmodes in an optical waveguide, which can be stimulated through electrostriction. The nomenclature GAWBS is coined by R. M. Shelby *et al.* who first studied this effect in optical fibre [72]. Nevertheless, the term FSBS will be referred to in the text to underscore the similar physics of elasticity as in the conventional backward Brillouin scattering while highlighting the feature of forward light scattering. The presence of FSBS is apparent in optical fibres because of the acoustic waves confinement in the tranverse direction, which does not happen for acoustic wave propagation in bulk material. The scattering properties of FSBS are described well by the clasical elastic wave propagation presented in the first chapter. Though intriguing, the underlying acoustic analyses of FSBS in optical fibre are similar to the elastic properties of cylindrical pipes and rods that has long been investigated in numerous previous works purely related to acoustic study [75, 30]. Initially, FSBS was mainly treated as a source of perturbation that limits long-range soliton transmission and generation of optical squeezed states in an optical fibre [53, 64]. The intense pulses used in the soliton optical transmission electrostrictively excite transverse acoustic waves and give rise to spatio-temporal changes in the refractive index of the fibre material, distorting the light pulses that arrive afterwards. The temporal dynamics of FSBS and its interaction with optical soliton propagation was studied and discussed extensively in [29, 14].

As photonic crystal fibre (PCF) was introduced and the technique of tapering optical fibre has been improved in great extend, studying FSBS in a long sub-wavelength structure is made possible. Due to the tight confinement of optical and acoustic fields in such tiny waveguide, the overlap between the two fields is large, which gives rise to strong FSBS response [46, 25, 47]. As smaller fibre dimension indicates shorter round-trip time for the acoustic wave resonating within the fibre cross-section, the frequency separation between the resonance peaks becomes larger and could reach multi-gigahertz resonance frequency for the fundamental acoustic mode in a typical solid core PCF with 1.8 μm core diameter [46]. Besides, FSBS is widely studied in silicon based sub-wavelength waveguide as tailorable narrow linewidth light source [60, 84, 73], paving way for monolithic integration with existing silicon photonic technology. Beyond continuous wave laser, FSBS based mode-locked fibre laser has been demonstrated using a 2.5 m PCF. Combining a proper cavity design and a optically dispersive guiding structure, the periodical acoustic oscillations perturbs the intensity of guided light and produces picosecond duration pulses [61, 40]. Interestingly, FSBS is also observed in air-filled hollow core PCF [68]. As both optical and acoustic waves are guided in the air, FSBS can be aptly turned into gas spectroscopy. Regardless of the myriads of FSBS studies in different waveguides, FSBS in standard optical fibre (SMF) remains compelling owing to the radially symmetric structure that simplifies the exploration of novel applications.

3.1 Transverse acoustic resonances

The acoustic modes present in the forward light scattering are the radial modes and the mixed torsional-radial modes, which define the acoustic waves that propagate radially and circumferentially, respectively. The guiding characteristics of radial (axisymmetric) transverse acoustic mode is described by Pochhammer-Chree equation (Eq. 1.81). As the axial wave vector approaches zero, the equation is given by

$$\frac{2p}{a} J_1\left(pa\right) - q^2 J_0\left(pa\right) = 0 \tag{3.1}$$

The absence of $J_n(qa)$ terms implies that the acoustic resonances are dominated by the compression wave. Using the Bessel recurrence identity,

$$J_n(x) = \frac{x}{2n}\left(J_{n-1}(x) + J_{n+1}(x)\right) \tag{3.2}$$

Equation 3.1 can be rewritten to yield the familiar characteristic equation

$$(1-\alpha^2)J_0(y) - \alpha^2 J_2(y) = 0 \tag{3.3}$$

where α is the ratio of the transverse acoustic velocity V_T to the longitudinal acoustic velocity V_L, $\alpha = V_\mathrm{T}/V_\mathrm{L}$. From the solutions y_m of Eq. 3.3, the eigenfrequencies f_m of the m modes are given by

$$f_m = y_m \frac{V_\mathrm{L}}{2\pi a} \tag{3.4}$$

where a is the optical fibre radius. The dispersion diagram of radial transverse acoustic mode, as shown in Fig. 3.1, is plotted based on Eq. 3.1 with the radius a of standard single-mode fibre (SMF), $a = 62.5\ \mu m$. The transverse acoustic modes enter their respective cut-off frequencies at zero wave vector. For very small wave vector $k < 50$, the slope of dispersion curve is close to zero, which indicates negligible group velocity and very dispersive acoustic guidance. The resonance frequencies of transverse acoustic waves for SMF are calculated and listed in Table 3.1 alongside with the experimentally measured values.

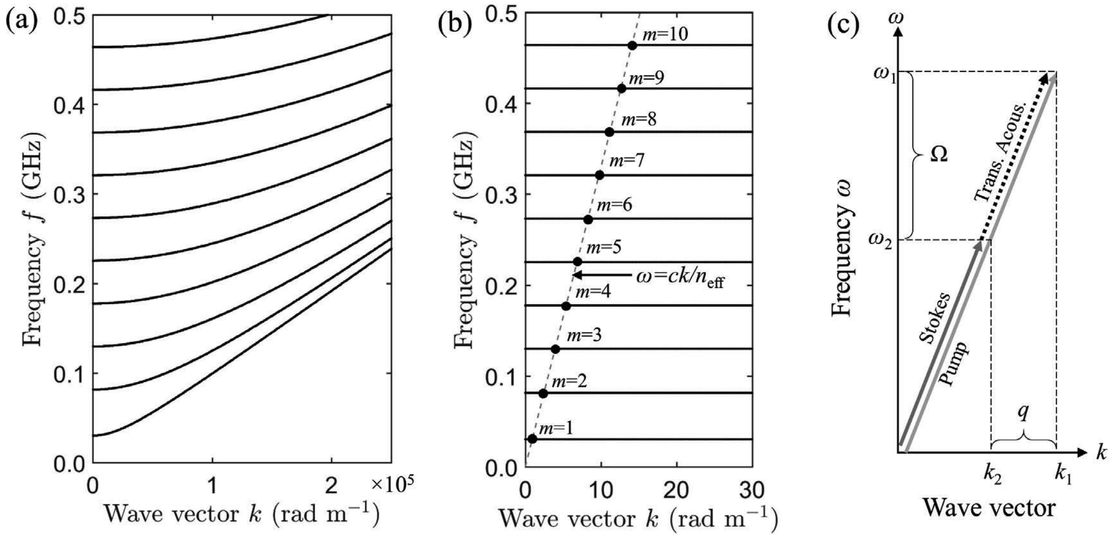

Figure 3.1 – (a) Dispersion diagram of radial transverse acoustic waves. (b) Zoom-in of dispersion diagram for small axial wave vector where the group velocity is negligible. (c) The phase matching between the vectors of the pump, Stokes lights and the stimulated transverse acoustic mode, which is given by the crossing points of acoustic modes and light line (dotted line) in (b).

3.2 Optical stimulation

Via FSBS, two coherent light waves of frequencies ω_1 and ω_2, respectively, are coupled with the transverse acoustic resonance of frequency $\Omega = \Delta\omega = \omega_1 - \omega_2$. Momentum conservation requires that the acoustic and optical wave vectors $q(\Omega)$ and $k(\omega)$, respectively, satisfy the phase matching relation, $q(\Omega) = \Delta k = k(\omega_1) - k(\omega_2)$. In the case of forward light scatterings, the group velocity of the activating light v_{g} is equivalent to the axial phase velocity of the transverse acoustic wave V_{a}, $v_{\mathrm{g}} = \Delta\omega/\Delta|k| = \Omega/q = V_a$ (see Fig. 3.1(c)). Due to the negligible group velocities of the transverse acoustic eigenmodes for small axial wave vectors, the same acoustic resonant frequencies maintain for a broad range of axial phase velocities, thus relaxing the phase matching condition and allowing the transverse acoustic wave to be stimulated by light at any wavelength.

The mode profile of transverse acoustic wave can be obtained using the same approach as in section 2.1. The normalised displacement u_{norm} of the 5th, 7th and 9th modes are shown in Fig. 3.3. When $k \to 0$, from Eq. 1.75 and the second equation of Eq. 2.1, the components of the shear wave are small, which indicates the mode profile of transverse acoustic resonance is dominated by the compression wave. The relative peak amplitude of the resonances are determined from the overlap factor Q^2 of acoustic and optical mode. Q^2 of FSBS is different from the backward SBS, the derivation of FSBS overlap integral is shown in Appendix C.

$$Q_m^2 = \frac{\left|\int_R E^2(r)\cdot S_m(r)\ r\mathrm{d}r\right|^2}{\int_R |E^2(r)|^2\ r\mathrm{d}r\ \int_R |S_m(r)|^2\ r\mathrm{d}r} \tag{3.5}$$

Table 3.1 – The resonance frequencies of radial transverse acoustic waves in SMF.

m	Calculation (MHz)	Measurement (MHz)
1	36.5	35.0
2	83.8	85.0
3	131.2	132.5
4	178.8	182.5
5	226.4	230.0
6	273.9	277.5
7	321.5	325.0
8	369.2	372.5
9	416.7	420.0
10	464.2	467.5

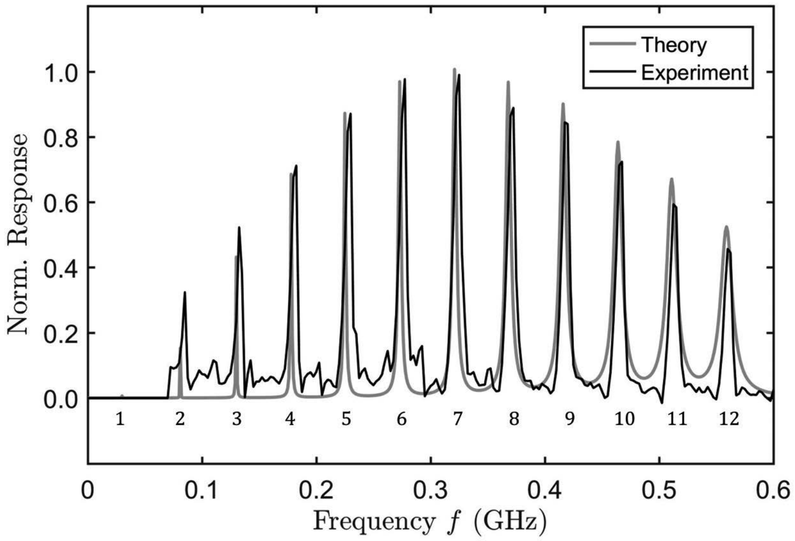

Figure 3.2 – Theoretical and experimental FSBS spectrum.

$S_m(r)$ is the dilatation profile of mode m. The profiles of normalised dilatation and optical field are shown in Fig. 3.3. For low acoustic resonance frequency, the optical mode falls inside the large central lobe of the acoustic dilatation, hence their overlap is small. As for higher resonance frequency, the optical mode overlap with part of the dilatation profile that is negative, which reduces the total value of the overlap integral. Thus, the spectrum of FSBS in SMF consists of multiple resonance peaks with peak amplitudes that form a bell shape. The theoretical spectrum of FSBS is plotted alongside with the experimental spectrum, shown in Fig. 3.2. The resonance peaks are wrapped by the effective gain of each mode determined from the overlap factor Q^2, the highest peak is found to be the 7th mode. As the resonance frequencies are inversely proportional to the radius of fibre (see Eq. 3.4), reducing the fibre size will increase the resonance frequencies as well as the separation between resonance peaks.

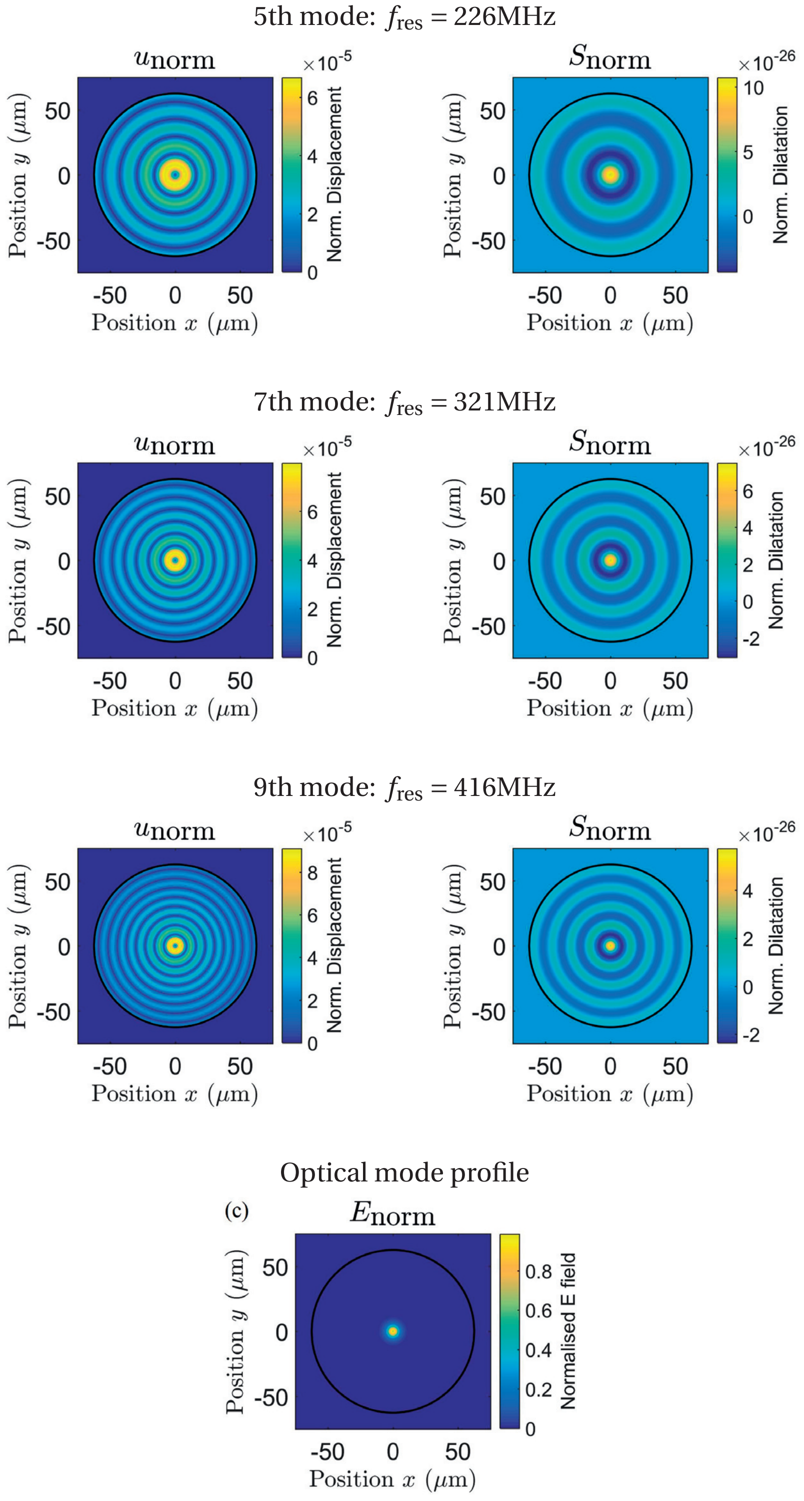

Figure 3.3 – The normalised displacement u_{norm} and dilatation S_{norm} profile of the 5th, 7th and 9th radial transverse acoustic mode. The normalised optical mode profile (bottom).

A Dirac delta function has a constant spectral density. When an extremely short and intense optical pulse close to a Dirac delta function is introduced into the fibre, all transverse acoustic modes are generated simultaneously. The impulse response of stimulated transverse acoustic waves in time domain is then given by the sum of individual acoustic oscillations at their respective resonance frequencies, given by

$$R(t) = \sum_{m}^{\infty} A_m \sin(\omega_m t) \tag{3.6}$$

where A_m is the gain of of individual mode m proportional to the overlap factor Q^2, ω_m is the resonance frequency of the mth mode. The theoretical impulse response of FSBS is plotted together with the experimental trace, as shown in Fig. 3.4.

The FSBS resonance frequencies are given by the solutions y_m of Eq. 3.3. For higher order solutions, the difference between two consecutive order of solutions is close to π, hence the separation between resonance peaks $\Delta\nu$ can be approximated by

$$\Delta\nu \approx \frac{V_{\mathrm{L}}}{2a} \tag{3.7}$$

which is similar to the free spectral range (FSR) of 1D optical cavity. For standard SMF with cladding diameter of 125 μm, $\Delta\nu$ calculated based on Eq. 3.7 is 47.6 MHz, which agrees with the measurements in Table 3.1. Since this is an approximation and the actual resonances are not perfectly separated by $\Delta\nu$, the impulse response exhibits a pseudo periodical pulse pattern (see Fig. 3.4(b)), which has a period of $\Delta t_r = 1/\Delta\nu$ where Δt_r is approximately 21 ns for standard SMF.

3.3 Detecting the response of FSBS

The stimulated transverse acoustic waves induce small refractive index change Δn in the fibre core because of the photoelastic effect in silica material. Refractive index change Δn can be found from the permittivity change $\Delta\epsilon$. $\Delta\epsilon$ of an isotropic material is given by Eq. 1.86. For transverse acoustic waves, as $k = 0$, S_{zz} is zero. $\Delta\epsilon$ is determined by S_{rr} and $S_{\theta\theta}$

$$\begin{aligned}\Delta\epsilon &= \Delta\epsilon_{ii} \\ &= -\epsilon^2(p_{11}+p_{12})(S_{rr}+S_{\theta\theta}) \\ &= -\epsilon^2(p_{11}+p_{12})S\end{aligned} \tag{3.8}$$

where S is the dilatation. The refractive index and permittivity is related by $n + \Delta n = \sqrt{\epsilon + \Delta\epsilon}$. Through Taylor expansion of $\Delta\epsilon$ up to the first order, Δn is approximated as

$$\Delta n \approx \frac{1}{2n}\Delta\epsilon \tag{3.9}$$

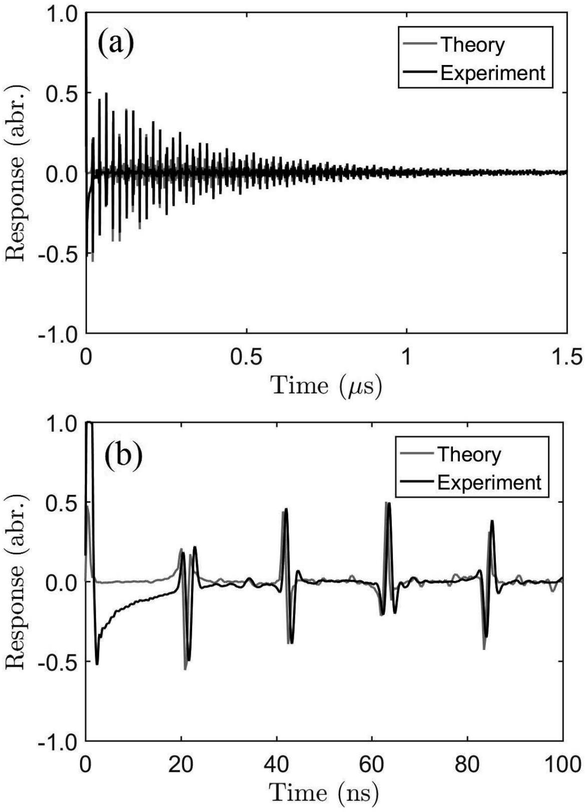

Figure 3.4 – The impulse response of FSBS when the fibre without coating is exposed to air. (a)(b) The experimental result is overlaid on the theoretical trace. (a) The decay time τ of the transverse acoustic wave is found to be around 1 μs by comparing with the experimental result. (b) The initial part of the trace ($t \leqslant 100$ ns) exhibits pseudo periodical pattern with time separation Δt of around 21 ns.

Therefore, by substituting Eq. 3.8 into Eq. 3.9, Δn due to strain is obtained as

$$\Delta n = -\frac{n^3(p_{11}+p_{12})}{2}S \tag{3.10}$$

This refractive index change can be probed by a guided light wave at a different wavelength. Since the group velocity of the probe light and the phase velocity of transverse acoustic wave are almost equal, the probe light follows the same wave front of the transverse acoustic wave while propagating along the fibre, therefore experiencing Δn that is unique to each point in the travelling transverse acoustic wave, such scenario is equal to the probe light being phase-modulated at the acoustic resonance frequency. This condition is analogous to Raman-Nath effect, which describes a propagating light that is phase-modulated by the transverse acoustic standing waves [15, 70]. The phase shift ξ of the probe light is given by

$$\xi = \beta L = \frac{2\pi L}{\lambda}\Delta n \tag{3.11}$$

where β is the propagation constant, L is the length of fibre and λ is the wavelength of light in vacuum. The phase signal in probe could then be read using an interferometer, which converts the optical phase change to intensity change that is detectable by a photodiode.

3.3.1 Optical and acoustic waves coupling

In FSBS, the optical pump and probe waves are propagating alongside each other in the same direction. The consequence is that the generated transverse acoustic waves simultaneously phase modulate both pump and probe waves and result in signal mixing that complicates the extraction of the probe signal. Thus, the generation and detection of transverse acoustic waves are separated to isolate the probe signals from the pump wave. In the experiment, the pump wave consists of two CW light waves with frequency separation that matches the frequency of an acoustic resonance peak. Through the beating between the two frequency components, the transverse acoustic wave is generated inside the fibre. On the other hand, the CW probe wave is placed at a distant wavelength which is ~20 nm away from the pump wavelength to ensure that the probe wave is free from the interference with the pump wave. The axial amplitude variation of probe wave can be analysed using similar coupled wave approach as in section 1.5. Because of the phase modulation by the transverse acoustic wave, the probe wave consists of multiple frequency sidebands that are propagating in forward direction, written as

$$E(z,t) = E_0(r) \sum_{n=-\infty}^{\infty} A_n(z,t) e^{i(k_n z - \omega_n t)} + \text{c.c.} \tag{3.12}$$

Since wave vector $q \approx 0$, the acoustic field at a particular resonance frequency generated by the optical pump is given by

$$u(z,t) = u_0(r) B e^{-i\Omega t} + \text{c.c.} \tag{3.13}$$

Here, the amplitude of the transverse acoustic field B is independent of z. Substitute Eq. 3.13 into the acoustic wave equation (Eq. 1.96) and follow through similar mathematical manipulations from Eq. 1.98 to Eq. 1.101, B is obtained as

$$\begin{aligned} B &= -\epsilon_0 \chi \rho^{-1} Q \frac{A_\text{p}^{(1)} A_\text{p}^{(2)*}}{\Omega_\text{B}^2 - \Omega^2 - i\Omega\Gamma_\text{B}} \\ &= \frac{-\epsilon_0 \chi Q}{\rho \Omega_\text{B} \Gamma_\text{B}} |A_\text{p}|^2 S(\Omega) \end{aligned} \tag{3.14}$$

$S(\Omega)$ is the normalised complex Lorentzian function, defined as

$$S(\Omega) = \frac{1}{-2\Omega' + i} \tag{3.15}$$

where Ω' is the transformed frequency, given by

$$\Omega' = \frac{\Omega - \Omega_a}{\Gamma_\mathrm{B}} \tag{3.16}$$

For the nonlinear polarization $P_\mathrm{NL} = \epsilon_0 \Delta\epsilon E$, the permittivity change $\Delta\epsilon$ due to the presence of transverse acoustic wave is given in Eq. 3.8, $\Delta\epsilon = -\epsilon^2 pS = -\chi S$. The photoelastic constant p is given by $p = p_{11} + p_{12}$ and the nonlinear parameter χ is defined as $\chi = \epsilon^2 p = n^4 p$. Using similar analysis from Eq. 1.103 to Eq. 1.110, the probe wave is written as

$$\begin{aligned}\frac{\partial A_n}{\partial z} &= \frac{-i\omega\chi Q}{2nc}\left(A_{n-1}B + A_{n+1}B^*\right)\\ &= \frac{i\omega\epsilon_0\chi^2 Q^2 \left|A_\mathrm{p}\right|^2}{2nc\rho\Omega_\mathrm{B}\Gamma_\mathrm{B}A_\mathrm{eff}}\left(A_{n-1}S(\Omega) + A_{n+1}S^*(\Omega)\right)\\ &= iP_\mathrm{p}\left(\gamma_\mathrm{A}(\Omega)A_{n-1} + \gamma_\mathrm{A}^*(\Omega)A_{n+1}\right)\end{aligned} \tag{3.17}$$

In Eq. 3.17, P_p is the pump power, given by $P_\mathrm{p} = 2n\epsilon_0 c A_\mathrm{eff}\left|A_\mathrm{p}\right|^2$ and γ_A is the acoustic nonlinear coefficient, given by

$$\gamma_\mathrm{A}(\Omega) = \frac{\omega\chi^2 Q^2}{4n^2c^2\rho\Omega_\mathrm{B}\Gamma_\mathrm{B}A_\mathrm{eff}^2}S(\Omega) \tag{3.18}$$

A_eff is the effective optical mode area. For fundamental Gaussian mode, A_eff is approximately equal to $A_\mathrm{eff} \approx \pi w^2$, where w is the radius at $1/e^2$ intensity. At the resonance peak Ω_B, the transformed frequency of the Lorentzian function is zero, $\Omega' = 0$. Thus $S(\Omega)$ is an imaginary unit i and the coupled equation can be rewritten as

$$\frac{\partial A_n}{\partial z} = |\gamma_\mathrm{A}(\Omega_\mathrm{B})|P\left(A_{n-1} - A_{n+1}\right) \tag{3.19}$$

By comparing with an identity of Bessel function as given below

$$\frac{\partial J_n(x)}{\partial x} = \frac{1}{2}(J_{n-1}(x) - J_{n+1}(x)) \tag{3.20}$$

Equation 3.19 is found to have solutions A_n in the form of Bessel functions $A_n(z) = A_n(0)J_n(\xi)$. Substitute this solution form into Eq. 3.19 yield

$$\begin{aligned}\frac{\partial J_n(\xi)}{\partial \xi} &= \frac{1}{2}(J_{n-1}(\xi) - J_{n+1}(\xi))\\ &= \frac{1}{2|\gamma_\mathrm{A}(\Omega_\mathrm{B})|P_\mathrm{p}}\frac{\partial A_n(z)}{\partial z}\end{aligned} \tag{3.21}$$

where the effective length ξ is given by

$$\begin{aligned}\xi &= 2|\gamma_{\mathrm{A}}(\Omega_{\mathrm{B}})|P_{\mathrm{p}}z \\ &= \frac{\pi n^5 p^2 Q^2}{\lambda c \rho \Omega_{\mathrm{B}} \Gamma_{\mathrm{B}} A_{\mathrm{eff}}^2} P_{\mathrm{p}} z\end{aligned} \tag{3.22}$$

The solution in Bessel functions indicates that the probe wave experiences phase modulation by the transverse acoustic wave. The modulation index is given by ξ, which is a function of the pump power P_{p} and distance in fibre z. The refractive index perturbation Δn can be expressed by combining Eq. 3.11 and Eq. 3.22, which results in

$$\Delta n = \frac{n^5 p^2 Q^2 P_{\mathrm{p}}}{2 c \rho \Omega_{\mathrm{B}} \Gamma_{\mathrm{B}} A_{\mathrm{eff}}^2} \tag{3.23}$$

Consider the following parameters for standard single-mode fibre: effective mode area $A_{\mathrm{eff}} = 85\ \mu\mathrm{m}^2$, overlap factor $Q^2 \approx 0.1$, the selected FSBS resonance frequency $\Omega_B = 2\pi f_{\mathrm{res}}$ where $f_{\mathrm{res}} = 321$ MHz, the FSBS resonance linewidth $\Gamma_{\mathrm{B}} = 2\pi\Delta\nu$ which is estimated based on the reported bulk viscosity of silica $\Delta\nu \approx 0.1$ MHz [46, 86] (The experimentally measured linewidth is slightly broader ($\Delta\nu \approx 0.3$ MHz) because of the ununiform fibre diameter). Using Eq. 3.18, the acoustic nonlinear coefficient $|\gamma_{\mathrm{A}}(\Omega_{\mathrm{B}})|$ is estimated as ~23.8 $\mathrm{W}^{-1}\mathrm{km}^{-1}$. Compare this value to the estimation in [46] for radial mode $m = 6$ in SMF-28 (8 $\mathrm{W}^{-1}\mathrm{km}^{-1}$), the value calculated here is larger because the fibre considered here is without coating thus having greater FSBS nonlinear gain. For the estimation of Δn, assume an input power $P_{\mathrm{p}} = 1$ W and the parameters mentioned above, Δn is calculated as ~8×10^{-9} using Eq. 3.23, which is in the same order of magnitude as the experimental value (~2.5×10^{-9}) that is obtained from the distributed FSBS measurement (refer to Fig. 3.19 in section 3.6). However, the Δn value calculated here provides only an estimation as the precise power in experiment was not obtained.

3.3.2 Experimental setup

The response of FSBS can be measured through either a time or a frequency domain technique. The experimental setup for FSBS activation and detection is shown in Fig. 3.5. An intensity-modulated optical pulse at $\lambda = 1551$ nm serves as the pump source (activation light) for FSBS. For time-domain measurement technique, a short pulse of 1 ns pulse duration is shaped from the incoming distributed feedback (DFB) laser by an electro-optic modulator (EOM) whereas for the frequency-domain method, a long pulse of 500 ns is first shaped from the laser by a semiconductor optical amplifier (SOA) and subsequently intensity-modulated by an EOM at FSBS frequency where the modulation signal is provided by a vector network analyzer (VNA). The purpose of introducing the long pulse is to suppress the unwanted response due to Kerr cross-phase modulation by means of selectively gating away the affected time duration in the response trace before detection (discussed in the subsequent section). The generated optical pulse in either technique is amplified by an Erbium doped fibre amplifier (EDFA) to produce a peak power of around 1 W. The duration of the pump pulse is optimised such that it generates the strongest transverse acoustic waves for detection. The pump pulse should be long enough to saturate the acoustic wave yet it should be maintained as short as possible at the same time so that higher amplification could be achieved (for the amplification of an optical pulse using a typical EDFA, the average peak amplification reduces as the pulse duration increases because of the gain saturation effect[49]).

A CW light from another DFB laser at a different wavelength of 1534 nm is used for probing the induced phase modulation through a fibre Sagnac interferometer, in which the incoming light is split into two arms by a coupler. The two separated light waves propagate in opposite directions inside the fibre loop and eventually meet again and interfere at the coupler. As both counter-propagating light waves in the Sagnac loop go through the same path and experience identical static refractive index perturbations, they have equal optical phase during interference and do not produce any intensity change. However, as the transverse acoustic wave propagates along the fibre at the group velocity of guided light, the probe light that travels in the same direction as the pump light will experience an acoustically induced Δn inside the fibre. Since each temporal point of the CW light and the transverse acoustic wave are propagating at the same speed, the CW light will experience time-dependent phase change that corresponds to the time feature of the transverse acoustic wave. On the other hand, the probe light that travels in opposite direction to the pump light crosses an undulating Δn which averages to zero phase change in time. This non-reciprocal light phase modulation allows Sagnac interferometer to be used for FSBS detection with the advantage of suppressing random refractive index perturbations in the fibre due to temperature and strain variations.

To detect the FSBS response from the sensing fibre only, a tunable narrow bandpass filter (BPF) is adjusted to the probe wavelength and is placed in the Sagnac loop after the sensing fibre where the pump light is blocked from travelling in the rest of the loop. Another BPF adjusted to the same wavelength is placed before the photodetector to further avoid the pump light from being detected. For the time domain measurement, the electrical signal from the photodiode is read by an high speed oscilloscope whereas for the frequency domain measurement, the signal is read by the VNA, which is synchronized to the pump modulation frequency and configured to sweep across a chosen FSBS resonance peak. The VNA acts as a narrow band filter that detects the electrical power at the same frequency as the generated sinusoidal signal. It could also be replaced by an electrical spectrum analyser (ESA) with a built-in tracking generator. The experimental results obtained through frequency and time domain techniques are given in Fig. 3.2 and Fig. 3.4, respectively.

3.3.3 Kerr-induced spectral distortion

The spectral shape of FSBS resonance is a Lorentzian function. However, the detected FSBS resonance spectrum exhibits Fano shape due to Kerr effect [86, 84]. The presence of Kerr effect causes cross-phase modulation, its impact on the probe wave is described by the coupled

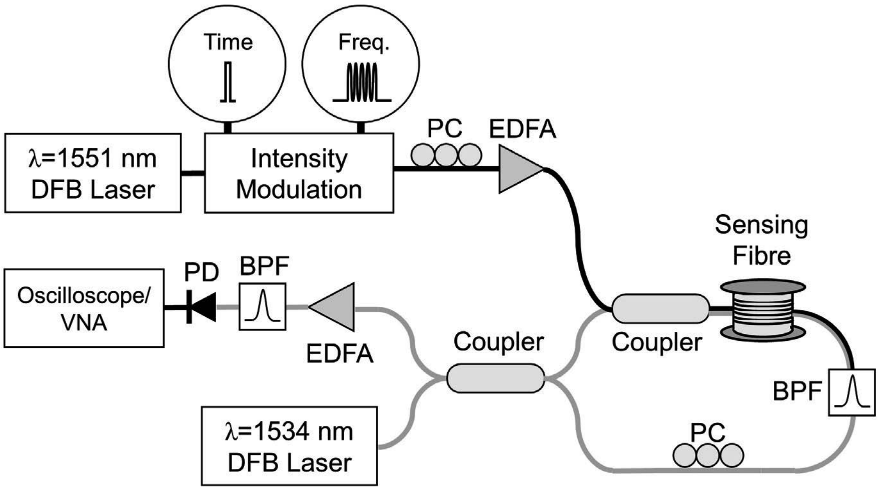

Figure 3.5 – Experimental setup used for detecting the response of FSBS. The uppermost branch (black line) gives the pump light for the generation of transverse acoustic waves in the sensing fibre. The probe (grey line) is configured as a Sagnac interferometer that converts the time dependent phase-shift induced by the transverse acoustic waves to intensity change that is detectable by a photodiode. The components are labelled as follows: PC, polarisation controller; EDFA, Erbium doped fibre amplifier; BPF, bandpass filter; PD, photodiode.

wave equations of 4-wave mixing [39], given by

$$\frac{\partial A_s}{\partial z} = i2n\epsilon_0 c A_{\text{eff}}\gamma_k \left[\left(|A_s|^2 + 2\left(|A_i|^2 + |A_p|^2\right)\right) A_s + A_i^* A_p^2 \exp(-i\Delta\beta z)\right] \tag{3.24}$$

where A_s is the signal wave, A_p is the pump wave, A_i is the idler wave, $\Delta\beta$ is the phase mismatch and γ_k is the Kerr nonlinear parameter, given by $\gamma_k = n_2\omega / cA_{\text{eff}}$, where n_2 is the nonlinear index coefficient ($n_2 \approx 2.6 \times 10^{-20}$ m^2 W^{-1} for bulk silica) [3]. Assume that the fibre is short and the initial signal and idler power are much smaller than the pump power, Eq. 3.24 can be rewritten as

$$\frac{\partial A_s}{\partial z} = i4n\epsilon_0 c A_{\text{eff}}\gamma_k |A_p|^2 A_s \tag{3.25}$$

Equation 3.25 shows that the presence of Kerr effect produces an additional phase shift to the probe wave, thus its contribution can be added to the FSBS coupled wave equations Eq. 3.17. For the purpose of analysing the spectral shape, only the Stokes component from Eq. 3.17 is considered. The combine effect is then written as

$$\begin{aligned}\frac{\partial A_n}{\partial z} &= i2n\epsilon_0 c A_{\text{eff}} |A_p|^2 (\gamma_{\text{A}}(\Omega) + 2\gamma_{\text{k}}) A_n \\ &= i2n\epsilon_0 c A_{\text{eff}} |A_p|^2 \gamma_m(\Omega) A_n \\ &= iP_{\text{p}}\gamma_m(\Omega) A_n\end{aligned} \tag{3.26}$$

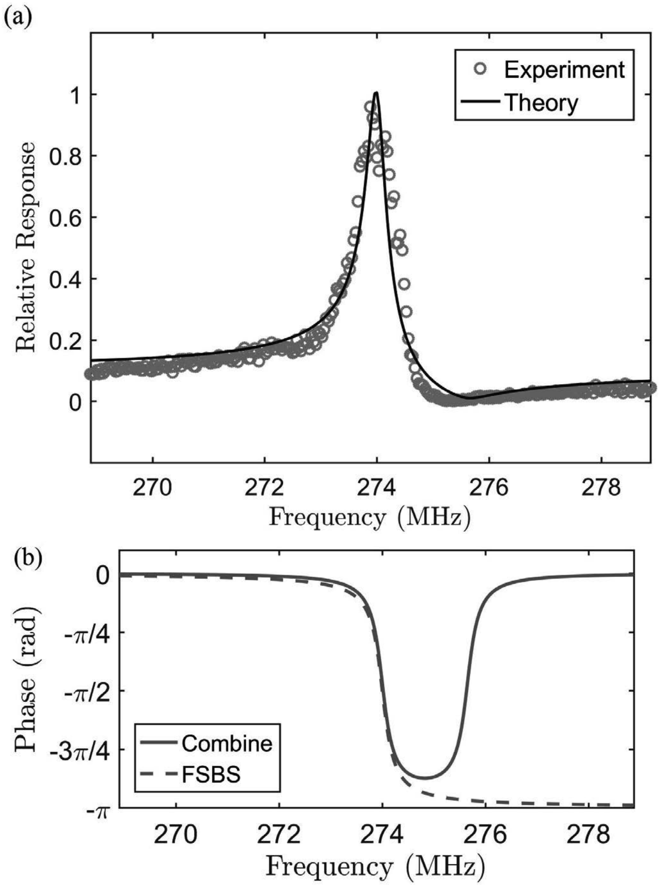

Figure 3.6 – The combination of FSBS resonance and Kerr effect. (a) The detected resonance spectrum exhibits Fano shape, described as the combination of a complex Lorentzian function (FSBS resonance peak) and the Kerr-induced phase shift that is uniform in spectrum. (b) The simulated signal phase shift of the combined effect compared with the signal phase shift due to FSBS effect alone.

The solution of Eq. 3.26 is a harmonic wave with phase shift $\xi = P_\mathrm{p}\gamma_m(\Omega)z$. The refractive index perturbation $\Delta n(\Omega)$ can be obtained from the phase shift, given by

$$\Delta n(\Omega) = \frac{\lambda P_\mathrm{p}\gamma_m(\Omega)}{2\pi} \tag{3.27}$$

where $\gamma_m(\Omega)$ is the total nonlinear parameter, define as

$$\gamma_m(\Omega) = \gamma_\mathrm{A}(\Omega) + 2\gamma_\mathrm{k} \tag{3.28}$$

To compare the contribution of FSBS and Kerr effect, $\gamma_m(\Omega)$ is normalized by the acoustic nonlinear coefficient at the resonance peak $|\gamma_\mathrm{A}(\Omega_\mathrm{B})|$, given by

$$\gamma_m^{(\mathrm{norm})}(\Omega) = S(\Omega) + \frac{2\gamma_\mathrm{k}}{|\gamma_\mathrm{A}(\Omega_\mathrm{B})|} \tag{3.29}$$

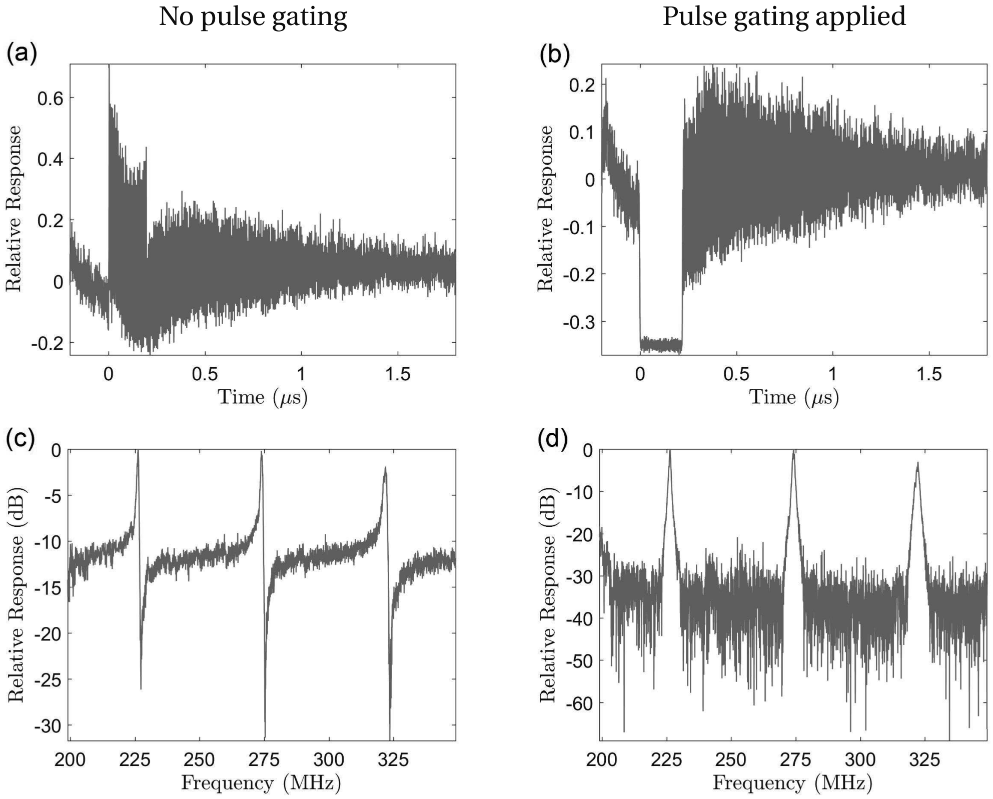

Figure 3.7 – Temporal traces and the corresponding VNA spectra of the detected signal at photodetector (a)(c) without and (b)(d) with pulse gating.

The normalised resonance spectrum of this combined effect is given by $|\gamma_m^{(\mathrm{norm})}(\Omega)|$, as shown in Fig 3.6(a), which is plotted together with the experimental result. The simulated signal phase shift of the combined effect is compared with the signal phase shift due to FSBS effect alone, as shown in Fig 3.6(b). At the centre of the FSBS resonance peak, the phase of signal due to FSBS effect is shifted by $\pi/2$ whereas the phase of signal due to Kerr effect does not change. This way, the presence of Kerr signal cancels the FSBS signal and results in reduced amplitude of the combined response.

By fitting the theoretical curve with the experimental data, the ratio of Kerr nonlinear coefficient γ_k to the FSBS nonlinear coefficient $|\gamma_\mathrm{A}(\Omega_\mathrm{B})|$ is found to be $\gamma_k/|\gamma_\mathrm{A}(\Omega_\mathrm{B})| \approx 0.05$, from which γ_k can be retrieved, $\gamma_k \approx 1.2\ \mathrm{W}^{-1}\mathrm{km}^{-1}$. The nonlinear index n_2 estimated from the experimental result is approximately $2.5 \times 10^{-20}\ \mathrm{m}^2\mathrm{W}^{-1}$, which is in the same order of magnitude as the reported value $2.6 \times 10^{-20}\ \mathrm{m}^2\mathrm{W}^{-1}$ [3].

Nevertheless, numerically eliminating Kerr effect from the spectrum requires prior knowledge of the fibre nonlinear parameter, therefore the separation of FSBS and Kerr effects could become complicated for different optical fibres or pump conditions. Here, the effectiveness of a pulse gating method is demonstrated. Knowing that Kerr effect is instantaneous whereas transverse acoustic resonance remains for hundreds of nanoseconds for a typical fibre, the contribution of FSBS and Kerr effect can be separated in the temporal domain. The pump wave is carved into a long rectangular pulse using an intensity modulator and synchronized with another intensity modulator in the detection part which suppresses the duration related to the pump pulse before the detection. The temporal traces and the corresponding VNA spectra of the detected response without and with pulse gating are compared. Without pulse gating, the non-symmetric resonance spectra are clearly observed (Fig. 3.7(c)). By applying pulse gating, only the acoustic tail is detected, eliminating Kerr contribution (compare Fig. 3.7(a) and (b)) and the resonance linewidth could be retrieved without ambiguity (Fig. 3.7(d)).

3.4 Acoustic impedance sensing

FSBS has been exploited for various innovative acoustic-based metrologies, namely for fibre diameter estimation [59], sound velocity measurement [74], strain, temperature sensing [81, 80] and more recently for measuring the acoustic impedance of surrounding liquid materials[6]. The latter sensing application allows the mechanical properties of an external material to directly impact the detected optical signal. By removing the acrylate coating of a standard single-mode fibre (SMF), transverse acoustic waves in the fibre cladding are allowed to interact directly with the fibre surroundings through reflection. Resembling a cavity ring-down technique, the acoustic decay rate is determined by the multi-pass reflection loss at the boundary, which could be used to calculate the acoustic impedance of the surrounding liquid.

The first fibre-based acoustic impedance sensor is devised in Bar-Ilan University, Israel [6], which is based on the time domain technique where a high intensity short pulse approximating a delta function is launched into the fibre to generate multiple acoustic modes simultaneously. Through fitting the damped oscillation trace with an exponential decay function, the decay time τ is obtained. The boundary reflectivity r, followed by the acoustic impedance of the outer material Z_o are then calculated from τ. Similar analysis can be carried out with the frequency domain technique, in which the pump light is modulated at a certain frequency that is swept across a selected acoustic resonance peak. Linewidth $\Delta\nu$ of the resonance is recovered from the Lorentzian fitting of the acquired resonance spectrum and is used to retrieve r and Z_o. A few variants of FSBS frequency sweeping methods have been described previously [86, 67]. All reported FSBS frequency domain techniques rely on frequency sweeping of pump light and interrogated through an interferometer. The sensing technique used here is based on a Sagnac interferometer as described in the previous section.

3.4.1 Retrieving the acoustic impedance

The acoustic impedance of the detected medium is retrieved by finding the acoustic reflectivity at the cladding-surroundings boundary [6]. Because of the large acoustic impedance mismatch between fibre bulk material (silica) and the external medium, part of the transverse acoustic waves are reflected back and trapped in the transversal cavity. The intensity of subsequent oscillation cycles reduces exponentially in time due to the reflection loss at the fibre

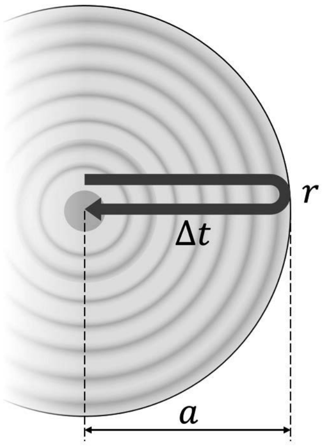

Figure 3.8 – Illustration of acoustic round-trip and reflection at fibre boundary.

boundary and the internal loss (dissipation, structural inhomogeneity, etc.). The reflectivity r, which depends on the acoustic impedance mismatch between fibre bulk and the surrounding medium, is given by

$$r = \left| \frac{Z_f - Z_o}{Z_f + Z_o} \right| \tag{3.30}$$

where Z_f and Z_o are the acoustic impedances of silica and the surrounding medium, respectively. The acoustic impedance of silica is 13.1×10^6 kg m^{-2}s^{-1} [1]. The decay time of the transverse acoustic cavity is estimated from the intrinsic material loss and the imperfect boundary reflection. Since the acoustic wavelength is much smaller than the fibre diameter, the fibre cross-section can be assumed as a 1D acoustic resonator similar to an optical Fabry-Pérot cavity, as illustrated in Fig. 3.8. Note that this assumption is only valid for higher order transverse acoustic modes of ($m \geq 5$), for which the separation between two consecutive resonance peaks is close the FSR of a 1D resonator, as given by Eq. 3.7. Consider the intrinsic distributed loss coefficient α_s and the reflectivity r, the overall loss can be described by the effective distributed loss coefficient α_m, given by

$$A_0 \exp(-2\alpha_m a) = A_0 r \exp(-2\alpha_s a) \tag{3.31}$$

where A_0 is the initial amplitude of the acoustic wave and a is the fibre radius. Taking natural logarithm of both sides and rearranging terms results in

$$\alpha_m = \alpha_s - \frac{1}{2a} \ln(|r|) \tag{3.32}$$

The acoustic loss α can be related to the decay time τ by

$$\alpha = \frac{1}{V_L \tau} \tag{3.33}$$

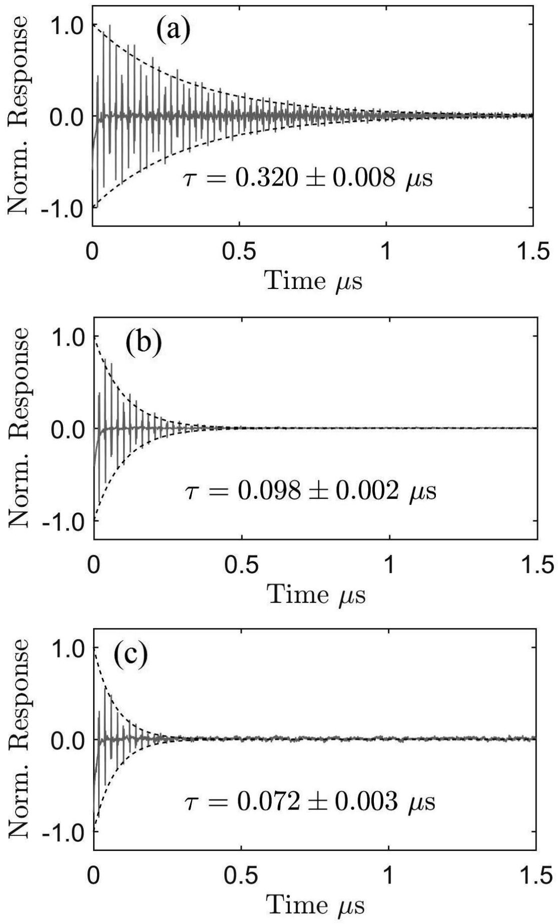

Figure 3.9 – Time response of FSBS to a 1 ns short impulse when fibre is surrounded by (a) air, (b) ethanol and (c) water. Time constant τ is determined from fitting the envelope of the signal with exponential decay function. (a) to (c) are normalised by the respective initial amplitude.

Thus, Eq. 3.32 can be rewritten as

$$\frac{1}{\tau_{\mathrm{m}}} = \frac{1}{\tau_{\mathrm{s}}} + \frac{1}{\Delta t}\ln\left(\frac{1}{|r|}\right) \tag{3.34}$$

where τ_m and τ_s are the effective (measured) and intrinsic (air as surrounding) acoustic decay time constants, respectively. Δt is the acoustic round-trip time, given by

$$\Delta t = \frac{2a}{V_{\mathrm{L}}} \tag{3.35}$$

To express Eq. 3.34 in the frequency domain, consider the relationship between the exponential decay time τ and the linewidth $\Delta\nu$ of a Lorentzian function, given by

$$\Delta\nu = \frac{1}{\pi\tau} \tag{3.36}$$

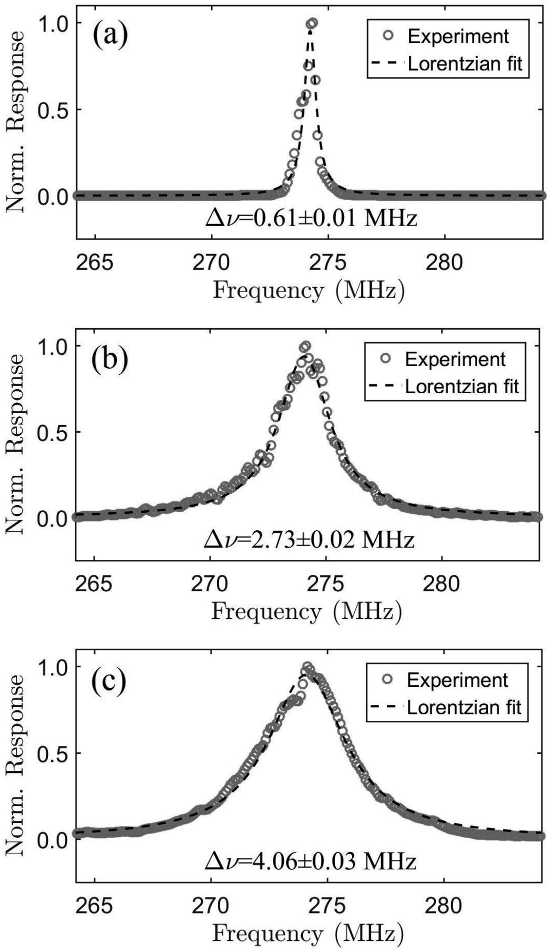

Figure 3.10 – Resonance spectrum of transverse acoustic wave when fibre is surrounded by (a) air, (b) ethanol and (c) water. Linewidth $\Delta\nu$ is determined from fitting the resonance spectrum with Lorentzian function. (a) to (c) are normalised by the respective peak intensity.

and the frequency separation $\Delta\nu_{\text{sep}}$ is given by the inverse of round-trip time.

$$\Delta\nu_{\text{sep}} = \frac{1}{\Delta t} \tag{3.37}$$

Substitute Eq. 3.36 and Eq. 3.37 into Eq. 3.34 results in the following relation in frequency domain (as discussed above, this relation is only valid for higher order modes).

$$\Delta\nu_{\text{m}} = \Delta\nu_{\text{s}} + \frac{\Delta\nu_{\text{sep}}}{\pi}\ln\left(\frac{1}{|r|}\right) \tag{3.38}$$

where $\Delta\nu_{\text{m}}$, $\Delta\nu_{\text{s}}$ and $\Delta\nu_{\text{sep}}$ are the linewidth of the measured resonance spectrum with a surrounding liquid medium, linewidth due to intrinsic loss (air as surroundings) and the frequency separation between peaks, respectively. Thus, the resonance linewidth $\Delta\nu_{\text{m}}$ is the linear sum of the linewidth broadening due to the intrinsic loss and the intensity decay due to non-unity reflectivity at the fibre boundary. The linewidth due to intrinsic loss $\Delta\nu_\mathrm{s}$ is obtained when the uncoated optical fibre is surrounded by air. Because of the large acoustic impedance difference between silica and air (acoustic impedance of silica: 13.1 $\times 10^6$ kg m^{-2}s^{-1}, air: 344 kg m^{-2}s^{-1} [1]), the reflectivity r is close to unity, the measured linewidth $\Delta\nu_\mathrm{m}$ in Eq. 3.38 is then equal to the linewidth due to intrinsic loss $\Delta\nu_\mathrm{s}$.

The measured FSBS time response for different surrounding materials are shown in Fig. 3.9. The data processing steps to obtain the acoustic impedance are detailed as follows [6]: First, fast Fourier transform is applied to the measured time response trace to obtain the FSBS spectrum. Then, one of the transverse acoustic resonance mode is selected from the spectrum by numerical filtering. Subsequently, the spectrum of the selected resonance mode is transformed back to time domain by applying inverse fast Fourier transform, the obtained time trace is the time response of the selected resonance mode. Next, the envelope of this time trace is normalised by its initial amplitude and fitted to an exponential decay function $\exp(-t/\tau)$ to retrieve the time constant τ, for which the values in air, ethanol and water are obtained as 0.320 ± 0.008 μs, 0.098 ± 0.002 μs and 0.072 ± 0.003 μs, respectively. Based on Eq. 3.34, the calculated acoustic impedances are $0.972 \pm 0.027 \times 10^6$ kg m^{-2}s^{-1} and $1.474 \pm 0.071 \times 10^6$ kg m^{-2}s^{-1} for ethanol and water, respectively.

For the frequency domain mesurements, the experimental results of the acoustic resonance linewidth in air, water and ethanol are shown in Fig. 3.10. The obtained linewidth of of air, ethanol and water are 0.61 ± 0.03 MHz, 2.73 ± 0.05 MHz and 4.06 ± 0.07 MHz, respectively. Using Eq. 3.38, acoustic impedances of ethanol and water are found to be $0.915 \pm 0.009 \times 10^6$ kg m^{-2}s^{-1} and $1.485 \pm 0.012 \times 10^6$ kg m^{-2}s^{-1}, respectively. The values obtained from both time and frequency domain method agree with the standard values published in [1] (ethanol: 0.93 $\times 10^6$ kg m^{-2}s^{-1}, water: 1.48 $\times 10^6$ kg m^{-2}s^{-1}).

By numerical fitting the experimental result to the theoretical curve, a confidence bound of the retrieved parameter ($\Delta\nu_m$ or τ) is obtained in the form of standard deviation σ. This σ from the numerical fitting is propagated step-by-step through Eq. 3.38 or Eq. 3.34 using standard error propagations to obtain the measurement uncertainty of the acoustic impedance. However, $\Delta\nu_\mathrm{sep}$, $\Delta\nu_\mathrm{s}$, Δt and τ_s in the error calculations are considered as constants and their uncertainties are not considered.

Both time and frequency domain techniques can retrieve the acoustic impedance of surrounding liquids accurately. Nevertheless, there are advantages and disadvantages associated to both techniques in terms of implementation. Time domain technique requires curve fitting of the experimental data to obtain the acoustic decay time τ, whereas for the frequency domain technique, the acoustic resonance linewidth $\Delta\nu_m$ can be obtained easily from the full-width half maximum (FWHM) of the resonance peak. On the flip side, frequency domain technique requires pulse gating to eliminate the distortion caused by Kerr nonlinearity. In practice, this requires two additional intensity modulators in the experimental setup as compared to the time domain technique and they must be synchronised perfectly.

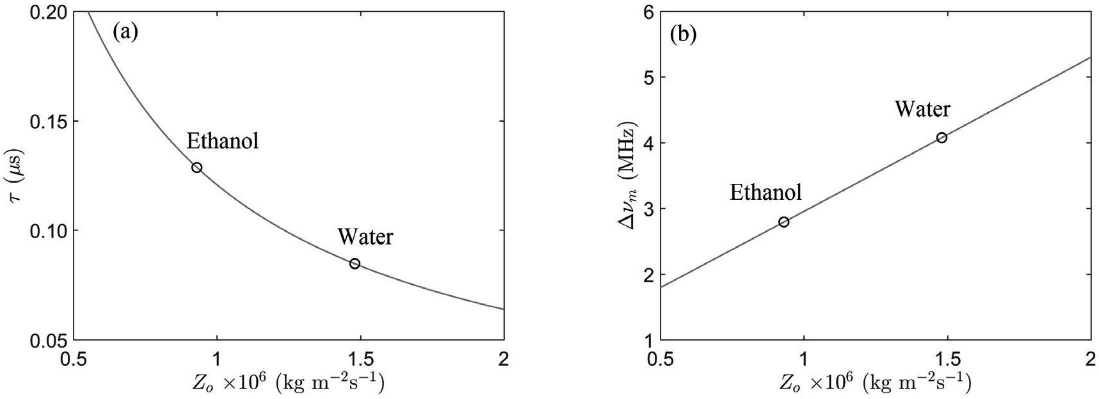

Figure 3.11 – The measured parameters against external acoustic impedance for (a) time domain technique and (b) frequency domain technique.

On the relationship of measurand and the external acoustic impedance Z_o, for time domain technique, the measured parameter τ_m is approximately reciprocal to Z_o, as shown in Fig. 3.11(a) whereas for frequency domain technique, the measured parameter $\Delta\nu_m$ is almost linearly proportional to Z_o, as shown in Fig. 3.11(b). For a typical liquid with Z_o around 0.5 to 2.0 $\times 10^6$ kg m^{-2}s^{-1}, frequency domain method is preferred as Z_o can be easily retrieved with a linear relation. However, time domain method is preferred for measuring external medium with low Z_o because of the decay time τ is long as compared to the narrow resonance linewidth $\Delta\nu_m$ using frequency domain method.

3.5 Thin polymer coated optical fibre

The FSBS-based fibre acoustic impedance sensors described in the previous section rely on stripping away the fibre's acrylate coating that has high acoustic loss to facilitate direct contact between the cladding's boundary and its surroundings. Although this approach greatly simplifies the retrieval of acoustic impedance, the mechanical strength of the sensing fibre is nonetheless compromised. The problem can be overcome by using a commercially available 20 m-long 80 μm-diameter single-mode silica optical fibre coated with a 8 μm-thickness polyimide layer [21, 28]. The thin polyimide layer allows the transverse acoustic waves to traverse between the cladding boundary and the coating boundary with much smaller loss compared with a standard fibre with 62.5 μm-thickness acrylate layer, so that the acoustic waves keep sufficient energy to complete the transverse cavity round-trip (see Fig. 3.12).

The eigenfrequencies of the radial modes for a 80 μm-diameter fibre (listed in Table. 3.2) can be calculated analytically by finding solutions satisfying the characteristic equation as in Eq. 3.3. Here, one of the strongest modes (9th mode, ν_{res} = 636 MHz) is selected for the sensing demonstration. The FSBS spectrum obtained from the experiment (Fig. 3.13) exhibits multiple resonant peaks that could be individually associated to one of the calculated FSBS

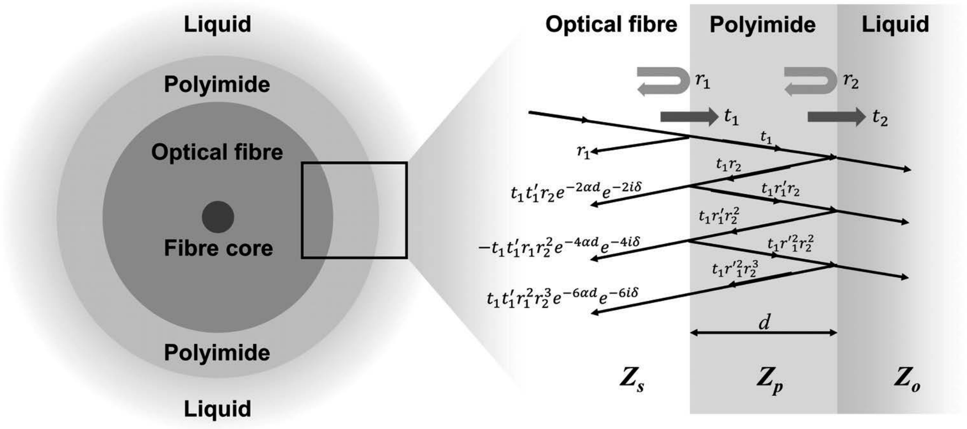

Figure 3.12 – Schematic diagram of the optical fibre with polyimide coating layer that acts as a 1D acoustic thin film. The reflection is angled for clarity purpose, transverse acoustic wave being assumed to be reflected normally from the surfaces.

resonances in the 80 μm-diameter bulk fibre (Table 3.2). This polyimide coated fibre has acoustic round-trip frequency in polyimide layer which is approximately twice as much as that of the silica bulk, causing the even order modes in the polyimide layer to interfere destructively with the acoustic resonances in the bulk fibre thus displaying reduced contrast.

The resonance responses in Fig. 3.13 can be interpreted using the common knowledge on thin film optical coatings: the polyimide coating thickness makes the even-order silica resonances roughly corresponds to a quarter-wave propagation through the layer like an anti-reflection optical coating. In this case, the acoustic impedance contrast at the boundary of fibre bulk increases greatly and the reflected acoustic wave is π-phase shifted, cancelling the incident acoustic wave and leading to the much attenuated resonance intensity. On the contrary, the odd-order resonances, which approximately match a half-wave propagation through the coating, manifests as a replication of the impedance at the interface and makes the presence of the coating acoustically imperceptible. In other words, by a slight adjustment of the coating thickness, its impact can be much reduced and ideally made inexistent. The analogy with the optical coating brings clear insight for a simple interpretation. However, unlike optical waves, the acoustic impedance does not depend on the wave velocity alone, but relies equally on the material density and compressive properties. Due to the added coupled cavity formed by the thin polyimide layer, the odd-order resonances are partially detuned and acts as a strongly dispersive element.

3.5.1 Acoustic impedance measurement

The dynamics of transverse acoustic waves inside the polyimide coated fibre can be simplified as a two-tier process where the acoustic impedance of the external material first affects the global acoustic reflectance of the polyimide coating layer, which in turn changes the FSBS

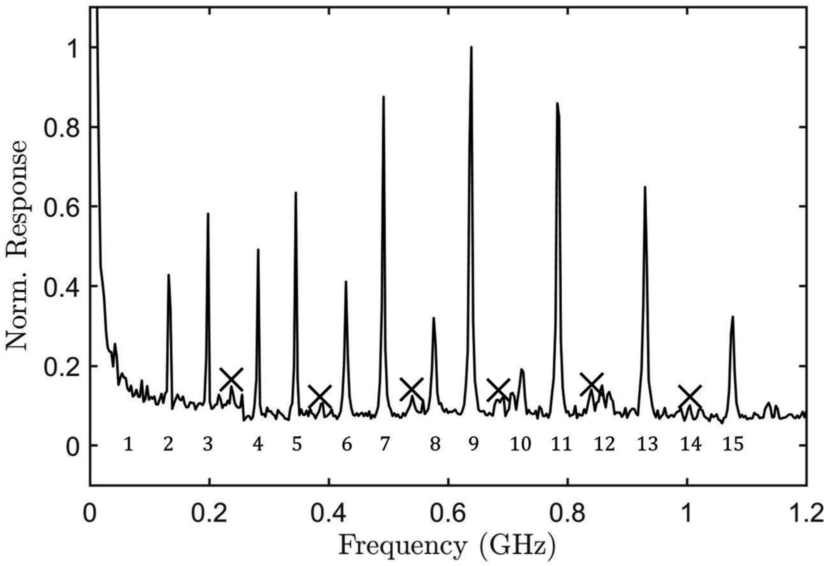

Figure 3.13 – FSBS spectrogram of the 80 μm-diameter polyimide coated fibre that is measured using the frequency domain technique.

spectral linewidth in the silica fibre structure. In other words, the linewidth broadening of FSBS resonance $\Delta\nu_m$, as given by Eq. 3.38, is considered as due to the effective reflectance R at the silica-polyimide boundary as seen by the resonating acoustic waves inside the silica fibre. Given the fiber radius ($a = 40\ \mu$m), $\Delta\nu_{\mathrm{RT}}$ for this fibre is ~74 MHz. The broadening due to the intrinsic loss of the fiber material $\Delta\nu_s$ is a constant that is much smaller as compared to $\Delta\nu_m$, which can be deduced from [6] by assuming that silica has the same acoustic quality factors for the same frequency region, which gives $\Delta\nu_s \approx 0.35$ MHz at 636 MHz.

The acoustic structure of the fiber and the polyimide coating can be approximated as a 1D acoustic layer in between two bulk materials (silica and the surrounding liquids), illustrated in Fig. 3.12. The mathematical description of this acoustic structure is similar to an optical thin film [41]. Note that this assumption is valid only for higher order transverse acoustic modes ($m \geq 5$), as explained in section 3.4. The acoustic impedance of the structure decreases successively following this order: silica-polyimide-exterior. The acoustic impedances of silica and polyimide are $Z_s = 13.1 \times 10^6$ kg/(m^{2}s) and $Z_p = 3.6 \times 10^6$ kg/(m^{2}s), respectively, whereas the acoustic impedances of most liquids-under-test Z_o fall below 2×10^6 kg/(m^{2}s). Energy is assumed to be conserved for the reflection and transmission at the interfaces. The acoustic field reflectance of silica-polyimide and polyimide-exterior boundaries, r_1 and r_2, respectively, are given by

$$r_1 = \left|\frac{Z_s - Z_p}{Z_s + Z_p}\right|, \; r_2 = \left|\frac{Z_p - Z_o}{Z_p + Z_o}\right| \tag{3.39}$$

r_1 is calculated to be 0.5678. The total field reflectance R as seen by the acoustic waves at the silica-polyimide boundary can be derived from the superposition of successive reflected

Table 3.2 – Resonance frequencies of the 80 μm-diameter polyimide coated fibre.

m	Calculation (MHz)	Measurement (MHz)
1	57	45
2	131	132
3	205	198
4	279	282
5	354	345
6	428	429
7	502	492
8	576	576
9	651	636
10	725	723
11	800	786
12	874	870
13	948	930
14	1023	1023
15	1097	1077

waves, the terms are in geometric series, expressed as

$$\begin{aligned} R &= r_1 + t_1 t_1^{'} r_2 e^{-2\alpha d} e^{-2i\delta} - t_1 t_1^{'} r_2^2 e^{-4\alpha d} e^{-4i\delta} + \ldots \\ &= \frac{r_1 + r_2 e^{-2\alpha d} e^{-2i\delta}}{1 + r_1 r_2 e^{-2\alpha d} e^{-2i\delta}} \end{aligned} \tag{3.40}$$

Both t_1 and $t_1^{'}$ are the transmittances from silica to polyimide and vice versa, respectively, they are related by $t_1 t_1^{'} = 1 - r_1^2$. α is the acoustic attenuation constant of polyimide and δ is the phase delay as the acoustic waves propagate through the polyimide layer, given by

$$\delta = \frac{2\pi \nu_{\text{res}}}{V_p} d \tag{3.41}$$

where ν_{res} is the resonant frequency of the transverse acoustic mode (636 MHz), V_p is the speed of sound in polyimide (~2440 m/s) and d is the thickness of the polyimide layer, which can be retrieved accurately from the FSBS spectrum in Fig. 3.13 where the small peaks marked by crosses are due to the leakages from the acoustic resonances inside the polyimide layer. The frequency separation between the peaks is ~151.7 MHz, which gives d = 8.04 μm. δ is then calculated to be ~13.17 rad. Since R is a complex quantity where its argument (phase) is absent in the linewidth $\Delta\nu_m$ measurement, the intensity reflectance R_P should be used in the following analysis

$$R_P = |R|^2 = \frac{r_1^2 + 2\eta r_1 r_2 \cos(2\delta) + \eta^2 r_2^2}{1 + 2\eta r_1 r_2 \cos(2\delta) + \eta^2 r_1^2 r_2^2} \tag{3.42}$$

Here, the polyimide attenuation is written as a power ratio $\eta = \exp(-2\alpha d)$ for the ease of the

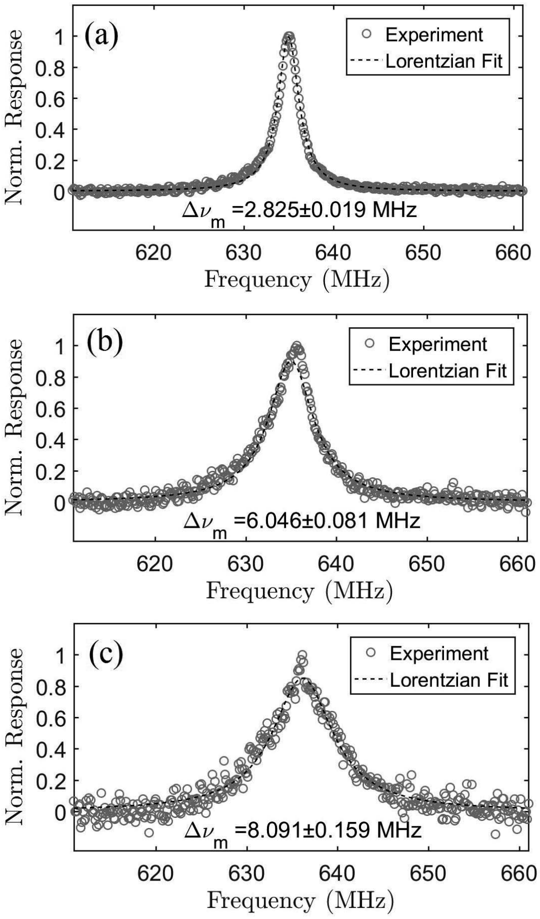

Figure 3.14 – Measured FSBS resonance spectra when the 80 μm thin polyimide coated fibre is surrounded by (a) air, (b) ethanol and (c) water.

subsequent algebraic manipulations.

The polyimide layer acts as a buffer for a fraction of resonating transverse acoustic waves, thus its intrinsic acoustic loss becomes a significant factor that contributes to the FSBS linewidth broadening. The attenuation constant can nevertheless be determined in the condition where the polyimide coated fiber is surrounded by air. In this case, $r_2 \approx 1$, Eq. 3.42 can then be rewritten as

$$\eta^2(R_P r_1^2 - 1) + 2\eta r_1(R_P - 1)\cos(2\delta) + R_P - r_1^2 = 0 \tag{3.43}$$

As R_P is obtained from Eq. 3.38 using the measured linewidth $\Delta\nu_m$ of air surroundings, η can be calculated by solving the quadratic equation Eq. 3.43 and consider only the positive solution. The measured FSBS spectrum around the resonant peak (636 MHz) with air as exterior is shown in Fig. 3.14(a), which is fitted with a Lorentzian function and gives $\Delta\nu_m = 2.825$ MHz. Then, η, α and the quality factor are calculated to be 0.874, 8.34×10^3 m^{-1} and 196, respectively, which agree well with the reported loss characterization of polyimide [37].

Table 3.3 – Experimental results and calculations of acoustic impedances

Material	Ethanol	Water
$\Delta\nu_m$ (MHz)	6.046 ± 0.081	8.091 ± 0.159
R_P	0.6164 ± 0.0042	0.5182 ± 0.0070
r_2	0.5915 ± 0.0073	0.4373 ± 0.0099
Z_o ($\times 10^6$ kg/(m^{2}s))	0.927 ± 0.017	1.414 ± 0.027
Standard Values [1]	0.93	1.483
Mea. Error, e	0.3%	4.7%

3.5.2 Experimental results

The measurement of acoustic impedance is demonstrated by immersing the polyimide coated fiber into the sample liquids. The FSBS spectra around the resonant peak (636 MHz) for ethanol and water surroundings are shown in Fig. 3.14(b) and (c), respectively. In the presence of liquids, the resonant linewidth $\Delta\nu_m$ broadens and the peak amplitude decreases. $\Delta\nu_m$ is retrieved through Lorentzian function fitting and used to calculate R_P by using Eq. 3.38. To obtain r_2, Eq. 3.43 should be rewritten as

$$r_2^2\eta^2(R_P r_1^2 - 1) + 2\eta r_1 r_2 (R_P - 1)\cos(2\delta) + R_P - r_1^2 = 0 \tag{3.44}$$

r_2 is obtained by solving the quadratic equation Eq. 3.44 and only the positive solution is considered. The acoustic impedance of the surrounding liquid Z_o is subsequently calculated from Eq. 3.39. The experimental results and calculations are listed in Table 3.3.

The measurement results of liquid acoustic impedances have less than 5% error as compared to the standard values. Although polyimide is known to swell in the presence of water vapor, the result presented here is not affected as the humidity response time of polyimide is more than 15 minutes [89], whereas the typical measurement time using this technique is a few seconds. The presented analysis is not limited to polyimide coating and can be used in the same way for optical fiber coated with other materials as a thin layer, ideally with an acoustic impedance matching that of silica, being poorly hydrophilic and with a much reduced acoustic loss.

3.6 Distributed analysis of forward Brillouin scattering

Backward stimulated Brillouin scattering (BSBS) is widely known for enabling distributed fibre sensing. While the spatial resolution, number of resolved points and real-time sampling rate have improved greatly over the past few years, distributed Brillouin sensing is nonetheless restricted to strain and temperature measurements or their direct physical derivatives due to the confinement of longitudinal acoustic wave inside the fibre core, which is an inherent limit in diversifying the options for detected parameters. On the other hand, through the stimulated transverse acoustic waves, FSBS allows the optical waves guided in the fibre core to interact with the materials surrounding the fibre. As presented in the previous sections, FSBS had been harnessed to measure the acoustic impedance of the surrounding material. Nevertheless, all demonstrated FSBS-based sensing applications are not spatially resolved. The existing FSBS detection schemes rely on either a Sagnac interferometer loop configuration to convert nonreciprocal optical phase variations of a probing signal into changes in the optical intensity for polarised (radial) FSBS or a direct polarised light detection method for depolarised (torsional) FSBS [72]. However, both techniques result in measurements that are not spatially resolved. Since FSBS scatters light in forward direction only because of the phase matching condition, neither backscattering-based time-of-flight acquisition nor local correlation peaks can be realised directly with the FSBS scattered light, making the measurement of its local resonance spectrum a challenging and non-trivial process.

3.6.1 Concept and implementation

A technique to measure the distributed FSBS resonance spectrum of an optical fibre is presented here [22]. The principle is based on measuring the longitudinal phase evolution of a guided light that is perturbed by FSBS transverse acoustic waves. First, a long optical pulse, on which an intensity modulation is superimposed at the FSBS resonant frequency (in the radio frequency (RF) range), is used for stimulating a transverse acoustic wave in an optical fibre. Then, a reading optical pulse that is in another wavelength range and follows the FSBS activating pulse will be phase modulated by the transverse acoustic wave, thus generating multiple sidebands on the reading pulse spectrum. As the amplitude of the oscillating phase changes experienced by the reading pulse accumulates along the fibre, the intensity of each sideband changes, following the corresponding order of Bessel functions. By analysing the intensities of the sidebands, the phase changes experienced by the reading pulse can be retrieved.

Since the reading pulse sidebands are narrowly-spaced and forward propagating, a specific technique is needed to selectively measure their intensity progressions. Considering the narrow resonance linewidth and large frequency-detuning features of the BSBS process, the intensity evolutions of several reading pulse sidebands are independently selected and measured as a function of distance over a sensing fibre; this particular step is similar to Brillouin optical time-domain analysis (BOTDA). Both transversal and longitudinal acoustic waves (activated by FSBS and BSBS, respectively) are independently and distinctively used here without cross-interaction. Subsequently, the longitudinal phase evolution of the reading pulse is retrieved mathematically from the measured intensity progressions of several reading pulse sidebands. Finally, the phase evolution is numerically differentiated with respect to the longitudinal distance to obtain the local response of FSBS. The local FSBS resonance spectrum is then reconstructed by repeating the steps while detuning the FSBS activating frequency around the FSBS resonance peak. Here, distributed measurements of the FSBS resonance spectrum of a 730 m single-mode fibre (SMF) are achieved with a spatial resolution of 15 m.

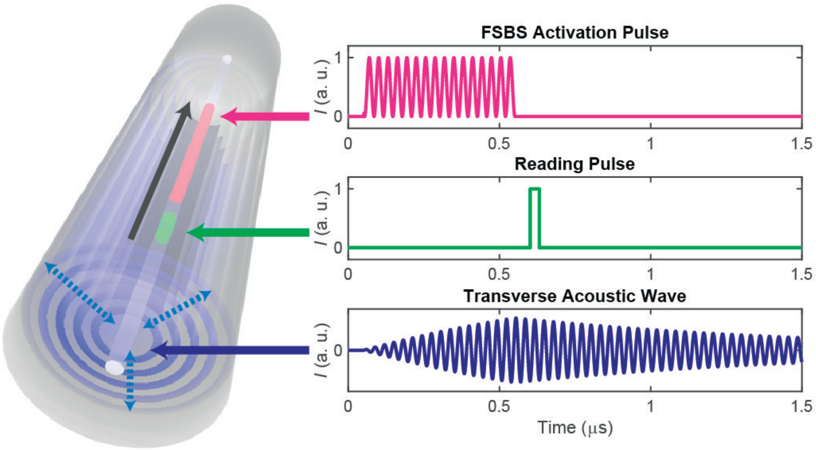

Figure 3.15 – Activation and reading of the transverse acoustic wave at an arbitrary fibre position. An intensity modulated optical pulse (magenta) stimulates a transverse acoustic wave (blue) (the oscillating period has been enlarged for illustration purpose), whose spectrum is probed by the reading pulse (green) that is time-overlapping with a short segment of the acoustic tail. The reading pulse is phase modulated by the transverse acoustic wave, thus generating multiple spectral sidebands. The longitudinal evolution of each reading pulse sideband resulting from this phase modulation is independently mapped by the process of backward stimulated Brillouin scattering.

3.6.2 Activation of the FSBS transverse acoustic wave

One of the strongest induced transverse acoustic modes, which corresponds to the 7th mode with resonant frequency $\nu_{\mathrm{res}} = 322$ MHz in standard SMF, is used for this sensing demonstration. The FSBS activating light is created by intensity modulating an incoming light with sinusoidal signal, forming a spectrum with sidebands separated by the modulation frequency ν_{F}. The beating among these spectral components inside the optical fibre stimulates the transverse acoustic mode that has a resonant frequency corresponding to ν_{F}. The intensity modulated light that activates FSBS is shaped into a long rectangular pulse to time-isolate the Kerr cross-phase modulation. This pulse is represented by the magenta trace in Fig. 3.15 and is referred to as FSBS activating pulse hereafter.

At an arbitrary fibre position z, the activated transverse acoustic wave remains oscillating locally for a certain decay time after the FSBS activating pulse passes through, as shown in the blue curve of Fig. 3.15. Through photoelastic effect, the transverse acoustic wave periodically modifies the refractive index of the fibre core at the modulation frequency ν_{F}. Considering negligible fibre loss, the peak power of the FSBS activating pulse is constant along the fibre, thus the induced refractive index change can be expressed as

$$\Delta n(\nu_{\mathrm{F}}, z, t) = a_{\mathrm{RI}}(\nu_{\mathrm{F}}, z)\cos(2\pi\nu_{\mathrm{F}} t) \tag{3.45}$$

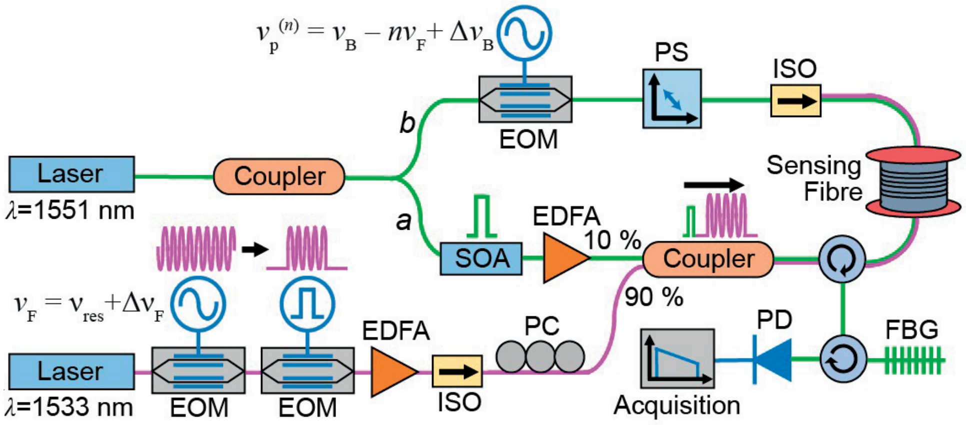

Figure 3.16 – Schematic diagram of the apparatus used to measure the spatially resolved spectrum of forward stimulated Brillouin scattering (FSBS). The FSBS activation light is represented as the magenta path (λ = 1533 nm) and the probing system based on backward stimulated Brillouin scattering (BSBS) is represented as the green path (λ = 1551 nm). The sensing fibre is 730 m-long and consists of a 30 m uncoated segment spliced between two coated segments of 500 m and 200 m respectively. The components are labelled as follows: EOM, electro-optic modulator; ISO, isolator; PC, polarisation controller; EDFA, erbium-doped fibre amplifier; SOA, semiconductor optical amplifier; PS, polarisation switch; PD, photodetector; FBG, fibre Bragg grating. The mathematical symbols are defined as follows: ν_{res}, the selected FSBS resonant frequency; ν_{F}, frequency of the intensity modulation and $\Delta\nu_{\text{F}}$, scanned frequency detuning for FSBS activation; ν_{B}, Brillouin frequency shift of BSBS; $\nu_{\text{p}}^{(n)}$, frequency of the intensity modulation and $\Delta\nu_{\text{B}}$, scanned frequency detuning for BSBS probe.

where $a_{\text{RI}}(\nu_{\text{F}}, z)$ is the amplitude of the refractive index changes and represents the spectrum of the selected FSBS resonance mode at position z, from which the local acoustic impedances of the external materials are eventually retrieved.

The experimental configuration related to the FSBS activating process is illustrated in the magenta path shown in Fig. 3.16. The continuous wave (CW) light from a distributed feedback (DFB) laser at 1533 nm is intensity modulated with sinusoidal signal at the selected FSBS resonant frequency ($\nu_{\text{res}} = 322$ MHz) using an electro-optic modulator (EOM), followed by shaping the modulated light into a ~500 ns rectangular pulse using another EOM. Approximately 160 periods of the intensity modulation are contained within this long pulse. The FSBS activating pulse is amplified by a high power erbium-doped fibre amplifier (EDFA) to reach a peak power of ~35 dBm so that the generated transverse acoustic wave is sufficiently strong for the subsequent reading process. To obtain the spectral profile of $a_{\text{RI}}(\nu_{\text{F}}, z)$, the modulation frequency ν_{F} is detuned around the FSBS resonant frequency ν_{res} and is expressed as $\nu_{\text{F}} = \nu_{\text{res}} + \Delta\nu_{\text{F}}$ (the scanned frequency detuning $\Delta\nu_{\text{F}}$ is from -7 MHz up to 7 MHz, resulting in ν_{F} ranging from 315 MHz up to 329 MHz with an incremental step of 0.1 MHz).

3.6.3 Reading the FSBS-induced phase modulation

The induced refractive index changes represented by Eq. 3.45 can be probed with a guided probing light that propagates in the same direction as the FSBS activation pulse but in a different wavelength region, so that the FSBS activating and reading (probing) processes are optically isolated. To provide time-of-flight distributed measurements of the FSBS-induced refractive index changes, this probing light is shaped into a short pulse (see dark green trace in Fig. 3.15), and is mentioned as the reading pulse. The optical field of the reading pulse can be expressed as

$$E(z_\mathrm{r},t) = A(z_\mathrm{r},t)\exp[j(k_\mathrm{z} z_\mathrm{r} - \omega_0 t + \phi_0 + \Delta\phi)] \tag{3.46}$$

where ϕ_0 is the initial phase, $\Delta\phi$ is the phase shift due to the transverse acoustic wave, $A(z_\mathrm{r},t)$ is the spatio-temporal profile of the reading pulse, ω_0 is the optical carrier frequency, z_r is the position of the reading pulse in the fibre, k_z is the axial optical wave-vector $k_\mathrm{z} \approx 2\pi n_\mathrm{eff}/\lambda$, and λ is the optical wavelength. Since the longitudinally phase velocity of the transverse acoustic wave is equal to the group velocity of the guided light, this reading pulse will follow the same acoustic phase along the fibre, therefore each temporal point of the reading pulse experiences the induced refractive index change associated to the respective overlapping point with the transverse acoustic waveform. In other words, the transverse acoustic waveform is imprinted on the reading pulse as time-dependent phase shifts $\Delta\phi$. This scenario is equivalent to the reading pulse being phase modulated by the transverse acoustic wave inside the fibre. Considering that the reading pulse duration is much longer than the period of the FSBS phase modulation, the phase shift $\Delta\phi$ is given by

$$\begin{aligned} \Delta\phi(\nu_\mathrm{F},z_\mathrm{r},t) &= \frac{2\pi}{\lambda}\int_0^{z_\mathrm{r}} \Delta n(\nu_\mathrm{F},z_\mathrm{r},t)\,dz \\ &= \frac{2\pi}{\lambda}\cos(2\pi\nu_\mathrm{F} t)\int_0^{z_\mathrm{r}} a_\mathrm{RI}(\nu_\mathrm{F},z)\,dz \end{aligned} \tag{3.47}$$

The reading pulse undergoes a phase shift $\Delta\phi$ that accumulates over distance as it propagates along the fibre. For simplicity, a term called phase factor is defined

$$\xi(\nu_\mathrm{F},z_\mathrm{r}) = \frac{2\pi}{\lambda}\int_0^{z_\mathrm{r}} a_\mathrm{RI}(\nu_\mathrm{F},z)\,dz \tag{3.48}$$

which represents the amplitude of the integrated phase shift experienced by the reading pulse as it reaches the position z_r in the fibre. Thus, the amplitude of local refractive index change $a_\mathrm{RI}(\nu_\mathrm{F},z)$ can be recovered through differentiation. By combining Eq. 3.46 to Eq. 3.48, the optical field can be written as

$$E(\nu_\mathrm{F},z_\mathrm{r},t) = A(z_\mathrm{r},t)\exp[j(k_\mathrm{z} z_\mathrm{r} - \omega_0 t + \phi_0)]\exp[j\xi(\nu_\mathrm{F},z_\mathrm{r})\cos(2\pi\nu_\mathrm{F} t)] \tag{3.49}$$

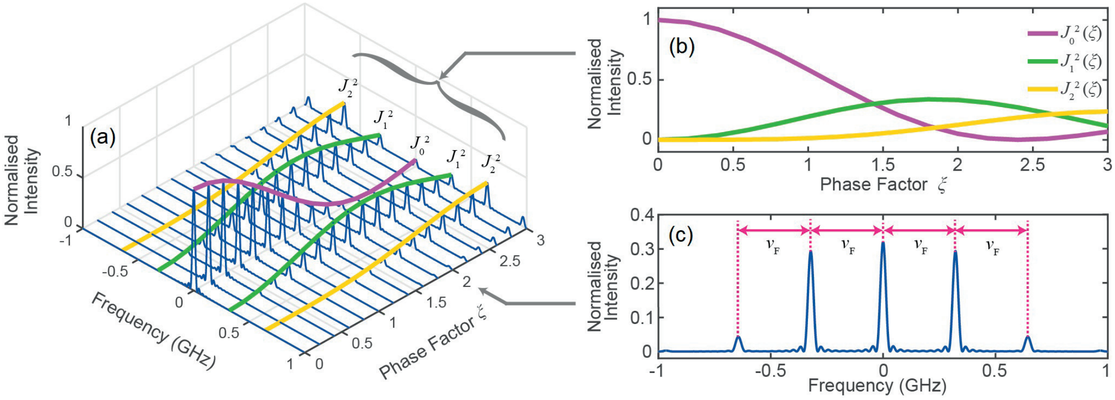

Figure 3.17 – Simulated longitudinal evolution of the reading pulse spectrum. (a) The reading pulse spectrum changes along the fibre as it is being phase modulated by the transverse acoustic wave of forward stimulated Brillouin scattering (FSBS). (For illustration purpose, the fibre surroundings is assumed to be uniform along the fibre, i.e., the phase factor $\xi(\nu_F, z_r)$ increases linearly with respect to the reading pulse location z_r. The spectrum is normalised by the input intensity of the reading pulse at its central frequency.) (b) The intensity progression of the 0th, 1st and 2nd order spectral sidebands (each one proportional to J_0^2, J_1^2 and J_2^2, respectively) of the reading pulse as a function of the z_r-dependent phase factor $\xi(\nu_F, z_r)$. (c) The reading pulse spectrum at an arbitrary position. Note that the local spectral sidebands are separated by the modulation frequency of FSBS activation ν_F.

The second exponential term of Eq. 3.49 can be expanded via Jacobi-Anger identity :

$$\begin{aligned} E(\nu_F, z_r, t) &= A(z_r, t)\exp[j(k_z z_r - \omega_0 t + \phi_0)]\left[\sum_{n=-\infty}^{\infty} j^n J_n(\xi(\nu_F, z_r))\exp(jn\Omega_F t)\right] \\ &= A(z_r, t)\exp[j(k_z z_r + \phi_0)]\left[\sum_{n=-\infty}^{\infty} j^n J_n(\xi(\nu_F, z_r))\exp(-j(\omega_0 - n\Omega_F)t)\right] \end{aligned} \tag{3.50}$$

where $\Omega_F = 2\pi\nu_F$. Equation 3.50 indicates that the spectrum of the reading pulse consists of spectral sidebands that are offset from the optical carrier frequency to multiples of the modulation frequency $\omega_0 \pm n\Omega_F$. The intensity progression associated to the nth order spectral sideband $I_r^{(n)} = E_{(n)}E_{(n)}^*$, is proportional to the square of the ordinary Bessel function of order n, $J_n^2(\xi)$ (see Fig. 3.17). By knowing the local intensities of the reading pulse sidebands, the phase factor $\xi(\nu_F, z_r)$ can be calculated mathematically.

The impact of Kerr effect on the measurement is avoided by delaying the reading pulse after the FSBS activating pulse. This way, the reading pulse interacts only with the tail of the FSBS transverse acoustic wave (blue trace in Fig. 3.15), which is free from the Kerr-induced distortions. The experimental setup related to the reading pulse is shown in the green path *a* in Fig. 3.16. Light from a DFB laser at 1551 nm is split into two paths to create counter-propagating pump and probe lights for BOTDA measurements (discussed in the next section). The reading pulse, which is also the pump pulse for the BOTDA system, is created by shaping the incoming light into a 30 ns high-extinction ratio pulse using a semiconductor optical amplifier (SOA). The reading pulse is then injected into the sensing fibre through a 90:10 coupler and synchronized by instruments to propagate with a 10 ns delay after the FSBS activating pulse.

3.6.4 Intensity progression of the reading pulse sidebands

To obtain the longitudinal phase evolution, the intensity progressions $I_{\mathrm{r}}^{(n)}(z_{\mathrm{r}})$ of a few reading pulse sidebands have to be individually measured (see the next section for further details). BSBS is exploited for this measurement since the linewidth of the Brillouin gain spectrum (BGS) (30 MHz) is much narrower than the separation between reading pulse sidebands ν_{F}. Through BSBS, the pump wave transfers energy proportional to its intensity to a counter-propagating probe wave that is red-shifted by the Brillouin frequency shift (BFS) ($\nu_{\mathrm{B}} \approx$10.86 GHz in standard optical fibre). As the frequency difference between one of the reading pulse sidebands and the probe wave is equal to the BFS, the sideband under interrogation will map its intensity variation efficiently to the probe wave during propagation in the fibre.

The BSBS measurement technique used here to retrieve $I_{\mathrm{r}}^{(n)}(z_{\mathrm{r}})$ is similar to BOTDA. The individual sideband of the reading pulse acts as the pump pulse for the BOTDA system whereas the CW probe wave is created by intensity modulating the incoming light with a sinusoidal signal at frequency $\nu_{\mathrm{p}}^{(n)} = \nu_{\mathrm{B}} - n\nu_{\mathrm{F}}$ using an EOM (see green path *b* of Fig. 3.16), so that the probe frequency coincides with the BGS peak of the nth order reading pulse sideband. Since the CW probe wave and the FSBS activating pulse are counter-propagating, the refractive index perturbation induced on the probe wave averages to zero, thus the probe wave is independent from the FSBS activation process. Nevertheless, the BFS in reality is not uniform along the fibre due to the inherent material inhomogeneity, external temperature perturbations and strain variations, which would affect the precise measurement of the sideband intensity progression. To overcome this problem, the peak gain of the BGS has to be determined by detuning $\nu_{\mathrm{p}}^{(n)}$ around the BFS, $\nu_{\mathrm{p}}^{(n)} = \nu_{\mathrm{B}} - n\nu_{\mathrm{F}} + \Delta\nu_{\mathrm{B}}$ (the frequency detuning $\Delta\nu_{\mathrm{B}}$ is from -25 MHz to 25 MHz). Then, a quadratic fitting is applied to the local BGS to obtain the peak gain, which proportionally represents the local intensity of the interrogated reading pulse sideband. Here, the BGS scanning to obtain $I_{\mathrm{r}}^{(0)}(z_{\mathrm{r}})$ is repeated for all detuned frequencies $\Delta\nu_{\mathrm{F}}$ around the FSBS resonant frequency ν_{res} and again repeated for other two higher-order sidebands,$I_{\mathrm{r}}^{(1)}(z_{\mathrm{r}})$ and $I_{\mathrm{r}}^{(2)}(z_{\mathrm{r}})$; the results are shown in Fig. 3.18.

3.6.5 Phase factor recovery and data processing

The intensity progression of *n*th order reading pulse spectral sideband $I_{\mathrm{r}}^{(n)}(z_{\mathrm{r}})$ is a function of phase factor $\xi(\nu_{\mathrm{F}}, z_{\mathrm{r}})$ and is proportional to $J_n^2(\xi(\nu_{\mathrm{F}}, z_{\mathrm{r}})$, written as $I_{\mathrm{r}}^{(n)}(z_{\mathrm{r}}) = I_{\mathrm{r}}^{(n)}(\xi(\nu_{\mathrm{F}}, z_{\mathrm{r}})) = \kappa J_n^2(\xi(\nu_{\mathrm{F}}, z_{\mathrm{r}}))$. In principle, to retrieve $\xi(\nu_{\mathrm{F}}, z_{\mathrm{r}})$, the inverse function of $I_{\mathrm{r}}^{(n)}(\xi(\nu_{\mathrm{F}}, z_{\mathrm{r}}))$ has to be determined. Although the non-invertible functions $J_n^2(\xi(\nu_{\mathrm{F}}, z_{\mathrm{r}}))$ can be made invertible by limiting the domain and range to the regions that are injective, using a single sideband to measure $\xi(\nu_{\mathrm{F}}, z_{\mathrm{r}})$ is nevertheless unreliable because the longitudinal intensity progression

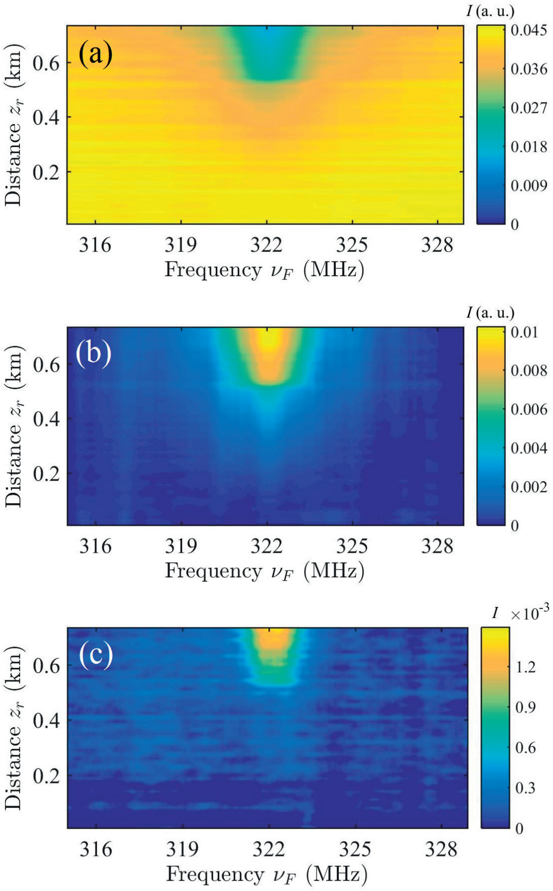

Figure 3.18 – Measured intensity progressions of the reading pulse sidebands. Intensity $I_{\mathrm{r}}^{(n)}(\nu_{\mathrm{F}}, z_{\mathrm{r}})$ of the (a) 0th, (b) 1st and (c) 2nd order reading pulse sidebands (each one is proportional to J_0^2, J_1^2 and J_2^2, respectively), measured at each scanning frequency ν_{F} (detuned within $\Delta\nu_{\mathrm{F}}$ around ν_{res}). Experimental results are obtained when the 30 m uncoated fibre segment is exposed to air.

can be easily affected by external perturbations, such as fibre bending or local losses. A more robust approach, which avoids the detrimental impact of local losses, is using the recurrence properties of Bessel functions to recover $\xi(\nu_{\mathrm{F}}, z_{\mathrm{r}})$. In particular, a simple form of the Bessel recurrence relation is given as

$$J_{(n-1)}(\xi(\nu_{\mathrm{F}}, z_{\mathrm{r}})) + J_{(n+1)}(\xi(\nu_{\mathrm{F}}, z_{\mathrm{r}})) = \frac{2n}{\xi(\nu_{\mathrm{F}}, z_{\mathrm{r}})} J_{(n)}(\xi(\nu_{\mathrm{F}}, z_{\mathrm{r}})) \tag{3.51}$$

where n is the Bessel function order. Using Eq. 3.51, $\xi(\nu_{\mathrm{F}}, z_{\mathrm{r}})$ can be reliably determined from the intensities of three consecutive orders of spectral sidebands. Here, the 0th, 1st and 2nd order sidebands are selected to maximize the signal-to-noise ratio (SNR) of the measurements as they have the highest intensities as compared to the other higher-order sidebands. $\xi(\nu_{\mathrm{F}}, z_{\mathrm{r}})$ is obtained from Eq. 3.51 with $n = 1$, and is related to the measured intensities of the sidebands

$I_{\mathrm{r}}^{(n)}(\xi(\nu_{\mathrm{F}}, z_{\mathrm{r}}))$, as given below

$$\begin{aligned}
\xi(\nu_{\mathrm{F}}, z_{\mathrm{r}}) &= 2\left(\frac{J_1(\xi(\nu_{\mathrm{F}}, z_{\mathrm{r}}))}{J_0(\xi(\nu_{\mathrm{F}}, z_{\mathrm{r}})) + J_2(\xi(\nu_{\mathrm{F}}, z_{\mathrm{r}}))}\right) \\
&= 2\left(\frac{\sqrt{I_{\mathrm{r}}^{(1)}(\xi(\nu_{\mathrm{F}}, z_{\mathrm{r}}))}}{\sqrt{I_{\mathrm{r}}^{(0)}(\xi(\nu_{\mathrm{F}}, z_{\mathrm{r}}))} + \sqrt{I_{\mathrm{r}}^{(2)}(\xi(\nu_{\mathrm{F}}, z_{\mathrm{r}}))}}\right) \text{ for } 0 \le \xi(\nu_{\mathrm{F}}, z_{\mathrm{r}}) \le 2.4048
\end{aligned} \tag{3.52}$$

Note that all $I_{\mathrm{r}}^{(n)}(\xi(\nu_{\mathrm{F}}, z_{\mathrm{r}}))$ in the numerator and denominator of Eq. 3.52 are of the same degree, thus any power loss affecting the reading pulse, which scales all $I_{\mathrm{r}}^{(n)}(\xi(\nu_{\mathrm{F}}, z_{\mathrm{r}}))$ equally, does not change $\xi(\nu_{\mathrm{F}}, z_{\mathrm{r}})$. Since Eq. 3.52 involves taking the square root of $I_{\mathrm{r}}^{(n)}(\xi(\nu_{\mathrm{F}}, z_{\mathrm{r}}))$, the signs of $J_n(\xi(\nu_{\mathrm{F}}, z_{\mathrm{r}}))$ cannot be recovered, which restricts the equation's validity to the regions where $J_0(\xi(\nu_{\mathrm{F}}, z_{\mathrm{r}}))$, $J_1(\xi(\nu_{\mathrm{F}}, z_{\mathrm{r}}))$ and $J_2(\xi(\nu_{\mathrm{F}}, z_{\mathrm{r}}))$ are positives. To overcome this problem, the operation is limited to the first valid region, which begins at $\xi(\nu_{\mathrm{F}}, z_{\mathrm{r}}) = 0$ and ends at the first zero of $J_{(0)}(\xi(\nu_{\mathrm{F}}, z_{\mathrm{r}}))$, i.e., $\xi(\nu_{\mathrm{F}}, z_{\mathrm{r}}) = 2.4048$. In practice, the intensity of the FSBS activating pulse, which affects the phase factor $\xi(\nu_{\mathrm{F}}, z_{\mathrm{r}})$, is controlled carefully so that $I_{\mathrm{r}}^{(0)}(\xi(\nu_{\mathrm{F}}, z_{\mathrm{r}}))$ does not exceed the first minimum at the end of the fibre and $\xi(\nu_{\mathrm{F}}, z_{\mathrm{r}})$ remains in the valid region. Nevertheless, it must be mentioned that limiting $\xi(\nu_{\mathrm{F}}, z_{\mathrm{r}})$ is a simplified solution for demonstration purpose. Extending the calculation to all regions is possible as $\xi(\nu_{\mathrm{F}}, z_{\mathrm{r}})$ is a monotonic function, which implies the changes of signs for $J_n(\xi(\nu_{\mathrm{F}}, z_{\mathrm{r}}))$ follow a definite sequence, thus allowing $\xi(\nu_{\mathrm{F}}, z_{\mathrm{r}})$ to be retrieved successively along the distance according to the progress of $\xi(\nu_{\mathrm{F}}, z_{\mathrm{r}})$.

The measurement results of $I_{\mathrm{r}}^{(n)}(z_{\mathrm{r}}))$ as shown in Fig. 3.18 are stored in a computer and processed trace by trace for each scanning frequency ν_{F} within the measurement range. To describe the data processing steps, only the traces measured at the FSBS resonant frequency ν_{res} are detailed. $I_{\mathrm{r}}^{(n)}(z_{\mathrm{r}}))$ of the 0th, 1st and 2nd order spectral sidebands are plotted in Fig. 3.19(a). $\xi(z_{\mathrm{r}})$ is obtained by applying Eq. 3.52 pointwise at each location z_{r}, the result is shown in Fig. 3.19(b). The retrieved $\xi(z_{\mathrm{r}})$ is a linearly increasing trace with a steep slope at the air-exposed region where $\xi(z_{\mathrm{r}})$ increases faster due to the larger FSBS induced local refractive index change. In the initial part of the optical fibre, where $\xi(z_{\mathrm{r}})$ is the lowest, $J_0^2(\xi(z_{\mathrm{r}}))$ is the highest while $J_1^2(\xi(z_{\mathrm{r}}))$ and $J_2^2(\xi(z_{\mathrm{r}}))$ are the lowest (see Fig. 3.17(b)). This indicates that the SNR for $\xi(z_{\mathrm{r}})$ deduced from Eq. 3.52 is dominated by $J_1^2(\xi(z_{\mathrm{r}}))$ and thus the SNR at the beginning of the retrieved $\xi(z_{\mathrm{r}})$ is always low (see Fig. 3.19(b)).

The local response of FSBS is represented by $a_{\mathrm{RI}}(\nu_{\mathrm{F}}, z)$. From Eq. 3.48, $a_{\mathrm{RI}}(\nu_{\mathrm{F}}, z_{\mathrm{r}})$ is determined from the differentiation of the phase factor $\xi(z_{\mathrm{r}})$. To mitigate the impact of the measurement noise on the numerical differentiation, the process begins by segmenting the data points of $\xi(z_{\mathrm{r}})$ into lengths of Δz and calculating the average value $\langle\xi(z_{\mathrm{r}})\rangle$ for the respective segment. Δz defines the final spatial resolution, which is set as 15 m in this experiment to achieve a good balance between the number of resolved points and the SNR. Based on Eq. 3.48,

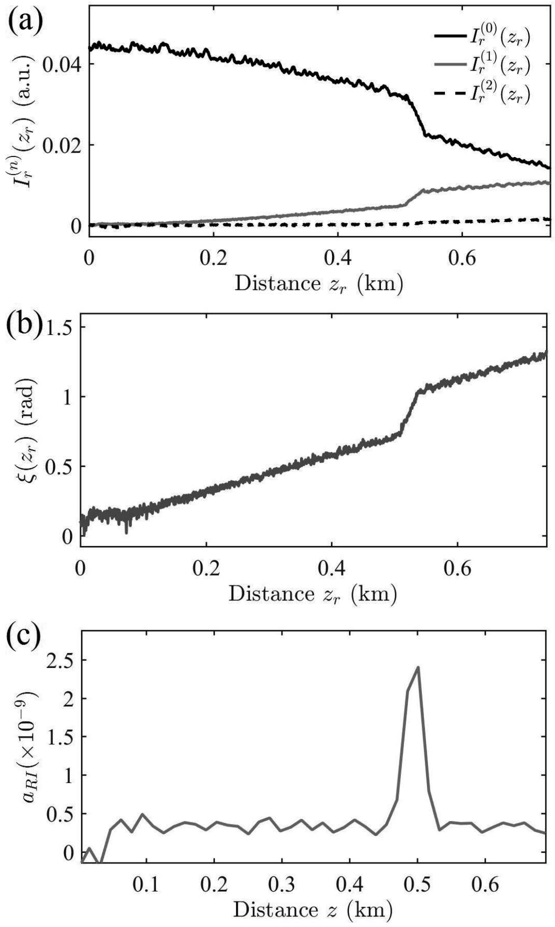

Figure 3.19 – Data processing steps to obtain the local response of forward stimulated Brillouin scattering. (a) The measured intensity $I_{\mathrm{r}}^{(n)}(z_{\mathrm{r}})$ of the 0th, 1st and 2nd order spectral sidebands versus distance z_{r}, obtained at the FSBS peak resonant frequency ν_{res}. (b) Phase factor $\xi(z_{\mathrm{r}})$ retrieved by using the Bessel recurrence relation in Eq. 3.52. (c) The local amplitude of refractive index changes $a_{\mathrm{RI}}(z)$ (unitless) that is obtained by using segmental differentiation.

$a_{\mathrm{RI}}(\nu_{\mathrm{F}}, z)$ can be retrieved via numerical differentiation

$$a_{\mathrm{RI}}(z) = \frac{\lambda}{2\pi} \frac{\langle \xi(z_{\mathrm{r}}) \rangle - \langle \xi(z_{\mathrm{r}} - \Delta z) \rangle}{\Delta z} \tag{3.53}$$

The retrieved $a_{\mathrm{RI}}(\nu_{\mathrm{F}}, z)$ is shown in Fig. 3.19(c). The noise source of $a_{\mathrm{RI}}(\nu_{\mathrm{F}}, z)$ is mainly attributed to the inhomogeneity of the BGS peak amplitude that could arise from several factors including strain variations along the optical fibre due to coiling and an imperfect compensation of the BSBS probe light polarization fading in the traces.

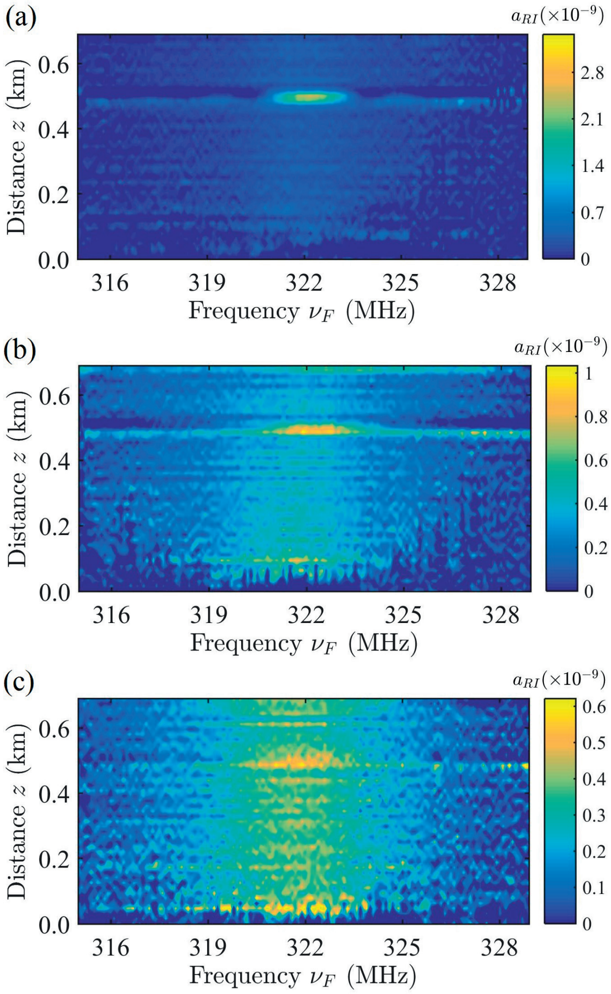

Figure 3.20 – Distributed spectra of forward stimulated Brillouin scattering (FSBS) measured over the 730 m-long sensing fibre when the 30 m uncoated fibre segment is exposed to (a) air, (b) ethanol and (c) water. The FSBS responses represented by the local amplitudes of refractive index changes a_{RI} (unitless) could be clearly observed in the exposed fibre regions (0.5 km).

3.6.6 Experimental results

Local acoustic impedance sensing is demonstrated by placing the 30 m uncoated optical fibre segment in three different outer environments (air, ethanol and water). The distributed FSBS spectra of the 730 m sensing fibre with air, ethanol and water exposures are shown in Fig. 3.20. The exposed region could be clearly identified in the FSBS distributed spectra maps because of the strong resonance from the efficient transverse acoustic wave reflection at the fibre boundary especially when exposed to air. The rest of the sensing fibre keeps its original acrylate coating, which reduces significantly the acoustic wave reflection. The local FSBS spectral response in the coated segments can be nevertheless observed, though with a much reduced amplitude contrast.

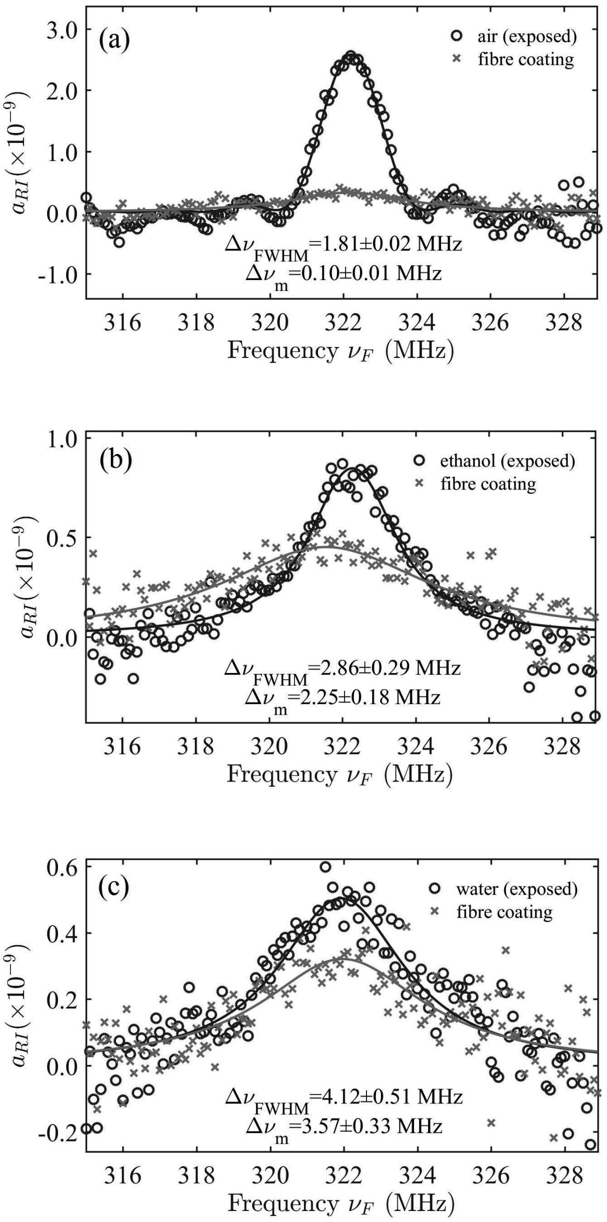

Figure 3.21 – The spectra of forward stimulated Brillouin scattering (FSBS) measured at a given fibre position inside the 30 m fibre segment exposed to (a) air, (b) ethanol and (c) water. The FSBS spectra measured at an arbitrary position in the normal coated fibre segment (with acrylate polymer coating) are plotted alongside for comparison. $\Delta\nu_{\mathrm{FWHM}}$ is the full width at half maximum (FWHM) of the measured spectrum at the sensing point (convolution of the pulse spectrum and FSBS resonance spectrum) and $\Delta\nu_{\mathrm{m}}$ is the recovered original linewidth of FSBS resonance at the corresponding position.

The FSBS resonance spectra at the exposed fibre segment are shown in Fig. 3.21. In the presence of different outer media, the FSBS resonance linewidth changes in an inverse proportion to the resonance peak intensity; i.e. as the resonance linewidth broadens, the resonance peak intensity decreases. The FSBS spectrum of the normal uncoated fibre segment with acrylate polymer coating are plotted alongside as reference for comparison. The FSBS resonance linewidth of each liquid sample is related to the acoustic impedances Z_o of the outer material and Z_f of the fibre material by Eq. 3.38.

The intrinsic acoustic loss defining $\Delta\nu_\mathrm{s}$ is estimated from the resonance linewidth when the uncoated fibre section is exposed to air. Under this condition the acoustic reflection at the optical fibre boundary is nearly perfect becasue of the large acoustic impedance mismatch. The intrinsic linewidth $\Delta\nu_\mathrm{s}$ is considered in this case as solely due to the bulk viscous damping of silica (~100 kHz) [46, 86]. The measured full width at half maximum (FWHM) $\Delta\nu_\mathrm{FWHM}$ of the FSBS resonance spectrum for air, ethanol and water are respectively 1.81 ± 0.02 MHz, 2.86 ± 0.29 MHz and 4.12 ± 0.51 MHz. However, because of the finite duration of the FSBS activating pulse, the measured FSBS spectrum is a convolution of the power spectrum of the FSBS activating pulse (described as a sinc function because it is obtained from the Fourier transform of the temporal rectangular pulse function) and the power spectrum of the original FSBS resonance (described as a Lorentzian function). The mathematical expression of the power spectrum of the FSBS activating pulse is

$$S_\mathrm{p}(\nu) = T\,\mathrm{sinc}^2(T\nu) \tag{3.54}$$

where ν and T are the frequency and the pulse duration, respectively. The power spectrum of the FSBS activating pulse is integrated to unity, $\int_{-\infty}^{+\infty} S_\mathrm{p}(\nu)\,\mathrm{d}\nu = 1$. The mathematical expression of the power spectrum of the FSBS resonance is

$$g_\mathrm{B} = g_0 \frac{\Gamma^2}{\Gamma^2 + \Omega^2} \tag{3.55}$$

where Ω is the angular frequency, $\Omega = 2\pi\nu$. g_0 is the maximum FSBS gain, $\Gamma = \Gamma_\mathrm{B}/2$ is the half width at half maximum (HWHM) of the original FSBS resonance spectrum in angular frequency, Γ_B is the FWHM, which is given by $\Gamma_\mathrm{B} = 2\pi\Delta\nu_\mathrm{m}$ and $\Delta\nu_\mathrm{m}$ is the original FSBS resonance linewidth. The convolution can be described by a full analytical expression for a given activating pulse duration [5]:

$$S_\mathrm{conv}(\Omega) = g_\mathrm{B}(\Omega)\left(1 - \frac{(\Gamma^2 - \Omega^2)(1 - e^{-\Gamma T}\cos(T\Omega)) + 2\Gamma\Omega e^{-\Gamma T}\sin(T\Omega)}{\Gamma T(\Gamma^2 + \Omega^2)}\right) \tag{3.56}$$

The finite duration of the FSBS activating pulse causes the broadening of the measured local FSBS resonance spectrum, which is simulated and shown in Fig. 3.22(a) using both numerical and analytical approaches. For the analytical approach, the spectrum of convolution is calculated directly using Eq. 3.56 while for the numerical approach, the spectrum of the convolution is obtained by applying *conv* function in Matlab to the power spectra dataset of both the rectangular shape pulse and the Lorentzian shape resonance.

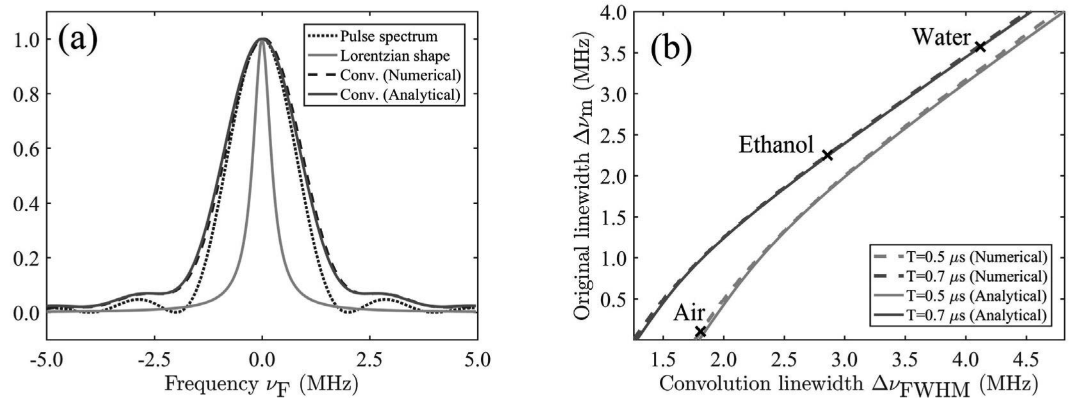

Figure 3.22 – Broadening of the measured FSBS resonance linewidth caused by the finite duration of FSBS activating pulse. (a) The convolution of the pulse spectrum and the Lorentzian shape FSBS resonance spectrum simulated via numerical approach (using *conv* function in Matlab) and analytical approach (using Eq. 3.56). The Lorentzian linewidth $\Delta\nu_\text{m}$ and the pulse duration T are arbitrarily set as 0.5 MHz and 0.5 μs, respectively. (b) The original FSBS resonance linewidth $\Delta\nu_\text{m}$ recovered from the FWHM of the measured spectrum of the convolution $\Delta\nu_\text{FWHM}$ for two different FSBS activating pulse durations, $T = 0.5$ μs and $T = 0.7$ μs. Both numerical and analytical approaches are plotted, they give the same $\Delta\nu_\text{m}$. The points corresponds to the measurement results of air, ethanol and water surroundings as in Fig. 3.21 are marked by crosses.

To obtain the original FSBS resonance linewidth $\Delta\nu_\text{m}$, the experimentally obtained local FSBS resonance spectrum is fitted to Eq. 3.56 with prior knowledge of the pulse duration T from the instrument settings. The pulse duration T is adjusted judiciously to optimize the detected signal strength. Decreasing T would lead to a broader FSBS resonance spectrum and lower resonance peak intensity [5] whereas increasing T would decrease the overall optical power gain of the pulse because of EDFA gain saturation, which results in weaker generated transverse acoustic waves. In this experiment, the pulse duration for the initial intrinsic loss calibration (when the fibre is surrounded by air) is adjusted to 0.5 μs. For the measurement of liquid acoustic impedance, it is increased to 0.7 μs to improve the detected signal gain because the peak intensity of the original FSBS resonance is about 5 times lower in liquid than in air. From the curve fitting, the value of Γ can be retrieved, which is used directly to calculate the value of $\Delta\nu_\text{m}$. A more direct approach to obtain $\Delta\nu_\text{m}$ is through finding the mathematical expression of the original FSBS resonance linewidth $\Delta\nu_\text{m}$ from the linewidth of convolution $\Delta\nu_\text{FWHM}$ (the linewidth obtained directly from the measured resonance spectrum) and the pulse duration T, this has been derived in [5]. The linewidth of convolution spectrum $\Delta\nu_\text{FWHM}$ is related to the linewidth of the original FSBS resonance spectrum $\Delta\nu_\text{m}$ by a broadening factor BF, $\Delta\nu_\text{FWHM} = BF \times \Delta\nu_\text{m}$. BF is given by [5]

$$BF = \sqrt{\frac{2 + \sqrt{4 + \psi^2}}{\psi}} \tag{3.57}$$

where $\psi = \Gamma T - 1 + e^{-\Gamma T}$. This expression is plotted in Fig. 3.22(b) alongside the numerical approach for comparison, the value of $\Delta\nu_\mathrm{m}$ obtained through both approaches are identical. The points that corresponds to $\Delta\nu_\mathrm{FWHM}$ from the results plotted in Fig. 3.21 are marked with crosses, from which $\Delta\nu_\mathrm{m}$ can be retrieved, the values are the same as compared to the curve fitting approach.

The original FSBS resonance linewidth $\Delta\nu_\mathrm{m}$ successfully retrieved from the fittings are 0.10 ± 0.01 MHz, 2.25 ± 0.18 MHz and 3.57 ± 0.33 MHz for air, ethanol and water exposures, respectively. For the case of air, the spectral response is nearly entirely given by the pulse spectrum. Since according to references the intrinsic linewidth due to bulk viscous damping of silica $\Delta\nu_\mathrm{s}$ is about 0.1 MHz [46, 86] and this value is compatible with the retrieved $\Delta\nu_\mathrm{s}$ from the measurement result, this value is used in the rest of the calculations. The corresponding acoustic impedances of the outer materials at the exposed fibre segment are then calculated based on Eq. 3.38, resulting in $1.49 \pm 0.13 \times 10^6$ kg m^{-2}s^{-1} for water, and $0.93 \pm 0.07 \times 10^6$ kg m^{-2}s^{-1} for ethanol. These results agree well with the reported standard values [1]. The measurement uncertainty of acoustic impedance is evaluated from the standard deviation of $\Delta\nu_\mathrm{m}$ fitting and calculated using standard error propagations as discussed in section 3.4.

3.6.7 Discussion

A technique is demonstrated to measure the distributed FSBS spectrum and retrieve the local acoustic impedance of the surrounding materials. In particular, the acoustic impedances of water and ethanol obtained by this technique agree well with the reported standard values. Experimental results prove that the distributed acoustic impedance measurements of a material are possible using the FSBS opto-acoustic interaction without direct interaction between light and the external material, which brings crucial advantages in terms of reliability and ease of implementation. The achieved spatial resolution $\Delta z = 15$ m is determined by the length of averaging segment in numerical differentiation. It is set to balance between the number of resolved points and the noise of differentiation. Further developments aiming at reducing the noise sources, in particular the amplitude fluctuation of BGS peak along the fibre, could improve the spatial resolution down to the reading pulse width.

The stripping of the fibre acrylate coating here is to simplify the acoustic impedance analysis so that the focus - distributed FSBS spectrum measurement could be emphasised. This technique operates with similar performance using optical fibres coated with a thin layer of polymer, e.g. polyimide. Thin polymer coating allows the transverse acoustic waves to penetrate with lower acoustic damping while maintains the same mechanical strength of fibre as the standard coated fibre as described in the previous section. In addition, this technique could be deployed to characterise local FSBS spectrum inside a waveguide, thus having potential applications not only in sensing but also in quality control of hybrid photonic-phononic waveguide fabrication, where the overall acoustic gain response is sensitive to small variations in the local waveguide geometry.

Conclusions

This thesis explores different classes of guided acoustic waves in optical fibres through Brillouin scatterings, emphasising on locating the acoustic resonances inside the optical fibres. The ability to analyse Brillouin scatterings in distributed fashion provides a powerful tool for non-invasive study of waveguide structures as well as opening new classes of fibre sensing technology, the benefits and prospects are numerous. In this thesis, the disparate Brillouin scattering classes with several variants of theoretical expressions are harmonised and described with a common set of physics principles which include the conservation of momentum and energy, elastic waves propagation and photoelastic effects. Based on these principles, different classes of Brillouin scatterings had been analysed separately by considering their respective optical and acoustic guiding conditions.

The mapping of Brillouin scatterings along a microfibre as demonstrated in chapter 2 establishes a unique way of obtaining the dimension of a sub-wavelength waveguide without resorting to conventional microscopy (e.g. scanning electron microscope (SEM)), which has damaging effects on the microfibre in most cases because of the preparation process for sample viewing. For the microfibre of diameter ~1 μm, its Brillouin spectrum is highly sensitive to small change in size, a mere 0.1 μm change in the radius of the microfibre can result in ~70 MHz shift in one of the main Brillouin resonance peaks. Moreover, all Brillouin resonance frequencies shift with different amount and signs as the size changes, therefore this study could possibly provide a way to isolate the effects of temperature and strain in characterising the size of a tiny waveguide. Apart from this, the phase-modulated counter-propagating pump and probe interrogation technique used in the position scanning of Brillouin spectrum essentially enables the surface acoustic wave (and the other Brillouin resonances) to be locally stimulated at any desired position, this could possibly be used as a random access type sensor to monitor the surface coating thickness, defects or the presence of condensates.

Nevertheless, the more elemental study of distributed Brillouin scatterings in microfibre with pump and probe technique remains an ongoing research area. Because of the random states of light polarisation inside the microfibre, the stimulation of acoustic waves at certain fibre locations are ineffective, common techniques that overcome this problem include scrambling the polarisation or through multiple fast polarisation switching and averaging. However, these practices prevent the study of torsional (asymmetric) acoustic modes, for which a certain polarisation state should be ensured and maintained in the fibre to effectively stimulate the torsional mode. Besides, an interesting effect - Brillouin scattering self-cancellation [32] (the electrostrictive force is canceled by radiation pressure at the silica microfibre boundary) is not observed with the pump and probe experiment in this work despite reported by a previous work. This is probably because the diameter range for this ephemeral phenomenon is very small (from ~1.05 μm to ~1.15 μm). To achieve such level of accuracy in microfibre diameter, the measurement has to be carried out during the fabrication process. Further study could be extended to improve and clarify these areas.

The study of forward stimulated Brillouin scattering (FSBS) in the standard singe-mode fibre (SMF) builds on a new class of optical fibre sensor that could detect the acoustic impedance of the fibre's external material. Particularly, this thesis presents a novel technique to position-resolve the FSBS spectrum along a fibre, from which the acoustic impedance of the surrounding liquid at a certain position can be retrieved. This unfolds several potential applications such as mapping the particle concentration or density of water along a river for environment protection, especially using it to probe deep water body where satellite images are unavailable. As such, this technique represents a yardstick in the domain of distributed Brillouin fibre sensing as almost all existing Brillouin fibre sensors rely on the axial propagating acoustic wave which are restricted by the available sensing parameters (temperature and strain) and hence limit their pervasiveness in field applications. Besides, the same distributed FSBS analysis technique can be easily developed into a new tool for fibre quality control such as measuring the fibre cladding diameter as it is inversely proportional to the separation between FSBS resonance peaks.

In terms of the field deployment of the proposed distributed FSBS mesurement system, the main challenges are: First, the distributed FSBS response is obtained through the differentiation of the phase shift progression, even though the reading pulse of the system is configured to have 3 m spatial resolution, the uneven peak amplitude distribution of the backward Brillouin resonance contributes to the largest noise source that limits the differential length in the differentiation process to 15 m, setting the differential length smaller than this value results in a noisy trace that obscures the sensor's signal. Certain sophisticated polarisation issues such as polarisation pulling [79] could be the cause of this uneven Brillouin peak amplitude problem. Though Brillouin optical time domain analysis (BOTDA) has been developed for many years, this problem is rarely tackled because it is usually a non-issue for standard BOTDA with simple polarisation diversity scheme, for which the sensing method depends on reading the frequency shift of Brillouin resonance peak rather than measuring the broadening of resonance linewidth. Second, the complexity of the scanning procedures, which involves measuring the spectral distribution of multiple phase modulated sidebands, results in close to 30 minutes to complete a single distributed FSBS spectrum map. The scanning time has be to thoroughly optimized if a dynamic sensing application is required.

In the proposed distributed FSBS measurement system, the retrieved distributed FSBS spectrum is the convolution of the activation pulse spectrum and the acoustic resonance spectrum. Although the original linewidth can be retrieved accurately through fitting the experimentally obtained spectrum to the analytical expression of the convolution, the approach is non-ideal in field deployment as it would confuse the user of this system. The technique could probably be improved by a method that involves time delaying the reading pulse in consecutive small steps with respect to the FSBS activating pulse. This way, the reading pulse would interact with different parts of the acoustic tail in each delay step, thus the entire decay profile of the acoustic wave can be reconstructed. Then, the acoustic impedance can be obtained in a manner that is similar to the time domain technique.

In view of the limitations such as the uneven Brillouin resonance peak amplitude and the need of differentiating the acquired data (inherent challenges of this distributed FSBS measurement technique), the other existing distributed measurement techniques could be explored to position-resolve FSBS in a fibre. A potential technique that could be utilized in this case is the phase-sensitive optical time domain reflectometry (ϕ-OTDR) [43]. This technique is based on Rayleigh backscattering of a coherent light pulse along a fibre, which gives a signature backscattered light intensity pattern for that fibre. The cross-correlation of the backscattered light spectra under a perturbed scenario and that of a reference condition provides the information on the refractive index change along a fibre. Since FSBS induces refractive index change inside the fibre core, ϕ-OTDR could be one of the possible techniques to measured FSBS distribution along a fibre. Nevertheless, having a wide variety of existing distributed measurement techniques, the endeavour to realise another distributed FSBS measurement system is only limited by imagination.

A Mathematical operations in the cylindrical coordinate system

Vectorial calculus formulas

$$\nabla f = \left[\frac{\partial f}{\partial r}, \frac{1}{r}\frac{\partial f}{\partial \theta}, \frac{\partial f}{\partial z}\right] \tag{A.1a}$$

$$\nabla \cdot \mathbf{v} = \frac{1}{r}\frac{\partial (r v_r)}{\partial r} + \frac{1}{r}\frac{\partial v_\theta}{\partial \theta} + \frac{\partial v_z}{\partial z} \tag{A.1b}$$

$$\nabla^2 f = \frac{\partial^2 f}{\partial r^2} + \frac{1}{r}\frac{\partial f}{\partial r} + \frac{1}{r^2}\frac{\partial^2 f}{\partial \theta^2} + \frac{\partial^2 f}{\partial z^2} \tag{A.1c}$$

$$\nabla \wedge \mathbf{v} = \left[\frac{1}{r}\frac{\partial v_z}{\partial \theta} - \frac{\partial v_\theta}{\partial z}, \frac{\partial v_r}{\partial z} - \frac{\partial v_z}{\partial r}, \frac{1}{r}\left(\frac{\partial (r v_\theta)}{\partial r} - \frac{\partial v_r}{\partial \theta}\right)\right] \tag{A.1d}$$

Vector Laplacian

$$\nabla^2 \mathbf{v} = \begin{bmatrix} \nabla^2 v_r - \dfrac{2}{r^2}\dfrac{\partial v_\theta}{\partial \theta} - \dfrac{v_r}{r^2} \\ \nabla^2 v_\theta + \dfrac{2}{r^2}\dfrac{\partial v_r}{\partial \theta} - \dfrac{v_\theta}{r^2} \\ \nabla^2 v_z \end{bmatrix} \tag{A.2}$$

Transformed Bessel differential equation [2]

$$\frac{\mathrm{d}^2 y}{\mathrm{d}x^2} - \frac{2\alpha - 1}{x}\frac{\mathrm{d}y}{\mathrm{d}x} + \left(\beta^2\gamma^2 x^{2\gamma-2} + \frac{\alpha^2 - n^2\gamma^2}{x^2}\right) y = 0 \tag{A.3}$$

The solution is

$$y = x^\alpha \left[A J_n\left(\beta x^\gamma\right) + B Y_n\left(\beta x^\gamma\right)\right] \quad \text{for integer } n \tag{A.4}$$

B Material constants for standard silica optical fibre

Material constants for the core and cladding of standard silica optical fibre as compiled by J.-C. Beugnot and V. Laude in [11, 52].

		Fibre cladding (pure silica)	*Fibre core* (0.36 % GeO_2-doped silica)
Elastic constant (GPa)	c_{11}	78	76
	c_{12}	16	16.15
	c_{44}	31	29.9
Photoelastic constant	p_{11}	0.12	
	p_{12}	0.27	
	p_{44}	-0.073	
Material density (kg m^{-1})	ρ	2203	2254
Young's modulus (GPa)	E	72.55	70.34
Poisson's ratio	ν	0.170	0.175
Axial acoustic velocity (m s^{-1})	V_L	5950	5807
Shear acoustic velocity (m s^{-1})	V_T	3709	3642
Refractive index ($\lambda = 1550$ nm)	n	1.444	1.4492

C FSBS overlap integral

In Brillouin scattering, the relative interaction strength of different acoustic modes with the propagating optical wave is determined by the overlap factor Q_m^2. For a given waveguide, the transverse acoustic field distribution $u(r)$ differs for each guided acoustic mode, which gives rise to different Q_m^2. In fact, the process of Brillouin scattering can be subdivided into two consecutive parts. In the first part, the divergence of optical field $\nabla \cdot (E_1 E_2^*)$ produces material displacement u through electrostriction. In the second part, the induced material dilatation S results in dielectric constant change $\Delta\epsilon$ via photo-elastic effect. The overlap factor comprises the contributions from the electrostriction process Q_m^{es} and the photo-elastic process Q_m^{pe}, where $Q_m^2 = Q_m^{\mathrm{es}} Q_m^{\mathrm{pe}}$. In the final part, the overlap factor is simplified for the cases relevant to the Brillouin interactions discussed in this thesis.

The electrostriction process is governed by the elastodynamic equation (Eq. 1.93). For a cylindrical waveguide based on isotropic material, the electrostrictive force $\boldsymbol{f}^{\mathrm{es}}$ is derived by A. S. Biryukov *et al.* [14]. Consider random polarisation states inside the fibre, the azimuthal component (ϕ) is averaged out. The radial component (r) is derived by H. Hagai Diamandi *et al.* [27] and is rearranged as follows

$$\begin{aligned} f_r &= -\frac{1}{4nc}(a_1 + 4a_2) E_0(r) \frac{\partial E_0(r)}{\partial r} \\ &= -\frac{1}{8nc}(a_1 + 4a_2) \frac{\partial E_0^2(r)}{\partial r} \end{aligned} \tag{C.1}$$

where n is the refractive index of silica, c is the speed of light in vacuum, the parameters $a_{1,2}$ consist of the elements of the photo-elastic tensor of silica [14]: $a_1 = -n^4(p_{11} - p_{12})$ and $a_2 = -n^4 p_{12}$. Hence, the related electrostrictive transverse overlap integral for forward stimulated Brillouin scattering (FSBS) is defined as follows (similar to [27])

$$Q_{\mathrm{FB}}^{\mathrm{es(m)}} \equiv 2\pi \int_0^a \frac{\partial E_0^2(r)}{\partial r} u_0^{(m)}(r)\; r\mathrm{d}r \equiv \left\langle \frac{\partial E_0^2(r)}{\partial r} u_0^{(m)}(r) \right\rangle \tag{C.2}$$

A shorthand $\langle a, b\rangle$ is used here for the field overlap, which can be normalised as

$$\langle a, b\rangle_{\text{norm}} = \sqrt{\frac{\left|\int_0^a a\cdot b\; r\mathrm{d}r\right|^2}{\int_0^a |a|^2\; r\mathrm{d}r\; \int_0^a |b|^2\; r\mathrm{d}r}} \tag{C.3}$$

Due to photo-elastic effect, the dielectric constant change $\Delta\epsilon$ caused by the radial transverse acoustic modes is given by [14]

$$\begin{aligned}\Delta\epsilon &= \left(\frac{a_1}{2} + a_2\right)\left(\frac{\partial u_0^{(m)}(r)}{\partial r} + \frac{u_0^{(m)}(r)}{r}\right)\\ &= \left(\frac{a_1}{2} + a_2\right)\left(\frac{\partial\left(r u_0^{(m)}(r)\right)}{r\partial r}\right)\\ &= \left(\frac{a_1}{2} + a_2\right) S^{(m)}(r)\end{aligned} \tag{C.4}$$

where $S^{(m)}(r)$ is the dilatation. The FSBS photo-elastic overlap integral is defined as below (similar to [27])

$$Q_{\text{FB}}^{\text{pe}(m)} \equiv 2\pi \int_0^a S^{(m)}(r)\; E_0^2(r)\; r\mathrm{d}r \equiv \left\langle S^{(m)}(r), E_0^2(r)\right\rangle \tag{C.5}$$

Here, $Q_{\text{FB}}^{\text{es(m)}}$ is related to $Q_{\text{FB}}^{\text{pe}(m)}$ using integration by parts

$$\begin{aligned}Q_{\text{FB}}^{\text{es(m)}} &= \left[2\pi \int_0^a \frac{\partial E_0^2(r)}{\partial r} u_0^{(m)}(r)\; r\mathrm{d}r\right]\\ &= 2\pi\left[\left. r u_0^{(m)}(r) E_0^2(r)\right|_0^a - \int_0^a E_0^2(r)\; \frac{\partial(r u_0^{(m)}(r))}{r\partial r}\; r\mathrm{d}r\right]\\ &= 2\pi\left[\left. r u_0^{(m)}(r) E_0^2(r)\right|_0^a - \int_0^a E_0^2(r)\; S^{(m)}(r)\; r\mathrm{d}r\right]\\ &= 2\pi\; \left. r u_0^{(m)}(r) E_0^2(r)\right|_0^a - Q_{\text{FB}}^{\text{pe}(m)}\end{aligned} \tag{C.6}$$

The term $\left. r u_0^{(m)}(r) E_0^2(r)\right|_0^a$ is approximately zero as the optical field at the fibre boundary is close to zero, $E_0(a) \approx 0$, so that $Q_{\text{FB}}^{\text{es(m)}} \approx -Q_{\text{FB}}^{\text{pe}(m)}$. This is valid for standard single-mode fibre as the optical field close to the fibre boundary is negligible. Nevertheless, for small diameter microfibre, the optical field at the fibre boundary can be large and $Q_{\text{FB}}^{\text{es(m)}}$ is not equal to $-Q_{\text{FB}}^{\text{pe}(m)}$. Hence, for the analysis of FSBS in standard single-mode fibre, the overall FSBS normalised overlap factor can be simplified to

$$Q_{\text{FB}}^{2(m)} = \left|Q_{\text{FB}}^{\text{es(m)}} Q_{\text{FB}}^{\text{pe}(m)}\right| = \frac{\left|\int_0^a |E_0(r)|^2 \cdot S^{(m)}(r)\; r\mathrm{d}r\right|^2}{\int_0^a |E_0(r)|^4\; r\mathrm{d}r\; \int_0^a |S^{(m)}(r)|^2\; r\mathrm{d}r} \tag{C.7}$$

Bibliography

[1] NDT Resource Center-material properties tables. https://www.nde-ed.org/GeneralResources/MaterialProperties/UT/ut_matlprop_liquids.htm.

[2] Wolfram MathWorld-Cylindrical Coordinates. http://mathworld.wolfram.com/CylindricalCoordinates.html.

[3] Govind P Agrawal. Nonlinear fiber optics. In *Nonlinear Science at the Dawn of the 21st Century*, pages 195–211. Springer, 2000.

[4] Ghatak Ajoy and K Thyagarajan. *Introduction to Fibre Optics*. Cambridge University Press, 1999.

[5] Mehdi Alem, Marcelo A Soto, Moshe Tur, and Luc Thévenaz. Analytical expression and experimental validation of the Brillouin gain spectral broadening at any sensing spatial resolution. In *Optical Fiber Sensors Conference (OFS), 2017 25th*, pages 1–4. Ieee, 2017.

[6] Yair Antman, Alex Clain, Yosef London, and Avi Zadok. Optomechanical sensing of liquids outside standard fibers using forward stimulated Brillouin scattering. *Optica*, 3(5):510–516, 2016.

[7] Bertram Alexander Auld. *Acoustic fields and waves in solids Volume I*. John Wiley & Sons, Inc., 1973.

[8] Bertram Alexander Auld. *Acoustic fields and waves in solids Volume II*. John Wiley & Sons, Inc., 1973.

[9] Alexander A Balandin and Denis L Nika. Phononics in low-dimensional materials. *Mater. Today*, 15(6):266–275, 2012.

[10] Gil Bashan, Hilel Hagai Diamandi, Yosef London, Eyal Preter, and Avi Zadok. Optomechanical time-domain reflectometry. *Nature communications*, 9(1):2991, 2018.

[11] Jean-Charles Beugnot and Vincent Laude. Electrostriction and guidance of acoustic phonons in optical fibers. *Phys. Rev. B*, 86(22):224304, 2012.

[12] Jean-Charles Beugnot, Sylvie Lebrun, Gilles Pauliat, Hervé Maillotte, Vincent Laude, and Thibaut Sylvestre. Brillouin light scattering from surface acoustic waves in a subwavelength-diameter optical fibre. *Nat. Commun.*, 5, 2014.

[13] Timothy A Birks and Youwei W Li. The shape of fiber tapers. *J. Lightwave Technol.*, 10(4):432–438, 1992.

[14] AS Biryukov, Maksim Evgen'evich Sukharev, and Evgenii M Dianov. Excitation of sound waves upon propagation of laser pulses in optical fibres. *Quantum Electronics*, 32(9):765, 2002.

[15] Robert W Boyd. *Nonlinear optics.* Elsevier, 2003.

[16] Richard G Brewer and Klaus E Rieckhoff. Stimulated Brillouin scattering in liquids. *Physical Review Letters*, 13(11):334, 1964.

[17] Brillouin, Léon. Diffusion de la lumière et des rayons x par un corps transparent homogène - influence de l'agitation thermique. *Ann. Phys.*, 9(17):88–122, 1922.

[18] RY Chiao and BP Stoicheff. Brillouin scattering in liquids excited by the he–ne maser. *JOSA*, 54(10):1286–1287, 1964.

[19] RY Chiao, CH Townes, and BP Stoicheff. Stimulated Brillouin scattering and coherent generation of intense hypersonic waves. *Physical Review Letters*, 12(21):592, 1964.

[20] Desmond M Chow, Jean-Charles Beugnot, Adrien Godet, Kien P Huy, Marcelo A Soto, and Luc Thévenaz. Local activation of surface and hybrid acoustic waves in optical microwires. *Optics letters*, 43(7):1487–1490, 2018.

[21] Desmond M Chow and Luc Thévenaz. Forward Brillouin scattering acoustic impedance sensor using thin polyimide-coated fiber. *Optics letters*, 43(21):5467–5470, 2018.

[22] Desmond M Chow, Zhisheng Yang, Marcelo A Soto, and Luc Thévenaz. Distributed forward Brillouin sensor based on local light phase recovery. *Nature communications*, 9(1):2990, 2018.

[23] Raphael Cohen, Yosef London, Yair Antman, and Avi Zadok. Brillouin optical correlation domain analysis with 4 millimeter resolution based on amplified spontaneous emission. *Optics express*, 22(10):12070–12078, 2014.

[24] D Cotter. Suppression of stimulated Brillouin scattering during transmission of high-power narrowband laser light in monomode fibre. *Electronics Letters*, 18(15):638–640, 1982.

[25] Paulo Dainese, P St J Russell, Gustavo S Wiederhecker, Nicolas Joly, Hugo L Fragnito, Vincent Laude, and Abdelkrim Khelif. Raman-like light scattering from acoustic phonons in photonic crystal fiber. *Optics Express*, 14(9):4141–4150, 2006.

[26] Andrey Denisov, Marcelo A Soto, and Luc Thévenaz. Going beyond 1000000 resolved points in a Brillouin distributed fiber sensor: theoretical analysis and experimental demonstration. *Light-Sci. Appl.*, 5(5):e16074, 2016.

[27] H Hagai Diamandi, Yosef London, and Avi Zadok. Opto-mechanical inter-core cross-talk in multi-core fibers. *Optica*, 4(3):289–297, 2017.

[28] Hilel Hagai Diamandi, Yosef London, Gil Bashan, and Avi Zadok. Sensing outside polyimide-coated fibers using guided acoustic waves Brillouin scattering. In *CLEO: Science and Innovations*, pages SM3K–1. Optical Society of America, 2018.

[29] Eugene M Dianov, AV Luchnikov, AN Pilipetskii, and AN Starodumov. Electrostriction mechanism of soliton interaction in optical fibers. *Optics letters*, 15(6):314–316, 1990.

[30] RD Doolittle, H Überall, and P Uginčius. Sound scattering by elastic cylinders. *The Journal of the Acoustical Society of America*, 43(1):1–14, 1968.

[31] Immanuil L Fabelinskii. *Molecular scattering of light*. Springer Science & Business Media, 2012.

[32] Omar Florez, Paulo F Jarschel, Yovanny AV Espinel, CMB Cordeiro, TP Mayer Alegre, Gustavo S Wiederhecker, and Paulo Dainese. Brillouin scattering self-cancellation. *Nat. Commun.*, 7, 2016.

[33] Stella M Foaleng, Moshe Tur, Jean-Charles Beugnot, and Luc Thévenaz. High spatial and spectral resolution long-range sensing using Brillouin echoes. *Journal of Lightwave Technology*, 28(20):2993–3003, 2010.

[34] Dieter Garus, Katerina Krebber, Frank Schliep, and Torsten Gogolla. Distributed sensing technique based on Brillouin optical-fiber frequency-domain analysis. *Optics letters*, 21(17):1402–1404, 1996.

[35] Adrien Godet, Abdoulaye Ndao, Thibaut Sylvestre, Vincent Pecheur, Sylvie Lebrun, Gilles Pauliat, Jean-Charles Beugnot, and Kien Phan Huy. Brillouin spectroscopy of optical microfibers and nanofibers. *Optica*, 4(10):1232–1238, 2017.

[36] E Gross. Change of wave-length of light due to elastic heat waves at scattering in liquids. *Nature*, 126(3171):201, 1930.

[37] B Hadimioglu and BT Khuri-Yakub. Polymer films as acoustic matching layers. In *Ultrasonics Symposium, 1990. Proceedings., IEEE 1990*, pages 1337–1340. IEEE, 1990.

[38] EE Hagenlocker and WG Rado. Stimulated Brillouin and raman scattering in gases. *Applied Physics Letters*, 7(9):236–238, 1965.

[39] Jonas Hansryd, Peter A Andrekson, Mathias Westlund, Jie Li, and P-O Hedekvist. Fiber-based optical parametric amplifiers and their applications. *IEEE Journal of Selected Topics in Quantum Electronics*, 8(3):506–520, 2002.

[40] Wenbin He, Meng Pang, and Philip St J Russell. Wideband-tunable soliton fiber laser mode-locked at 1.88 ghz by optoacoustic interactions in solid-core pcf. *Optics express*, 23(19):24945–24954, 2015.

[41] Oliver S Heavens. *Optical properties of thin solid films.* Courier Corporation, 1991.

[42] Tsuneo Horiguchi, Kaoru Shimizu, Toshio Kurashima, Mitsuhiro Tateda, and Yahei Koyamada. Development of a distributed sensing technique using Brillouin scattering. *J. Lightwave Technol.*, 13(7):1296–1302, 1995.

[43] Y Horiuchi, S Ryu, K Mochizuki, and H Wakabayashi. Novel coherent heterodyne optical time domain reflectometry for fault localization of optical amplifier submarine cable systems. *IEEE Photonics Technology Letters*, 2(4):291–293, 1990.

[44] Kazuo Hotate and Takemi Hasegawa. Measurement of Brillouin gain spectrum distribution along an optical fiber using a correlation-based technique–proposal, experiment and simulation–. *IEICE T. Electron.*, 83(3):405–412, 2000.

[45] EP Ippen and RH Stolen. Stimulated Brillouin scattering in optical fibers. *Appl. Phys. Lett.*, 21(11):539–541, 1972.

[46] MS Kang, A Nazarkin, A Brenn, and P St J Russell. Tightly trapped acoustic phonons in photonic crystal fibres as highly nonlinear artificial Raman oscillators. *Nature Physics*, 5(4):276–280, 2009.

[47] Myeong Soo Kang, André Brenn, Gustavo S Wiederhecker, and Philip St J Russell. Optical excitation and characterization of gigahertz acoustic resonances in optical fiber tapers. *Applied Physics Letters*, 93(13):131110, 2008.

[48] Yong Hyun Kim and Kwang Yong Song. Mapping of intermodal beat length distribution in an elliptical-core two-mode fiber based on Brillouin dynamic grating. *Optics Express*, 22(14):17292–17302, 2014.

[49] KY Ko, MS Demokan, and HY Tam. Transient analysis of erbium-doped fiber amplifiers. *IEEE Photonics Technology Letters*, 6(12):1436–1438, 1994.

[50] Y Koyamada, S Sato, S Nakamura, H Sotobayashi, and W Chujo. Simulating and designing Brillouin gain spectrum in single-mode fibers. *Journal of Lightwave Technology*, 22(2):631–639, 2004.

[51] Vincent Laude. *Phononic crystals: artificial crystals for sonic, acoustic, and elastic waves*, volume 26. Walter de Gruyter GmbH & Co KG, 2015.

[52] Vincent Laude and Jean-Charles Beugnot. Generation of phonons from electrostriction in small-core optical waveguides. *AIP Adv.*, 3(4):042109, 2013.

[53] D Le Quang, Y Jaouën, M Zimmerli, P Gallion, and JB Thomine. Time-resolved measurement of dynamic frequency chirp due to electrostriction mechanism in optical fibers. *IEEE Photonics Technology Letters*, 8(3):414–416, 1996.

[54] CS Liu, Marshall N Rosenbluth, and Roscoe B White. Raman and Brillouin scattering of electromagnetic waves in inhomogeneous plasmas. *The Physics of Fluids*, 17(6):1211–1219, 1974.

[55] Aldo Minardo, Romeo Bernini, Ruben Ruiz-Lombera, Jesus Mirapeix, Jose Miguel Lopez-Higuera, and Luigi Zeni. Proposal of Brillouin optical frequency-domain reflectometry (bofdr). *Optics express*, 24(26):29994–30001, 2016.

[56] Yosuke Mizuno, Neisei Hayashi, Hideyuki Fukuda, Kwang Yong Song, and Kentaro Nakamura. Ultrahigh-speed distributed Brillouin reflectometry. *Light: Science & Applications*, 5(12):e16184, 2016.

[57] Yosuke Mizuno, Weiwen Zou, Zuyuan He, and Kazuo Hotate. Proposal of Brillouin optical correlation-domain reflectometry (bocdr). *Optics express*, 16(16):12148–12153, 2008.

[58] Rémy Mosseri. *Léon Brillouin, 1889-1969: à la croisée des ondes*. Belin, 1999.

[59] Masaharu Ohashi, Nori Shibata, and K Shirakai. Fibre diameter estimation based on guided acoustic wave Brillouin scattering. *Electronics Letters*, 28(10):900–902, 1992.

[60] Nils T Otterstrom, Ryan O Behunin, Eric A Kittlaus, Zheng Wang, and Peter T Rakich. A silicon Brillouin laser. *Science*, 360(6393):1113–1116, 2018.

[61] M Pang, X Jiang, W He, GKL Wong, G Onishchukov, NY Joly, G Ahmed, CR Menyuk, and P St J Russell. Stable subpicosecond soliton fiber laser passively mode-locked by gigahertz acoustic resonance in photonic crystal fiber core. *Optica*, 2(4):339–342, 2015.

[62] Yair Peled, Avi Motil, Lior Yaron, and Moshe Tur. Slope-assisted fast distributed sensing in optical fibers with arbitrary Brillouin profile. *Optics express*, 19(21):19845–19854, 2011.

[63] ER Pike, JM Vaughan, and WF Vinen. Brillouin scattering from first and second sound in a superfluid 3he 4he mixture. *Physics Letters A*, 30(7):373–374, 1969.

[64] Alistair J Poustie. Guided acoustic-wave Brillouin scattering with optical pulses. *Optics Letters*, 17(8):574–576, 1992.

[65] Wenjun Qiu, Peter T Rakich, Heedeuk Shin, Hui Dong, Marin Soljačić, and Zheng Wang. Stimulated Brillouin scattering in nanoscale silicon step-index waveguides: a general framework of selection rules and calculating sbs gain. *Optics express*, 21(25):31402–31419, 2013.

[66] Peter T Rakich, Paul Davids, and Zheng Wang. Tailoring optical forces in waveguides through radiation pressure and electrostrictive forces. *Optics express*, 18(14):14439–14453, 2010.

[67] WH Renninger, H Shin, RO Behunin, P Kharel, EA Kittlaus, and PT Rakich. Forward Brillouin scattering in hollow-core photonic bandgap fibers. *New Journal of Physics*, 18(2):025008, 2016.

[68] William H Renninger, Ryan O Behunin, and Peter T Rakich. Guided-wave Brillouin scattering in air. *Optica*, 3(12):1316–1319, 2016.

[69] Daniel Royer and Eugène Dieulesaint. *Elastic Waves in Solids I: Free and Guided Propagation, translated by DP Morgan.* Springer Science & Business Media, 1996.

[70] Daniel Royer and Eugene Dieulesaint. *Elastic waves in solids II: generation, acousto-optic interaction, applications.* Springer Science & Business Media, 1999.

[71] P St J Russell, D Culverhouse, and F Farahi. Theory of forward stimulated Brillouin scattering in dual-mode single-core fibers. *IEEE Journal of Quantum Electronics*, 27(3):836–842, 1991.

[72] RM Shelby, MD Levenson, and PW Bayer. Guided acoustic-wave Brillouin scattering. *Phys. Rev. B*, 31(8):5244, 1985.

[73] Heedeuk Shin, Wenjun Qiu, Robert Jarecki, Jonathan A Cox, Roy H Olsson III, Andrew Starbuck, Zheng Wang, and Peter T Rakich. Tailorable stimulated Brillouin scattering in nanoscale silicon waveguides. *Nature communications*, 4:1944, 2013.

[74] Kazuyuki Shiraki and Masaharu Ohashi. Sound velocity measurement based on guided acoustic-wave Brillouin scattering. *IEEE photonics technology letters*, 4(10):1177–1180, 1992.

[75] EK Sittig and GA Coquin. Visualization of plane-strain vibration modes of a long cylinder capable of producing sound radiation. *The Journal of the Acoustical Society of America*, 48(5B):1150–1159, 1970.

[76] Kwang-Yong Song, Zuyuan He, and Kazuo Hotate. Distributed strain measurement with millimeter-order spatial resolution based on Brillouin optical correlation domain analysis and beat lock-in detection scheme. In *Optical Fiber Sensors*, page ThC2. Optical Society of America, 2006.

[77] Kwang-Yong Song, Miguel González Herráez, and Luc Thévenaz. Mapping of chromatic-dispersion distribution along optical fibers with 20-m spatial resolution. *Journal of lightwave technology*, 23(12):4140, 2005.

[78] Kwang Yong Song and Hyuk Jin Yoon. High-resolution Brillouin optical time domain analysis based on Brillouin dynamic grating. *Optics letters*, 35(1):52–54, 2010.

[79] Marcelo A Soto, Moshe Tur, Alexia Lopez-Gil, Miguel Gonzalez-Herraez, and Luc Thévenaz. Polarisation pulling in Brillouin optical time-domain analysers. In *Optical Fiber Sensors Conference (OFS), 2017 25th*, pages 1–4. Ieee, 2017.

[80] Yosuke Tanaka and Kazuhiko Ogusu. Temperature coefficient of sideband frequencies produced by depolarized guided acoustic-wave Brillouin scattering. *IEEE Photonics Technology Letters*, 10(12):1769–1771, 1998.

[81] Yosuke Tanaka and Kazuhiko Ogusu. Tensile-strain coefficient of resonance frequency of depolarized guided acoustic-wave Brillouin scattering. *IEEE Photonics Technology Letters*, 11(7):865–867, 1999.

[82] Joël Cabrel Tchahame, Jean-Charles Beugnot, Kien Phan Huy, Vincent Laude, Alexandre Kudlinski, and Thibaut Sylvestre. Surface Brillouin scattering in photonic crystal fibers. *Opt. Lett.*, 41(14):3269–3272, 2016.

[83] R Vacher and L Boyer. Brillouin scattering: A tool for the measurement of elastic and photoelastic constants. *Physical Review B*, 6(2):639, 1972.

[84] Raphaël Van Laer, Bart Kuyken, Dries Van Thourhout, and Roel Baets. Interaction between light and highly confined hypersound in a silicon photonic nanowire. *Nature Photonics*, 9(3):199, 2015.

[85] Armand Vedadi, Dario Alasia, Eric Lantz, Hervé Maillotte, Luc Thévenaz, Miguel Gonzalez-Herraez, and Thibaut Sylvestre. Brillouin optical time-domain analysis of fiber-optic parametric amplifiers. *IEEE Photonics Technology Letters*, 19(3):179–181, 2007.

[86] Jing Wang, Yunhui Zhu, Rui Zhang, and Daniel J Gauthier. FSBS resonances observed in a standard highly nonlinear fiber. *Optics Express*, 19(6):5339–5349, 2011.

[87] Richard M White. Surface elastic waves. *Proceedings of the IEEE*, 58(8):1238–1276, 1970.

[88] Christian Wolff, Birgit Stiller, BJ Eggleton, Michael J Steel, and Christopher G Poulton. Cascaded forward Brillouin scattering to all stokes orders. *New Journal of Physics*, 19(2):023021, 2017.

[89] Teck L Yeo, Tong Sun, Kenneth TV Grattan, David Parry, Rob Lade, and Brian D Powell. Polymer-coated fiber Bragg grating for relative humidity sensing. *IEEE Sens. J.*, 5(5):1082–1089, 2005.

[90] Avi Zadok, Yair Antman, Nikolay Primerov, Andrey Denisov, Juan Sancho, and Luc Thevenaz. Random-access distributed fiber sensing. *Laser. Photonics Rev.*, 6(5), 2012.

[91] Atiyeh Zarifi, Birgit Stiller, Moritz Merklein, Neuton Li, Khu Vu, Duk-Yong Choi, Pan Ma, Stephen J Madden, and Benjamin J Eggleton. Highly localized distributed Brillouin scattering response in a photonic integrated circuit. *APL Photonics*, 3(3):036101, 2018.

[92] Mark S Zediker, Charles C Rinzler, Brian O Faircloth, Yeshaya Koblick, and Joel F Moxley. Method and apparatus for delivering high power laser energy over long distances, April 2015. US Patent 8,997,894.

Desmond CHOW Ming Chia
Email: desmond.chow@epfl.ch
Tel: +41 (0) 78 82 77 328

Specialisation:

- Optical sensing and precision measurement
- Light detection and ranging (LIDAR)
- Distributed fibre based sensing network
- Design and fabrication of specialty optical fibres
- Real time multivariate data and signal processing
- Brillouin based optical phase engineering
- Multiphysics modelling of optoacoustic systems
- Managing international collaborative research

Education:

2014-2018 **PhD in Photonics at *Ecole Polytechnique Fédérale de Lausanne* (EPFL)**
-Thesis title: Distributed analyses using distinct classes of Brillouin scatterings in optical fibres

2012-2014 **Master in Engineering Science (Photonics) at *University of Malaya***
-Dissertation title: Design and fabrication of photonic crystal fibres

2007-2011 **Bachelor of Engineering (Electrical) at *University of Malaya***
-Major in microelectronics
-Minor in power systems

Professional Experience:

2014-2018 **Ecole Polytechnique Féderale de Lausanne (EPFL)** (Doctoral Assistant)

1. Implemented a fibre optics sensing network based on laser generated transverse acoustic waves for location specific (resolution: 15 m) chemical detection. This invention expanded the market for distributed fibre sensing technology which hitherto measures only temperature and strain.

2. Constructed a cross-correlation based fibre optics system using phase-coded lights to generate local surface acoustic waves in a microfibre. This technique allows the investigation of different optoacoustic mechanisms present in a non-uniform fibre/waveguide at sub-cm spatial resolution.

3. Demonstrated the first organic based chemical vapour sensor using spider silk with the construction of a precision mechanism for light in-coupling and polarization analysis. This invention opens the door for bio-compatible chemical sensor with high sensitivity.

2012-2014 **University of Malaya** (Research Assistant)

Designed a solid-core photonic crystal fibre that allows optical transmission at C+L band and optimized the stack-and-draw fabrication technique for its fabrication. This allows the production of low-cost, km-scale photonic crystal fibre filter.

2011-2012 **IC Microsystems Ltd.** (Intern)

Simulated IC component using Silvaco TCAD tool (Athena); Generated full-custom IC layout design and verification using Silvaco Gateway and Expert. Reduced defective units in a multi-project silicon wafer from 2.5 % to less than 0.75 %

Hands-on experience: Programming languages: MATLAB, Octave, Python, C++; Modelling and design tools: COMSOL, AutoCAD, Altium, Cinema 4D; Data acquisition tools: LabVIEW, PIC microcontrollers; Publishing tools: LaTeX, Adobe Illustrator; Web programming: PHP, HTML, SQL; Characterisation tools: polarisation analyser, vector network analyser, arbitrary waveform generators, locked-in amplifier.

Language: English (IELTS 8.0/9.0), Mandarin (Mother tongue), French (B1 Level), Malay (Competent)

Publications:

Journal papers

1. Chow, D. M., Z. Yang, Soto, M. A., & Thévenaz, L. (2018) Distributed forward Brillouin sensor based on local light phase recovery. *Nature Communications, 9(1), 2990.*
2. Chow, D. M., & Thévenaz, L. (2018). Forward Brillouin scattering acoustic impedance sensor using thin polyimide-coated fiber. *Optics Letters*, 43(21), 5467-5470.
3. Chow, D. M., Beugnot, J. C., Godet, A., Huy, K. P., Soto, M. A., & Thévenaz, L. (2018). Local activation of surface and hybrid acoustic waves in optical microwires. *Optics Letters*, *43*(7), 1487-1490.
4. Yang, Z., Soto, M. A., Chow, D. M., Ray, P., & Thévenaz, L. (2018). Brillouin Distributed Optical Fiber Sensor Based on a Closed-Loop Configuration. *Journal of Lightwave Technology*, 36(5), 1239-1248.
5. Tow, K. H., Chow, D. M., Vollrath, F., Dicaire, I., Gheysens, T., & Thévenaz, L. (2018). Exploring the Use of Native Spider Silk as an Optical Fiber for Chemical Sensing. *Journal of Lightwave Technology*, 36(4), 1138-1144.
6. Rifat, A. A., Mahdiraji, G. A., Ahmed, R., Chow, D. M., Sua, Y. M., Shee, Y. G., & Adikan, F. M. (2016). Copper-Graphene-Based Photonic Crystal Fiber Plasmonic Biosensor. *IEEE Photonics Journal*, 8(1), 1-8.
7. Rifat, A. A., Mahdiraji, G. A., Chow, D. M., Shee, Y. G., Ahmed, R., & Adikan, F. R. M. (2015). Photonic crystal fiber-based surface plasmon resonance sensor with selective analyte channels and graphene-silver deposited core. *Sensors*, 15(5), 11499-11510.
8. Rifat, A. A., Mahdiraji, G. A., Sua, Y. M., Shee, Y. G., Ahmed, R., Chow, D. M., & Adikan, F. M. (2015). Surface plasmon resonance photonic crystal fiber biosensor: a practical sensing approach. *IEEE Photonics Technology Letters*, 27(15), 1628-1631.
9. Kakaie, Z., Shakibaei, B. H., Sua, Y. M., Chow, D. M., Mahdiraji, G. A., & Adikan, F. R. M. (2015). Design of Single-Band Bandpass Filter Using Photonic Bandgap Fiber by Suppressing Core Modes in Higher Order Bandgaps. *IEEE Photonics Journal*, 7(3), 1-14.
10. Amouzad Mahdiraji, G., Chow, D. M., Sandoghchi, S. R., Amirkhan, F., Dermosesian, E., Yeo, K. S., & Mahamd Adikan, F. R. (2014). Challenges and solutions in fabrication of silica-based photonic crystal fibers: An experimental study. *Fiber and Integrated Optics*, 33(1-2), 85-104.
11. Mahdiraji, G. A., Amirkhan, F., Chow, D. M., Kakaie, Z., Yong, P. S., Dambul, K. D., & Adikan, F. R. M. (2014). Multicore flat fiber: a new fabrication technique. *IEEE Photonics Technology Letters*, 26(19), 1972-1974.

Conferences

1. Chow, D. M., Yang, Z., Soto, M. A., & Thévenaz, L. (2018, September). Distributed acoustic impedance measurement based on forward stimulated Brillouin scattering. In *International Conference on Optical Fibre Sensors OFS-26*, Lausanne, Switzerland. (Received the Best Student Paper Award).
2. Chow, D. M., Soto, M. A., & Thévenaz, L. (2017, April). Frequency-domain technique to measure the inertial response of forward stimulated Brillouin scattering for acoustic impedance sensing. In *International Conference on Optical Fibre Sensors OFS-25*, Jeju, South Korea.
3. Chow, D. M., Tow, K. H., Vollrath, F., Dicaire, I., Gheysens, T., & Thévenaz, L. (2015, October). Shedding light on the optical properties of spider silk fiber. In 2015 IEEE Photonics Conference (IPC) (pp. 333-334). IEEE.
4. Chow, D. M., NOUGNIHI, J. C. T., Denisov, A., Beugnot, J. C., Sylvestre, T., Li, L., & Thévenaz, L. (2015, October). Mapping the Uniformity of Optical Microwires Using Phase-Correlation Brillouin Distributed Measurements. InFrontiers in Optics (pp. FW4F-4). Optical Society of America.
5. Chow, D. M., Sandoghchi, S. R., & Adikan, F. M. (2012, October). Fabrication of photonic crystal fibers. In 2012 IEEE 3rd International Conference on Photonics.
6. Chow, D. M., Tee, D. C., Sandoghchi, S. R., & Adikan, F. M. (2012, June). Direct UV Written Waveguide's Dispersion in Flexible Silica Flat Fibre Chip. In Nonlinear Photonics (pp. SM2E-4). Optical Society of America.